Doctoral Dissertation

Enhancing Selectivity, Sensitivity, and Molecular Identification towards High-performance Graphene Gas Sensors

Osazuwa Gabriel Agbonlahor

Supervisor: Professor Hiroshi Mizuta

Graduate School of Advanced Science and Technology
Japan Advanced Institute of Science and Technology
[Materials Science]
March 2021

Abstract

Detecting minute concentrations of gaseous pollutants in the atmosphere and human breath enables environmental monitoring and non-invasive detection of ailments. Consequently, due to graphene's single-molecule sensitivity, it is highly sought after for high sensitivity gas detection. However, its poor selectivity, huge p-doping in the atmosphere, and inability to identify adsorbed gases makes graphene less useful for practical applications in environmental and clinical gas sensors which are typically deployed in atmospheric conditions. Hence in this work, we develop a chemical vapour deposition (CVD) graphene-based sensor with extreme ammonia sensitivity and selectivity in atmospheric air. Furthermore, we demonstrate the van der Waals (vdW) bonding memory of adsorbed gases on graphene and consequently demonstrate a proof-of-concept, the Charge Neutrality Point Disparity (CNPD), that characterizes various gases in atmospheric air.

First, we demonstrate the gas sensing, electrical properties, and morphological characteristics of a 38 nm oxidized activated carbon functionalized graphene field-effect transistor (a-CF-GFET) sensor. We show that the activated carbon (a-C) on the graphene channel passivates the graphene channel against p-doping in the atmosphere while simultaneously enhancing ammonia selectivity. Consequently, 500 parts per trillion (ppt) of ammonia was detected in the atmosphere with a response time of 3 seconds making the a-CF-GFET sensor the most sensitive ammonia selective sensor so far reported. The extreme ammonia sensitivity makes the a-CF-GFET sensor suitable for environmental monitoring and non-invasive medical diagnosis of ailments such as ulcers and kidney problems using ammonia as a biomarker.

Furthermore, we demonstrate that the electric field induced graphene-molecule charge transfer is retained in the graphene-molecule vdW complex even after the electric field is turned off, with the retained charge still unique to the applied electric field magnitude and direction.

Consequently, the vdW bonding memory of adsorbed molecules on graphene was observed. This bonding memory is important for the molecular identification of gases based on their electrically tunable charge transfer.

Following the observation of the vdW bonding memory, we demonstrate a proof of concept for a charge transfer based molecular identification technique, the CNPD method which measures the charge-transfer induced by consecutive applications of ∓tuning voltages ($\mp V_t$). The difference between the $-V_t$ and $+V_t$ induced charge transfer obtained from the shift of graphene's charge neutrality point was characteristic of various gas environments detecting parts per billion concentrations of ammonia and acetone.

In conclusion, we demonstrate a facile fabrication route for the simultaneous activation of the graphene channel towards ammonia selectivity while passivating it against atmospheric p-doping. Thereafter we show that adsorbed gases on graphene possess a tuning voltage induced van der Waals bonding memory lasting over 2h. Finally, following the demonstration of this vdW bonding memory, a proof-of-concept for a charge-based molecular identification technique, CNPD, which characterizes adsorbed gases based on their electrically tunable charge transfer is demonstrated.

Keywords: CVD graphene, ammonia selectivity, activated carbon, scattering, molecular identification

Contents

Acronyms

ppb	Parts Per Billion
UV	Ultraviolet
CNPD	Charge Neutrality Point Disparity
eV	Electron Volt
PMMA	Polymethylmethacrylate
MMA	Methylmethacrylate
CVD	Chemical Vapour Deposition
MFC	Mass Flow Controllers
a-C	Activated Carbon
a-CF-GFET	Activated Carbon Functionalized Graphene Field-effect Transistor
ppt	Parts Per Trillion
AFM	Atomic Force Microscopy
V_t	Tuning Voltage
vdW	van der Waals
nd	Doping Concentration
GFET	Graphene Field-effect Transistors
CNP	Charge Neutrality Point
IV_t	In-Between the V_t Experiments
AV_t	After the V_t Experiments
DFT	Density Functional Theory
revPBE	Perdew-Burke-Ernzerhof

Symbols

e-	Electronic Charge
σ	Conductivity
σ_i	Initial Conductivity
σ_f	Final Conductivity
μ	Mobility
$\Delta\mu$	Change in Mobility
n	Carrier Concentration
I_d	Drain Current
V_g	Gate Voltage
V_{ds}	Source-Drain Voltage
L	Device Length
W	Device Width
ΔV_{CNP}	CNP Shift
Cg	Gate Capacitance
$\boldsymbol{\varepsilon}_o$	Permittivity of Vacuum
$\boldsymbol{\varepsilon}_r$	Relative Permittivity of SiO_2
t_{ox}	SiO_2 Thickness
$\mu_{(max)vac}$	Maximum Field-Effect Mobility in Vacuum
$\mu_{(max)gas}$	Maximum Field-Effect Mobility in the Gas Environment
$E_{gra\text{-}mol}$	Total Energy of the Graphene-Molecule System
E_{gra}	Total Energies of Graphene
E_{mol}	Total Energies of the Isolated CO_2 Molecule
R_{tot}	Source-Drain Resistance
R_c	Contact Resistance
$R_{channel}$	Device Channel Resistance
N_{sq}	Number of Squares of the Gated Area (L/W)
n_o	Intrinsic Carrier Concentration at the CNP
$n[V_{TG}^*]$	Gate-Induced Carrier Concentration from the CNP
$\hbar$	Reduced Planck's Constant
v_F	Fermi Velocity

List of Figures

Chapter 1

Introduction

1.1. Pollutants and the significance of graphene-based gas sensors

With a mass of 1 millionth that of the earth,[1] the atmosphere facilitates respiratory processes in animals and photosynthesis of carbohydrates in plants, supporting life on the planet while being crucial for reducing global warming, and ozone layer depletion. Consequently, the air quality of the atmosphere is crucial to the survival of life on the planet, not to mention the prevention of economic loss of artifacts and capital assets. To put the effects of atmospheric pollutants in perspective, oxides of nitrogen and sulphur even at concentrations as low as 200 parts per billion result in severe respiratory problems.[2,3] Sources of pollutants in the atmosphere include both natural events such as volcanoes, natural fires as well as anthropogenic activities from the use of cars, industrial processes, airplanes, combustion, gas flaring activities, etc. [2,3]

Additionally, since the amount of biomarkers (such as ammonia, acetone, sulphur compounds, isoprene, etc.) [4] produced by the human body depend on the health condition of the individual, their detection in breath can be used for non-invasive medical diagnosis of different ailments. For instance, ammonia in human breath can be used as a biomarker for the diagnosis of urea cycle disorder,[5] kidney problems,[6,7] or ulcers resulting from *Helicobacter pylori* bacterial infection in the stomach.[6] However, the small volume of respired air obtainable in breath analysis, demands very high sensitivity (< 50 parts per billion (ppb)) clinical ammonia sensors with a maximum response time of a few minutes.[6,8] For effective environmental monitoring of ammonia, the

sensitivity of < 2 ppb is desired.[9]

Since the first successful fabrication of graphene devices,[10] and detection of single-molecule adsorption events,[11,12] its ubiquitous application as the ultimate sensing platform was widely expected due to its extreme sensitivity, low electronic noise levels,[13] high surface to volume ratio, and outstanding electronic properties such as carrier mobility and ambi-polar characteristics (i.e. ability to conduct with both holes and electrons).[12,14,15] So far, the most sensitive graphene-based ammonia sensors have detection limits of 41 ppb ((in nitrogen environment),[16] 200ppb (in vacuum at a temperature of 425K),[17] 84ppb in argon environment (increasing to 200ppt with *in situ* UV cleaning).[18] Notably, the aforementioned reports were performed in inert environments, while actual selective ammonia sensing is required in atmospheric air.

Gas sensing experiments using graphene are not done in atmospheric air because of the huge p-doping of graphene upon exposure to atmospheric air resulting from the acceptor properties of the oxygen/H_2O electrochemical couple[19,20] as shown in equation 1.

$$O_2 + 2H_2O + 4e^- \rightarrow 4OH^- \quad (1)$$

The electrons (e^-) needed for the electrochemical reaction are provided by graphene, resulting in depletion of the occupied electron states in graphene, and consequently p-doping. Hence, demonstrations of high sensitivity and selectivity of graphene sensors are typically performed using pure gases in vacuum,[12] nitrogen,[21] argon,[21] or dry air[13] which largely limit its commercial application as a sensing material.

Additionally, gas selectively i.e. detecting a particular gas while being relatively insensitive to other gases is highly desirable for the commercialization of graphene sensors. This is typically achieved by nanoparticle functionalization,[22] polymer functionalization,[22] and/or oxidation of graphene (i.e. graphene oxides and reduced graphene oxides).[23] While these methods often

improve the selectivity of graphene especially in inert environments, they also reduce the electronic properties of the device, for instance, oxidation of graphene to graphene oxide could result in mobility as low as $5cm^2/V.S$,[24] at least three orders of magnitude below the mobility of pristine graphene.

Additionally, inducing molecular identification in graphene sensors is becoming of increasing interest for high performance in graphene sensors.[14,25–27] Molecular identification is very important for gas sensing in complex environments (consisting of a mixture of gases), especially if the sensor has limited selectivity. Notable approaches towards molecular identification include demonstrations of generation-recombination 1/f noise peak frequencies characteristic of specific gases,[13] and the deployment of machine learning (ML) pattern recognition algorithms using either an array of functionalized selective gas sensors or a single graphene sensor as an electronic nose (e-nose).[25] Although, the use of arrays of functionalized sensors has provided impressive results, the huge number of analyte gases of interest in applications such as environmental monitoring makes this method limited in its application. Consequently, there has been increasing interest in the use of machine learning pattern recognition algorithms with a single graphene sensor for molecular identification.[25] Nevertheless, for the successful deployment of ML pattern recognition algorithms using a single graphene sensor, gas specific electronic responses are desired as these have been shown to improve the performance of ML algorithms.[25]

1.2. Motivation and aims

From the above discussions, to achieve high performance in graphene gas sensors three core challenges need to be addressed namely:

(i) The development of graphene devices with minimal p-doping in the air while

maintaining high sensitivity and selectivity towards target analyte.

(ii) The sensors should be amenable with the current lithographic process, with a facile and scalable fabrication.

(iii) The measurement technique should be facile and yield electronic responses unique to individual gases. Consequently, suitable for molecular identification (i.e. e-nose) applications.

In this work, we address the above challenges while providing new insights into graphene device fabrication techniques, sensing methods, and understanding of graphene-adsorbed molecules van der Waals bonding interactions towards high performance in graphene-based gas sensors.

1.3. Structure of this thesis

An introduction to gas sensing, as well as the motivation, aims, challenges, and prospects of graphene gas sensors, are presented in Chapter 1. In Chapter 2, a theoretical and experimental background on gas sensing mechanism of graphene gas sensors as well as some previous experimental findings and theories are presented. In chapter 3 a highly selective ammonia gas sensor, with a room temperature sensitivity of 500 parts per trillion and a response time of 3 seconds is presented. The sensor consists of a graphene channel covered with porous oxidized activated carbon which simultaneously facilitates minimal p-doping when exposed to atmospheric air while inducing ammonia selectivity. In chapter 4, the dependence of gas adsorption induced doping and scattering on the gas adsorption distance is presented. Consequently, the concept of graphene-molecule van der Waals bonding memory (i.e. the retention of electrically induced charge-transfer long after the electric field is turned off) is demonstrated. The vdW bonding memory is important for the realization of tunable charge-transfer-based molecular identification

techniques. A proof-of-concept for a charge-transfer-based molecular identification technique called the charge neutrality point disparity (CNPD) is presented in chapter 5. The CNPD method is shown to depend on both the applied electric field magnitude and time. The CNPD method successfully characterized different adsorbed gases even at parts per billion concentrations in atmospheric air. In chapter 6, the conclusion and prospects for this research is presented.

References

(1) How Much Does Earth's Atmosphere Weigh? | Britannica Blog http://blogs.britannica.com/2012/01/how-much-does-earth-atmosphere-weigh/ (accessed Oct 7, 2020).

(2) Florentina, I.; Io, B. The Effects of Air Pollutants on Vegetation and the Role of Vegetation in Reducing Atmospheric Pollution. In *The Impact of Air Pollution on Health, Economy, Environment and Agricultural Sources*; InTech, 2011. https://doi.org/10.5772/17660.

(3) Manisalidis, I.; Stavropoulou, E.; Stavropoulos, A.; Bezirtzoglou, E. Environmental and Health Impacts of Air Pollution: A Review. *Frontiers in Public Health*. Frontiers Media S.A. February 20, 2020, p 14. https://doi.org/10.3389/fpubh.2020.00014.

(4) Buszewski, B.; Kęsy, M.; Ligor, T.; Amann, A. Human Exhaled Air Analytics: Biomarkers of Diseases. *Biomed. Chromatogr.* **2007**, *21* (6), 553–566. https://doi.org/10.1002/bmc.835.

(5) Ayyub, O. B.; Behrens, A. M.; Heligman, B. T.; Natoli, M. E.; Ayoub, J. J.; Cunningham, G.; Summar, M.; Kofinas, P. Simple and Inexpensive Quantification of Ammonia in Whole Blood. *Mol. Genet. Metab.* **2015**, *115* (2–3), 95–100. https://doi.org/10.1016/j.ymgme.2015.04.004.

(6) Timmer, B.; Olthuis, W.; Berg, A. van den. Ammonia Sensors and Their Applications—a Review. *Sensors Actuators B Chem.* **2005**, *107* (2), 666–677.

https://doi.org/10.1016/J.SNB.2004.11.054.

(7) Narasimhan, L. R.; Goodman, W.; Patel, C. K. Correlation of Breath Ammonia with Blood Urea Nitrogen and Creatinine during Hemodialysis. *Proc. Natl. Acad. Sci. U. S. A.* **2001**, *98* (8), 4617–4621. https://doi.org/10.1073/pnas.071057598.

(8) Verpoorte, E. Microfluidic Chips for Clinical and Forensic Analysis. *Electrophoresis* **2002**, *23* (5), 677–712. https://doi.org/10.1002/1522-2683(200203)23:5<677::AID-ELPS677>3.0.CO;2-8.

(9) Tadi, K. K.; Pal, S.; Narayanan, T. N. Fluorographene Based Ultrasensitive Ammonia Sensor. *Sci. Rep.* **2016**, *6* (1), 25221. https://doi.org/10.1038/srep25221.

(10) Novoselov, K. S.; Jiang, D.; Schedin, F.; Booth, T. J.; Khotkevich, V. V.; Morozov, S. V.; Geim, A. K. Two-Dimensional Atomic Crystals. *Proc. Natl. Acad. Sci. U. S. A.* **2005**, *102* (30), 10451–10453. https://doi.org/10.1073/pnas.0502848102.

(11) Schedin, F.; Geim, A. K.; Morozov, S. V.; Hill, E. W.; Blake, P.; Katsnelson, M. I.; Novoselov, K. S. Detection of Individual Gas Molecules Adsorbed on Graphene. *Nat. Mater.* **2007**, *6* (9), 652–655. https://doi.org/10.1038/nmat1967.

(12) Sun, J.; Muruganathan, M.; Mizuta, H. Room Temperature Detection of Individual Molecular Physisorption Using Suspended Bilayer Graphene. *Sci. Adv.* **2016**, *2* (4), e1501518–e1501518. https://doi.org/10.1126/sciadv.1501518.

(13) Rumyantsev, S.; Liu, G.; Shur, M. S.; Potyrailo, R. A.; Balandin, A. A. Selective Gas Sensing with a Single Pristine Graphene Transistor. *Nano Lett.* **2012**, *12* (5), 2294–2298. https://doi.org/10.1021/nl3001293.

(14) Muruganathan, M.; Sun, J.; Imamura, T.; Mizuta, H. Electrically Tunable van Der Waals Interaction in Graphene–Molecule Complex. *Nano Lett.* **2015**, *15* (12), 8176–8180.

https://doi.org/10.1021/acs.nanolett.5b03653.

(15) Kulothungan, J.; Muruganathan, M.; Mizuta, H. Modulation of Twisted Bilayer CVD Graphene Interlayer Resistivity by Order of Magnitude Based on In-Situ Annealing. *Carbon N. Y.* **2019**, *153*, 355–363. https://doi.org/10.1016/j.carbon.2019.07.036.

(16) Fujitsu. Fujitsu Develops World's First Gas Sensor to Apply a New Principle for Graphene Use - Fujitsu Global http://www.fujitsu.com/global/about/resources/news/press-releases/2016/1205-01.html (accessed Sep 28, 2018).

(17) Noll, D.; Schwalke, U. Ammonia Sensors Based on in Situ Fabricated Nanocrystalline Graphene Field-Effect Devices. In *2018 13th International Conference on Design & Technology of Integrated Systems In Nanoscale Era (DTIS)*; IEEE, 2018; pp 1–5. https://doi.org/10.1109/DTIS.2018.8368566.

(18) Chen, G.; Paronyan, T. M.; Harutyunyan, A. R. Sub-Ppt Gas Detection with Pristine Graphene. *Appl. Phys. Lett.* **2012**, *101* (5), 053119. https://doi.org/10.1063/1.4742327.

(19) Yang, Y.; Brenner, K.; Murali, R. The Influence of Atmosphere on Electrical Transport in Graphene. *Carbon N. Y.* **2012**, *50* (5), 1727–1733. https://doi.org/10.1016/J.CARBON.2011.12.008.

(20) Sato, Y.; Takai, K.; Enoki, T. Electrically Controlled Adsorption of Oxygen in Bilayer Graphene Devices. *Nano Lett.* **2011**, *11* (8), 3468–3475. https://doi.org/10.1021/nl202002p.

(21) Smith, A. D.; Elgammal, K.; Fan, X.; Lemme, M. C.; Delin, A.; Råsander, M.; Bergqvist, L.; Schröder, S.; Fischer, A. C.; Niklaus, F.; et al. Graphene-Based CO_2 Sensing and Its Cross-Sensitivity with Humidity. *RSC Adv.* **2017**, *7* (36), 22329–22339. https://doi.org/10.1039/C7RA02821K.

(22) Georgakilas, V.; Otyepka, M.; Bourlinos, A. B.; Chandra, V.; Kim, N.; Kemp, K. C.; Hobza,

P.; Zboril, R.; Kim, K. S. Functionalization of Graphene: Covalent and Non-Covalent Approaches, Derivatives and Applications. *Chemical Reviews*. American Chemical Society November 14, 2012, pp 6156–6214. https://doi.org/10.1021/cr3000412.

(23) Some, S.; Xu, Y.; Kim, Y.; Yoon, Y.; Qin, H.; Kulkarni, A.; Kim, T.; Lee, H. Highly Sensitive and Selective Gas Sensor Using Hydrophilic and Hydrophobic Graphenes. *Sci. Rep.* **2013**, *3* (1), 1–8. https://doi.org/10.1038/srep01868.

(24) Wang, Y.; Chen, Y.; Lacey, S. D.; Xu, L.; Xie, H.; Li, T.; Danner, V. A.; Hu, L. Reduced Graphene Oxide Film with Record-High Conductivity and Mobility. *Mater. Today* **2018**, *21* (2), 186–192. https://doi.org/10.1016/j.mattod.2017.10.008.

(25) Hayasaka, T.; Lin, A.; Copa, V. C.; Lopez, L. P.; Loberternos, R. A.; Ballesteros, L. I. M.; Kubota, Y.; Liu, Y.; Salvador, A. A.; Lin, L. An Electronic Nose Using a Single Graphene FET and Machine Learning for Water, Methanol, and Ethanol. *Microsystems Nanoeng.* **2020**, *6* (1), 1–13. https://doi.org/10.1038/s41378-020-0161-3.

(26) Agbonlahor, O. G.; Muruganathan, M.; Imamura, T.; Mizuta, H. Adsorbed Molecules as Interchangeable Dopants and Scatterers with a Van Der Waals Bonding Memory in Graphene Sensors. *ACS Sensors* **2020**, *5* (7), 2003–2009. https://doi.org/10.1021/acssensors.0c00403.

(27) Liu, Y.; Liu, H.; Chu, Y.; Cui, Y.; Hayasaka, T.; Dasaka, V.; Nguyen, L.; Lin, L. Defect-Induced Gas Adsorption on Graphene Transistors. *Adv. Mater. Interfaces* **2018**, *5* (9), 1701640. https://doi.org/10.1002/admi.201701640.

Chapter 2

Research background

2.1. Theoretical background

2.1.1 Graphene lattice structure

Graphene is an atomic layer thick planar honeycomb lattice of sp^2 hybridized carbon atoms with a carbon-carbon bond length of 1.42 Å. The unit cell of graphene is a 6-membered ring of carbon atoms. The Bravais lattice consists of two vectors $\overline{a1}$ and $\overline{a2}$ and two non-equivalent atoms as shown in Figure 1.[1] Taking the coordinate system (0, x, y), $\overline{a1} = \left(\frac{\sqrt{3}a_o}{2}, \frac{a_o}{2}\right)$ and $\overline{a2} = \left(\frac{\sqrt{3}a_o}{2}, -\frac{a_o}{2}\right)$ with an angle of $\pi/3$ between them, such that $|\overline{a1}| = |\overline{a2}| = a_0$. Consequently, the reciprocal lattice (Figure 1b) is spanned by vectors $\overline{b1} = \left(\frac{2\pi}{\sqrt{3}a_o}, \frac{2\pi}{a_0}\right)$ and $\overline{b2} = \left(\frac{2\pi}{\sqrt{3}a_o}, -\frac{2\pi}{a_0}\right)$, with $|\overline{b1}| = |\overline{b2}| = 4\pi\sqrt{3}a_0$ and an angle of $2\pi/3$ between them.

Each carbon atom forms three σ bonds using its 2s, 2px, and 2py orbitals. The 2pz orbital which is perpendicular to the plane of hybridization forms a delocalized π electron cloud. These π electrons are free to move in the plane of hybridization, consequently, graphene shows good electrical conductivity at room temperature.

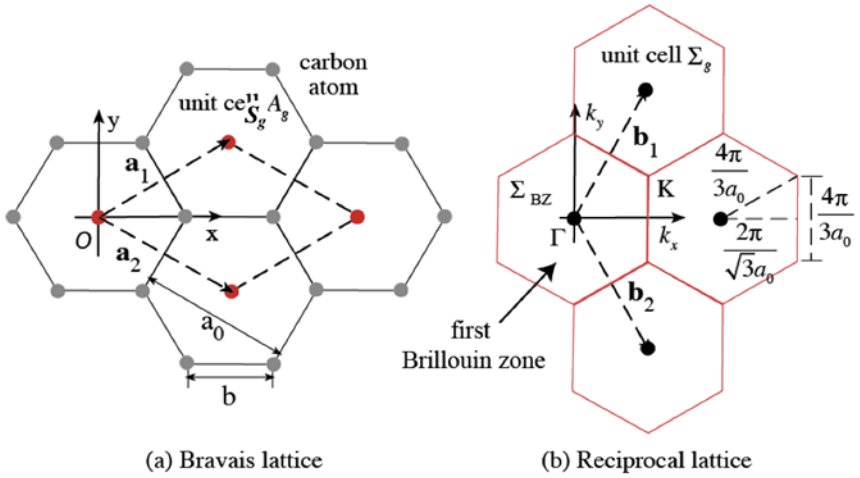

Figure 2.1: Lattice structure of graphene.[1] (a) The Bravais lattice, (b) the reciprocal lattice.

Using the nearest-neighbor tight-binding approximation, the π-electrons dispersion relation is given as:[1]

$$E^{(\pm)}(k) \pm \gamma \left[1 + 4cos\left(\frac{\sqrt{3k_x}a_0}{2}\right)cos\left(\frac{k_y a_0}{2}\right) + 4cos^2\left(\frac{k_y a_0}{2}\right)\right]^{1/2} \ldots(1)$$

E^+ is the energy of the conduction band, while E^- is the energy of the valence band. γ is the carbon-carbon interaction energy, 2.7 eV. Figure 2.2 shows the energy dispersion (E-K) relation. The two non-equivalent carbon atoms in each lattice result in two distinct intersections (K and K') in the Brillouin zone with a linear energy-momentum dispersion (equation 2) at the K-point as shown in Figure 2.2

This intersection is the Dirac point, which corresponds to the Fermi level of graphene. Consequently, graphene has a zero bandgap.

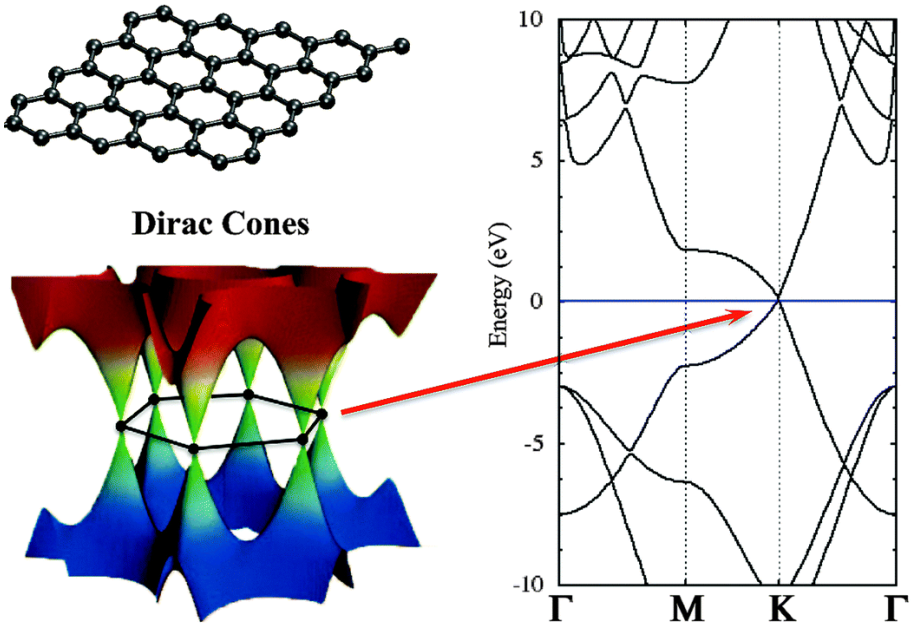

Figure 2.2: Schematic (top right) and band structure of single-layer graphene (left) showing Dirac cone (bottom left) and Dirac point (red arrow).[2]

$$E^{(\pm)} \approx \pm \hbar v_F |k - k_0| \qquad (2)$$

where k_0 is the wavenumber at the Dirac point, v_F is the Fermi velocity ≈ 0.87 x 10^6 m/s and $\hbar$ is the Planck constant

2.1.2 Electronic transport around the Fermi level

Application of an electric field across a device results in the flow of electric current due to a lowering of the potential in one electrode (drain) and a simultaneous rise in the potential of the other electrode (source). Consequently, states in the channel around this energy are filled/emptied resulting in electrical conduction due to the flow of electrons/holes. The probability of occupancy of an electronic state is defined by the Fermi function (equation 3) such that states with energy > than the chemical potential (μ) have a lower probability of occupancy, while states with energy < μ have a higher probability of occupancy 1.

$$f(\epsilon) = \frac{1}{exp[(\epsilon - \mu)/k_B T] + 1}$$

Since μ, the chemical potential is a function of temperature, at T = 0K, it is clearly defined, $\epsilon = \mu = \epsilon_F$, where ϵ_F is the Fermi energy. Consequently, the Fermi function changes discontinuously from 1 i.e. filled states (below μ) to 0 i.e. empty states (above μ). With rising temperature, however, μ becomes diffuse due to thermal fluctuations resulting in the broadening of the Fermi function. Consequently, it becomes impossible to define a precise Fermi energy. Since at all temperatures, $f(\epsilon)$ = ½ when $\epsilon = \mu$, the concept of a Fermi level which corresponds to the energy at which there is a 50 % probability of occupancy is adopted to describe states around μ.

2.2 Literature review for related researches

2.2.1 Graphene as a sensor channel

Due to graphene's high surface to volume ratio, low noise, high mobility, and high carrier density it has found extensive use in gas sensing detecting even single-molecule adsorption events.[3–6] Gas adsorption on graphene results in changes in the graphene device properties such as its carrier concentration (and consequently its charge neutrality point), resistance, mobility, and density of states.[3,7,8] Therefore, the adsorbed gas acts both as a dopant and a scattering center[8] as shown in Figure 2.3a. Tuning voltage application however modifies these properties, first, a positive tuning voltage capacitively dopes the graphene channel with electrons while a negative tuning voltage depletes the channel of electrons thereby increasing the hole concentration in the channel.[3,8]

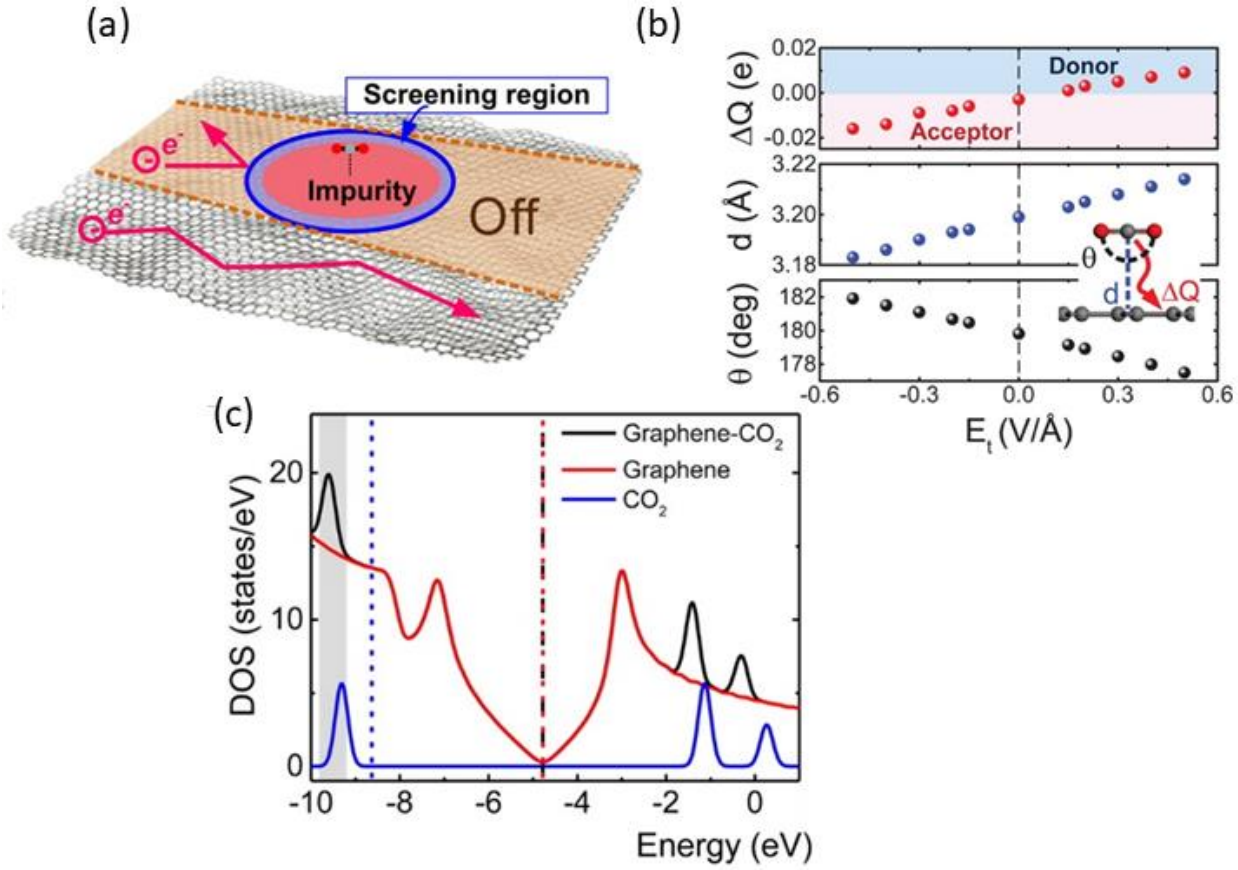

Figure 2.3: Gas adsorption induced modification of graphene electronic properties and density of states.[3] (a) Schematic showing gas adsorption induced doping and scattering, (b) variation of charge transfer, gas adsorption distance, and bond-angle on applied tuning voltage. The x-axis shows applied electric field = $-\frac{tuning\ voltage}{adsorption\ distance}$. (c) CO_2 adsorption induced changes in the density of states in graphene.

Consequently, with positive tuning voltage, the states in the conduction band are occupied and so the graphene channel readily releases electrons to adsorbed gases. Conversely, when a negative tuning voltage is applied, the electrons in the channel are depleted moving the Fermi level into the valence band and emptying occupied states. Thus, the graphene channel has more low energy unoccupied states which can accept electrons from adsorbed gases. As shown in Figures 3b,c these interactions, change the charge transfer characteristics of adsorbed gases on graphene, graphene-gas adsorption distance, and the density of states. Additionally, the adsorption distance, the density

of states, and charge transfer induced by the electrically tunable graphene-molecule van der Waals interaction are unique to the applied electric field.[3]

2.2.2. Dependence of electronic response on gas adsorption sites

Gas adsorption sites on graphene could be defective (e.g. graphene grain boundaries, polymer residues, substrate-induced defects, etc.).[9–11] Pristine graphene obtained via exfoliation is almost defect-free and monocrystalline consequently, it has very high carrier mobility.[4,5] However, while the absence of defects improves pristine graphene's mobility, it also reduces the available defect induced gas adsorption sites. Large area CVD graphene on the other hand is polycrystalline with grains typically larger than a few hundred nanometers.[11,12] Hence it shows lower mobility compared to exfoliated graphene, however, its grain boundaries serve as good adsorption sites for gases while still maintaining good carrier mobility. Indeed, defects in general (including externally induced defects), have been shown to substantially improve the sensing response in graphene sensors as long as the device electronic properties are not utterly degraded.[11,13,14] These properties as well as its scalability make CVD graphene highly sought after for gas sensing applications. Since the adsorption sites in both CVD and pristine graphene are not selective to specific gases, their electronic responses to gases are not selective. Furthermore, in atmospheric air, the high p-doping induced by the O_2/H_2O electrochemical couple makes graphene sensors less useful in atmospheric applications. Consequently, there is increasing interest in high-performance graphene sensors with good gas selectivity, especially in atmospheric air.

Another form of graphene is graphene-oxide, which is typically obtained by chemical oxidation of graphite.[15] Although, it has a reasonable amount of oxidized functional groups (such as carbonyl and epoxy groups) which could reduce p-doping in humid air,[15] its highly defective

nature results in relatively poor electronic properties with carrier mobility and conductivity values as low as $5cm^2/V.S$ and 1500 Scm^{-1} respectively[16] often requiring special treatment such as joule heating at 3000 K,[16] laser deposition[17] or microwave reduction[17] to improve the electrical properties.

As earlier stated, gas adsorption generally results in both doping (i.e. charge transfer) and carrier scattering on the graphene channel.[18] Although carrier mobility has been reported to decrease with gas adsorption due to scattering,[19] an increase in carrier mobility with gas adsorption has also been observed.[8,20] Such an increase in carrier mobility upon gas adsorption has been attributed to the compensation of charged impurities on the graphene channel by gas molecules with opposite doping characteristics (e.g. adsorption of an n-doping gas on p-type charge defect).[8,20] Consequently, gas adsorption on pristine sites and morphological defects such as grain boundaries results in a decrease in carrier mobility[8,19] (or no change in mobility[5,19]) as the adsorbed gases act as scattering centers,[19] however adsorption of gas molecules on charged impurities with an opposite charge, resulting in an increase in mobility due to compensation of charges.[8,20]

2.2.3. Inducing Selectivity and Molecular Identification in Graphene Sensors

Although graphene has demonstrated extreme sensitivity to gases, its lack of selectivity is a major drawback as highlighted in the previous sections. A common strategy to overcome this has been the functionalization of graphene with nanoparticles and polymers[21] or the use of gas-specific generation recombination noise frequencies in the 1/f noise spectra of graphene upon exposure to certain gases (Figure 2.4a). The 1/f noise method is promising both for selective detection and molecular identification of gases.[6,22] However, some gases do not show any characteristic peak,[6] also the 1/f noise measurement set-up requires a “clean bias source” due to

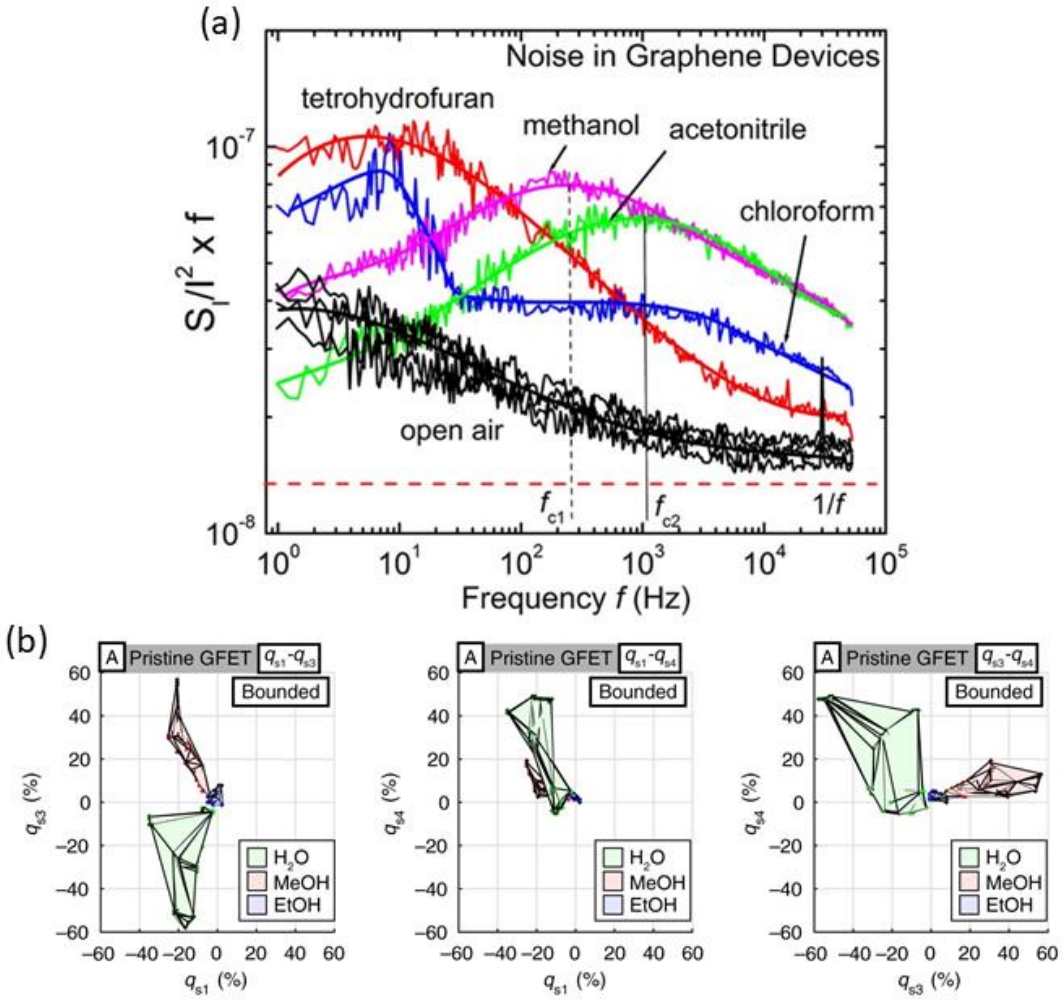

Figure 2.4: Molecular identification techniques. (a) 1/f noise in graphene gas sensors showing gas specific generation-recombination bulges in the 1/f noise spectrum of graphene.[6] (b) Pattern recognition ML algorithm showing the gas specific patterns. q_{s1}, q_{s3}, and q_{s4} represent gas adsorption induced changes in electron mobility, hole mobility, and residual carriers respectively.[23]

the low noise levels in graphene, making the measurement set-up a bit robust. Additionally, the aforementioned methods (graphene functionalization and 1/f noise signals) for inducing selectivity to graphene sensors are typically used in dry air or other inert environments (due to the huge p-doping in atmospheric air), while actual applications require such demonstrations in atmospheric air. Consequently, these methods are unsuitable for atmospheric applications.

In recent times, the use of machine learning (ML) algorithms for pattern recognition of gas

adsorption signals has been shown to induce molecular identification properties inducing "electronic nose (e-nose)" characteristics to graphene sensors (Figure 2.4b). Typically, e-nose sensors use either an array of sensors specifically functionalized for individual gases or a single graphene sensor.[23,24] Generally, the performance of ML algorithms improves with the functionalization of graphene due to increased specificity in the obtained signals.[23,24] However, considering the huge number of gases of interest in applications such as environmental monitoring, the use of functionalized sensor arrays tailored to individual gases is quite cumbersome, consequently, there has been increasing interest in the use of single graphene sensors. Recently, a single graphene sensor was used to identify ethanol, methanol, and water in humid air. However, the performance of the e-nose sensor was shown to be largely dependent on the specificity of the gas adsorption signals measured.[23]

Hence developing gas specific electronic responses with facile measurement methods remain a priority in graphene e-nose sensing. In this regard, the specificity of the electrically tunable charge transfer between the adsorbed gases and graphene holds huge promise for molecular identification in graphene sensors.[3,8,25] Key requirements for the deployment of such charge-based molecular identification methods include: (i) partial stability in the graphene-molecule van der Waals bonding,[25] (so that it's doping characteristics can be experimentally measured) and (ii) facile and reversible switching between different electrically induced vdW bonding states in real-time.

References

(1) Maffucci, A.; Miano, G. Electrical Properties of Graphene for Interconnect Applications. *Appl. Sci.* **2014**, *4* (2), 305–317. https://doi.org/10.3390/app4020305.

(2) Miró, P.; Audiffred, M.; Heine, T. An Atlas of Two-Dimensional Materials. *Chemical Society Reviews*. Royal Society of Chemistry September 21, 2014, pp 6537–6554. https://doi.org/10.1039/c4cs00102h.

(3) Muruganathan, M.; Sun, J.; Imamura, T.; Mizuta, H. Electrically Tunable van Der Waals Interaction in Graphene–Molecule Complex. *Nano Lett.* **2015**, *15* (12), 8176–8180. https://doi.org/10.1021/acs.nanolett.5b03653.

(4) Sun, J.; Muruganathan, M.; Mizuta, H. Room Temperature Detection of Individual Molecular Physisorption Using Suspended Bilayer Graphene. *Sci. Adv.* **2016**, *2* (4), e1501518–e1501518. https://doi.org/10.1126/sciadv.1501518.

(5) Schedin, F.; Geim, A. K.; Morozov, S. V.; Hill, E. W.; Blake, P.; Katsnelson, M. I.; Novoselov, K. S. Detection of Individual Gas Molecules Adsorbed on Graphene. *Nat. Mater.* **2007**, *6* (9), 652–655. https://doi.org/10.1038/nmat1967.

(6) Rumyantsev, S.; Liu, G.; Shur, M. S.; Potyrailo, R. A.; Balandin, A. A. Selective Gas Sensing with a Single Pristine Graphene Transistor. *Nano Lett.* **2012**, *12* (5), 2294–2298. https://doi.org/10.1021/nl3001293.

(7) Cadore, A. R.; Mania, E.; Alencar, A. B.; Rezende, N. P.; de Oliveira, S.; Watanabe, K.; Taniguchi, T.; Chacham, H.; Campos, L. C.; Lacerda, R. G. Enhancing the Response of NH3 Graphene-Sensors by Using Devices with Different Graphene-Substrate Distances. *Sensors Actuators B Chem.* **2018**, *266*, 438–446. https://doi.org/10.1016/j.snb.2018.03.164.

(8) Liu, Y.; Liu, H.; Chu, Y.; Cui, Y.; Hayasaka, T.; Dasaka, V.; Nguyen, L.; Lin, L. Defect-Induced Gas Adsorption on Graphene Transistors. *Adv. Mater. Interfaces* **2018**, *5* (9), 1701640. https://doi.org/10.1002/admi.201701640.

(9) Kumar, B.; Min, K.; Bashirzadeh, M.; Farimani, A. B.; Bae, M.-H.; Estrada, D.; Kim, Y. D.; Yasaei, P.; Park, Y. D.; Pop, E.; et al. The Role of External Defects in Chemical Sensing of Graphene Field-Effect Transistors. *Nano Lett.* **2013**, *13* (5), 1962–1968. https://doi.org/10.1021/nl304734g.

(10) Yasaei, P.; Kumar, B.; Hantehzadeh, R.; Kayyalha, M.; Baskin, A.; Repnin, N.; Wang, C.; Klie, R. F.; Chen, Y. P.; Král, P.; et al. Chemical Sensing with Switchable Transport Channels in Graphene Grain Boundaries. *Nat. Commun.* **2014**, *5* (1), 1–8. https://doi.org/10.1038/ncomms5911.

(11) Salehi-Khojin, A.; Estrada, D.; Lin, K. Y.; Bae, M.-H.; Xiong, F.; Pop, E.; Masel, R. I. Polycrystalline Graphene Ribbons as Chemiresistors. *Adv. Mater.* **2012**, *24* (1), 53–57. https://doi.org/10.1002/adma.201102663.

(12) Huang, P. Y.; Ruiz-Vargas, C. S.; Van Der Zande, A. M.; Whitney, W. S.; Levendorf, M. P.; Kevek, J. W.; Garg, S.; Alden, J. S.; Hustedt, C. J.; Zhu, Y.; et al. Grains and Grain Boundaries in Single-Layer Graphene Atomic Patchwork Quilts. *Nature* **2011**, *469* (7330), 389–392. https://doi.org/10.1038/nature09718.

(13) Hajati, Y.; Blom, T.; Jafri, S. H. M.; Haldar, S.; Bhandary, S.; Shoushtari, M. Z.; Eriksson, O.; Sanyal, B.; Leifer, K. Improved Gas Sensing Activity in Structurally Defected Bilayer Graphene. *Nanotechnology* **2012**, *23* (50), 505501. https://doi.org/10.1088/0957-4484/23/50/505501.

(14) Lee, G.; Yang, G.; Cho, A.; Han, J. W.; Kim, J. Defect-Engineered Graphene Chemical Sensors with Ultrahigh Sensitivity. *Phys. Chem. Chem. Phys.* **2016**, *18* (21), 14198–14204. https://doi.org/10.1039/C5CP04422G.

(15) Some, S.; Xu, Y.; Kim, Y.; Yoon, Y.; Qin, H.; Kulkarni, A.; Kim, T.; Lee, H. Highly Sensitive and Selective Gas Sensor Using Hydrophilic and Hydrophobic Graphenes. *Sci. Rep.* **2013**, *3* (1), 1–8. https://doi.org/10.1038/srep01868.

(16) Wang, Y.; Chen, Y.; Lacey, S. D.; Xu, L.; Xie, H.; Li, T.; Danner, V. A.; Hu, L. Reduced Graphene Oxide Film with Record-High Conductivity and Mobility. *Mater. Today* **2018**, *21* (2), 186–192. https://doi.org/10.1016/j.mattod.2017.10.008.

(17) Bhaumik, A.; Haque, A.; Taufique, M.; Karnati, P.; Patel, R.; Nath, M.; Ghosh, K. Reduced Graphene Oxide Thin Films with Very Large Charge Carrier Mobility Using Pulsed Laser Deposition. *J. Mater. Sci. Eng.* **2017**, *06* (04). https://doi.org/10.4172/2169-0022.1000364.

(18) Hwang, E. H.; Adam, S.; Das Sarma, S. Transport in Chemically Doped Graphene in the Presence of Adsorbed Molecules. *Phys. Rev. B* **2007**, *76* (19), 195421. https://doi.org/10.1103/PhysRevB.76.195421.

(19) Blechta, V.; Drogowska, K. A.; Vales, V.; Kalbac, M. Adsorption Site-Dependent Mobility Behavior in Graphene Exposed to Gas Oxygen. *J. Phys. Chem. C* **2018**, *122* (37), 21493–21499. https://doi.org/10.1021/acs.jpcc.8b06906.

(20) Cao, G.; Liu, X.; Liu, W.; Li, Q.; Li, X.; Wang, X. Chemical Environment Dominated Fermi Level Pinning of a Graphene Gas Sensor. *Carbon N. Y.* **2017**, *124*, 57–63. https://doi.org/10.1016/J.CARBON.2017.08.026.

(21) Georgakilas, V.; Otyepka, M.; Bourlinos, A. B.; Chandra, V.; Kim, N.; Kemp, K. C.; Hobza, P.; Zboril, R.; Kim, K. S. Functionalization of Graphene: Covalent and Non-Covalent Approaches, Derivatives and Applications. *Chemical Reviews*. American Chemical Society November 14, 2012, pp 6156–6214. https://doi.org/10.1021/cr3000412.

(22) Amin, K. R.; Bid, A. Effect of Ambient on the Resistance Fluctuations of Graphene. *Appl. Phys. Lett.* **2015**, *106* (18), 183105. https://doi.org/10.1063/1.4919793.

(23) Hayasaka, T.; Lin, A.; Copa, V. C.; Lopez, L. P.; Loberternos, R. A.; Ballesteros, L. I. M.; Kubota, Y.; Liu, Y.; Salvador, A. A.; Lin, L. An Electronic Nose Using a Single Graphene FET and Machine Learning for Water, Methanol, and Ethanol. *Microsystems Nanoeng.* **2020**, *6* (1), 1–13. https://doi.org/10.1038/s41378-020-0161-3.

(24) Liu, B.; Huang, Y.; Kam, K. W.; Cheung, W. F.; Zhao, N.; Zheng, B. Functionalized Graphene-Based Chemiresistive Electronic Nose for Discrimination of Disease-Related Volatile Organic Compounds. *Biosens. Bioelectron. X* **2019**, *1*, 100016. https://doi.org/10.1016/j.biosx.2019.100016.

(25) Agbonlahor, O. G.; Muruganathan, M.; Imamura, T.; Mizuta, H. Adsorbed Molecules as Interchangeable Dopants and Scatterers with a Van Der Waals Bonding Memory in

Graphene Sensors. *ACS Sensors* **2020**, *5* (7), 2003–2009. https://doi.org/10.1021/acssensors.0c00403.

Chapter 3

Porous Activated Carbon Functionalized CVD-Graphene Ammonia Gas Sensor

As discussed in chapter 2, huge p-doping of CVD graphene when exposed to atmospheric air results in poor gas sensitivity and selectivity. Consequently, demonstrations of graphene's sensitivity and suitability for applications such as environmental monitoring and non-invasive medical diagnosis are often done in inert environments such as nitrogen and dry air, although actual environmental and clinical sensors will ultimately be used in atmospheric conditions. Hence, in this chapter, the morphological characteristics, electronic and gas sensing properties of an activated carbon functionalized graphene field-effect transistor (a-CF-GFET) room temperature ammonia sensor with 500 parts per trillion (ppt) of ammonia sensitivity in atmospheric air and a response time of < 3 seconds is presented.

3.1. The Menace of Atmospheric Doping of Graphene

Graphene's low noise, 2D nature, high mobility, and single-molecule sensitivity makes it highly sought after for various applications including ultra-sensitive gas sensors.[1–3] However, its ubiquitous commercialization as the ultimate sensing materials is inhibited by its poor selectivity and high p-doping in atmospheric air.[4] Addressing these challenges often involve metal nanoparticles/organic 'functionalization' of the graphene surface or the observation of gas-specific generation-recombination Lorentzian 'peaks' in graphene's 1/f noise spectra.[1,5,6] Nevertheless, since these methods are typically demonstrated in inert environments insights on their utility for commercial environmental and clinical gas sensor applications are limited. Additionally, for

commercial applications, the sensor fabrication process should be scalable and lithographically compatible. These requirements make porous activated carbon (a-C) suitable for this application since it is easily generated by chemical/lithographic modification and subsequent pyrolysis of polymeric precursors such as Novolac resin[7–9] while possessing good gas molecular sieving properties and ammonia selectivity.[10–13] High sensitivity ammonia detection is required for environmental monitoring and non-invasive diagnosis of urea cycle disorder,[14] kidney problems,[15,16] and ulcers resulting from *Helicobacter pylori* bacterial infection in the stomach.[15]

3.2. Experimental methods

3.2.1 Fabrication of activated carbon functionalized graphene devices

Monolayer CVD graphene on Cu substrate was purchased from the graphene platform and used as obtained. The obtained CVD sample comprised of monolayer graphene grown on Cu substrate and sandwiched between a bottom plastic film, and protective top plastic. For the transfer to SiO_2/Si substrate, a ~ 15mm x 10mm sample was cut and the protective top plastic peeled off. Thereafter, the exposed CVD graphene was spin-coated with polymethyl methacrylate (PMMA) resist at 4000 revolutions per minute followed by heating in a hot plate at about ~150 ^oC to remove the bottom plastic film. The backside of the copper film was plasma etched to remove any graphene that might have been deposited during the CVD growth process. The PMMA coated graphene on Cu film was made to float in 0.1M ammonium persulphate etching solution with the PMMA coated surface facing up. After ~6 hours, the Cu film was completely etched, and the PMMA coated graphene was picked up using a watch glass, transferred to a beaker of water, and rinsed for 5 minutes. This rinsing was repeated twice, and then the floating CVD graphene was picked up using a 285nm SiO_2/Si wafer and allowed to dry in atmospheric air in a slanted position. The coated PMMA was stripped off graphene using acetone and rinsed in isopropanol. Finally, the transferred graphene

was annealed in Ar/H_2 environment at about 300 ^oC for 3 h to remove any residual PMMA on graphene. Before graphene transfer, the Si/SiO_2 substrate was cleaned in acetone and isopropanol. Oxygen plasma etching was not used as it increases susceptibility to wetting by atmospheric moisture.[17]

Next, electrodes (Cr/Au) were deposited using typical lithographic techniques, followed by metal evaporation and lift-off. The graphene nanoribbon was defined by electron beam lithography (dose = 100μC/cm) using a negative Novolac resin-based resist (ARN 7520.07) followed by resist development and oxygen plasma etching (Flow rate = 20 Sccm, time = 35s, Pressure = 6Pa, RF = 20W). The as-fabricated device was annealed at 300 ^oC for 3.5h in vacuum to convert the post-lithographic resist into activated carbon. During pyrolysis, the heater was ramped to 300 degrees at ~30 ^oC per minute. Before all the lithographic resist coating steps above, the substrate was rinsed for few minutes in acetone and subsequently, IPA followed by pre-heating at 180 degrees for 5 minutes to remove adsorbed water on the chip. This pre-heating and cleaning step helps reduce the p-doping in the fabricated device when exposed to atmospheric air.

3.3. Gas sensing measurement

3.3.1. Detection of gas by CNP shift

All gases used in this study were either pure (99.9%) or diluted in nitrogen. Measurements in atmospheric air were done at atmospheric conditions in an isolated laboratory. Concentrations in parts per volume were measured with respect to the chamber volume (2L).

In Dry Air*:* After recovering the device in vacuum (by annealing at 150 ^oC for about 1-3 h or vacuuming overnight) the transfer characteristic of the device was obtained in vacuum. Thereafter, 155 Torr of oxygen and I55 Torr nitrogen were introduced into the chamber using mass flow controllers (MFCs), followed by the desired concentration of ammonia. Afterward, the total

pressure in the chamber was increased to 710 Torr by introducing nitrogen and the transfer characteristic measured.

In Atmospheric Air: After recovering the device in vacuum (by annealing at 150 ^{o}C for about 2-3 h or vacuuming overnight) the transfer characteristic in vacuum was obtained. Thereafter the device was exposed to air for 1 minute after which the transfer characteristic was measured. For 200 ppb in atmospheric air using the device fabricated without standard cleaning and pre-heating, exposure to air was for only 10s. This was followed by introducing the desired concentration of the analyte gas and subsequently transfer characteristics measurement.

3.4. Morphological Characteristics of the a-CF-GFET sensor

The porous activated carbon device is shown by the schematic, Raman characterization, and atomic force microscope (AFM) imaging (Figures 3.1a,b). The broad peak at 1200 cm^{-1}- 1500 cm^{-1} in the Raman spectra (Figure 3.1a, right) confirms the presence of activated carbon[18] (a-C) on the graphene surface. The thickness of the a-C was found to be about ~38 nm based on AFM imaging (Figure 1b). Lithographic patterning induces crosslinking in the resist making the lithographically patterned a-C more fibrous (Figure 3.1c, left) compared to the uncrosslinked a-C (Figure 3.1c, right). The plasma oxidation step simultaneously etches away exposed graphene and oxidizes the surface of the a-C as shown in the EDX maps and spectra (Figures 3.1d and 3.2) such that the pores leading to graphene are surrounded by oxidized a-C walls. This oxidation facilitates good ammonia selectivity[10] and minimal p-doping in atmospheric air.[19]

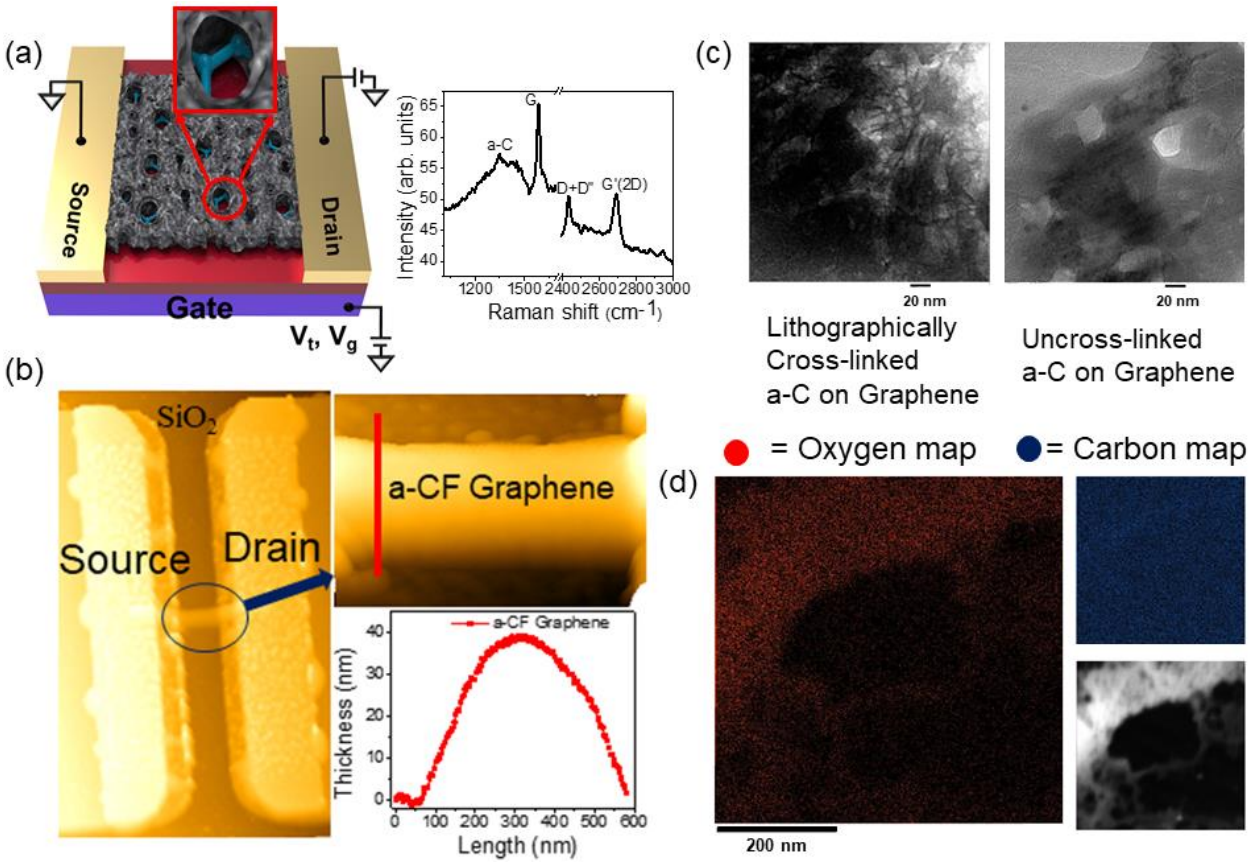

Figure 3.1: Morphological characteristics of the a-CF-GFET sensor. (a) Device schematics of the a-CF-GFET sensor showing porous a-C on graphene (left) and Raman spectra of the a-CF-GFET sensor showing broad a-C peak (right) (b) AFM image showing 38 nm a-C on graphene (c) TEM image (bright field) showing the fibrous nature of the lithographically cross-linked a-C on the graphene (left), and the more amorphous uncrosslinked a-C on graphene (right). Dark regions are activated carbon, while bright regions are pores leading to graphene. Scale bars in both images are 20 nm. (d) EDX mapping of oxygen around a-C pores on graphene (left) showing minimal oxygen in pores and more oxygen on the surrounding a-C. Top-right is the EDX carbon map of the same region. The bottom right image is the dark field TEM image of the same a-C region on graphene used in EDX mapping. Bright regions are the activated carbon while the dark regions are the pores.

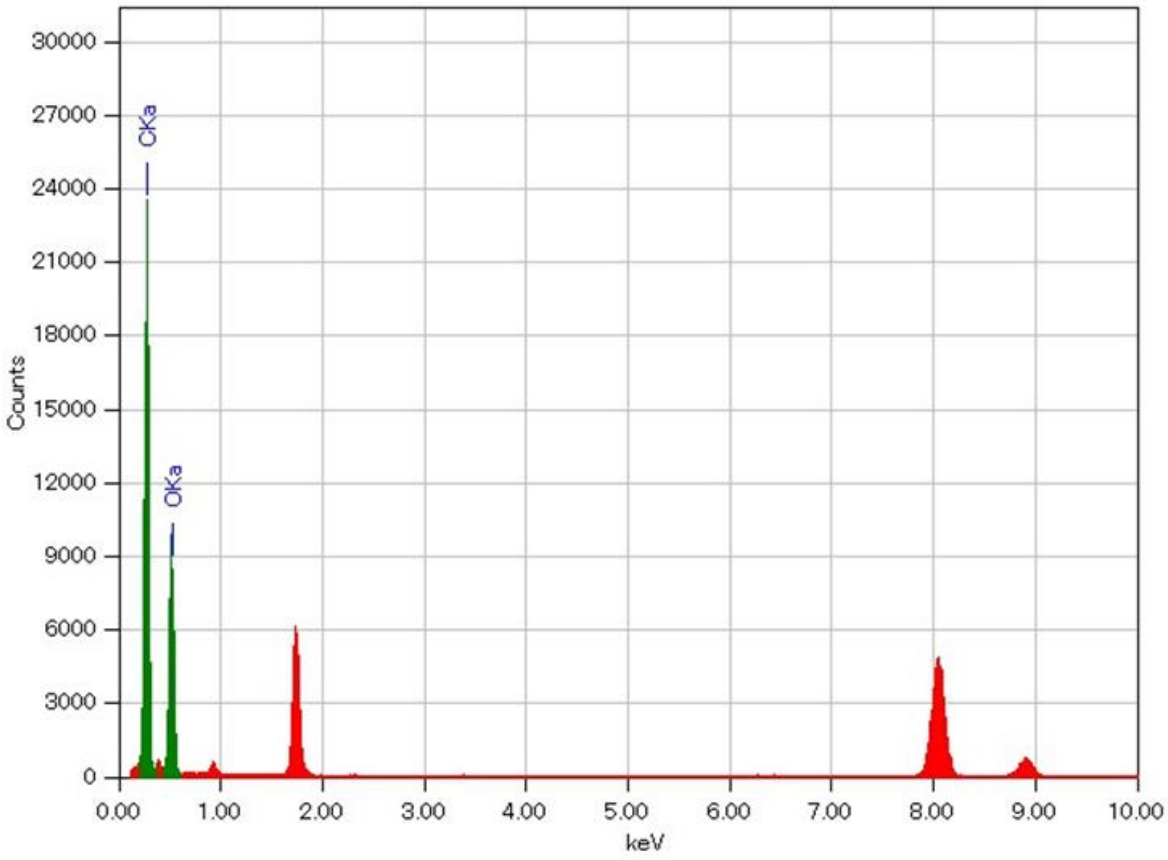

Figure 3.2: EDX spectra of the a-CF-graphene showing the presence of carbon and oxygen (green peaks). Red peaks represent copper from the TEM grid.

3.5. Electrical Characteristics of the a-CF-GFET sensor

The I-V plot, transfer characteristics, and field-effect mobility of the as-fabricated devices before and after pyrolysis are shown in Figures 3.3 a-e. The devices showed ohmic conductance before and after pyrolysis with an increase in resistance after pyrolysis. The increased resistance in the pyrolyzed devices may be attributed to a decrease in carrier concentration due to the desorption of charged impurities on the fabricated device during pyrolysis. The devices generally showed high field-effect carrier mobility increasing with aspect ratio (Figure 3.3e) and rising to about 3500 cm^2/Vs for an aspect ratio of about 6.6 (Figure 3.3d).

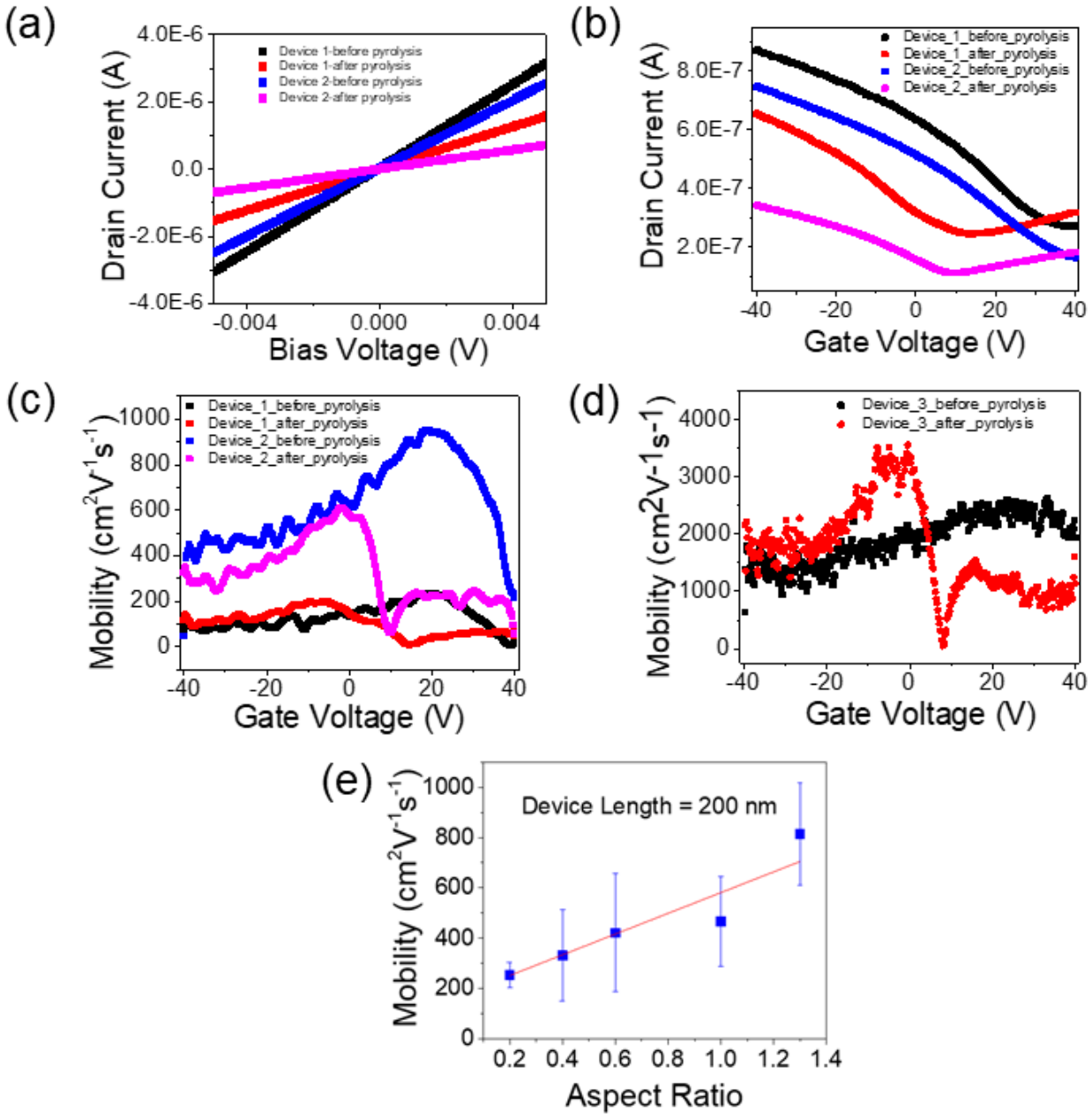

Figure 3.3: Electrical characterization of a-CF-GFET device (a) I-V characteristics of two sample devices with dimensions: length = 0.2 µm, width = 1µm (Device_1), and length = 0.5 µm, width = 0.5µm (Device_2) (b) transfer characteristics of the devices in (a) (c) field effect mobility of devices in (a) (d) field effect mobility of a 1 um x 0.15 nm device showing a hole mobility of 3500 $cm^2V^{-1}s^{-1}$ after pyrolysis (e) variation of the field effect mobility of 200 nm length devices with different aspect ratio (length/width).

3.6. Gas Sensing Response of the a-CF-GFET Sensor

The a-CF-GFET sensor showed the typical p-type doping response to dry air (Figure 3.4a), no response to nitrogen (Figure 3.4b), and p-doping to atmospheric air (Figure 3.3c). Generally, the p-doping in air was mild (device CNP was <20 V even after 40 mins (Figure 3.4c) compared to pristine CVD graphene, whose CNP could not be observed in air. It is important to note that standard cleaning in acetone and isopropanol and pre-heating (before resist coating) as discussed in the experimental section, helps minimize p-doping in air (Figures 3.4c, and 3.5a,b). The cleaning involved washing in acetone and isopropanol and subsequent heating at 180 ^{o}C for 5 minutes to remove adsorbed water on the chip before resist coating. Otherwise stated, results were obtained from devices fabricated with standard cleaning and pre-heating.

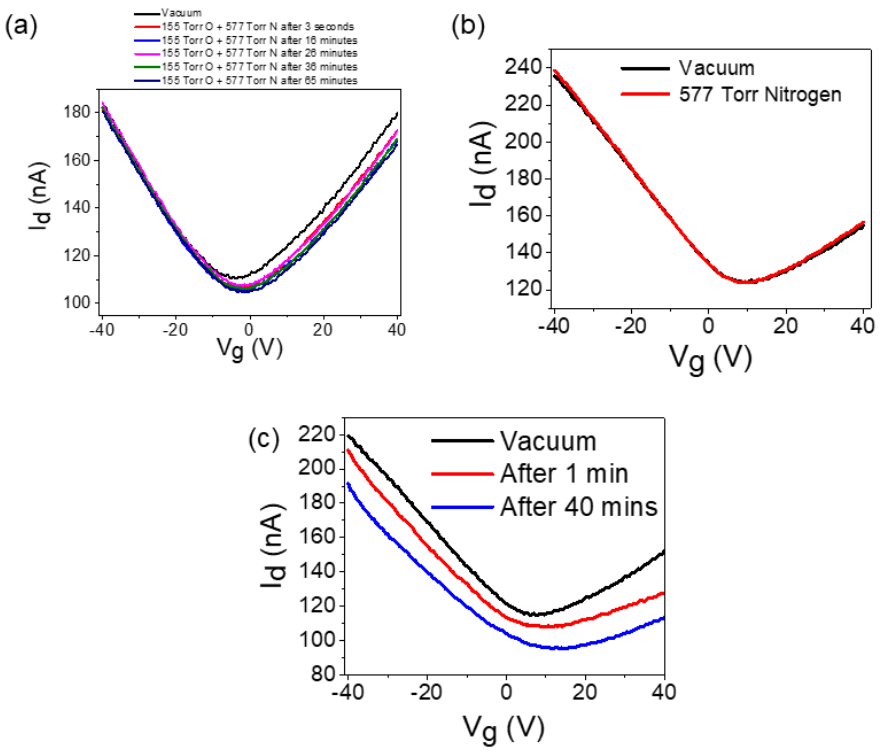

Figure 3.4: Doping response of the a-CF-GFET sensor with acetone and isopropanol cleaning, and pre-heating fabrication steps. (a) Dry air, (b) Nitrogen (after 3 seconds) (c) Atmospheric air after 1-minute exposure and after 40 minutes.

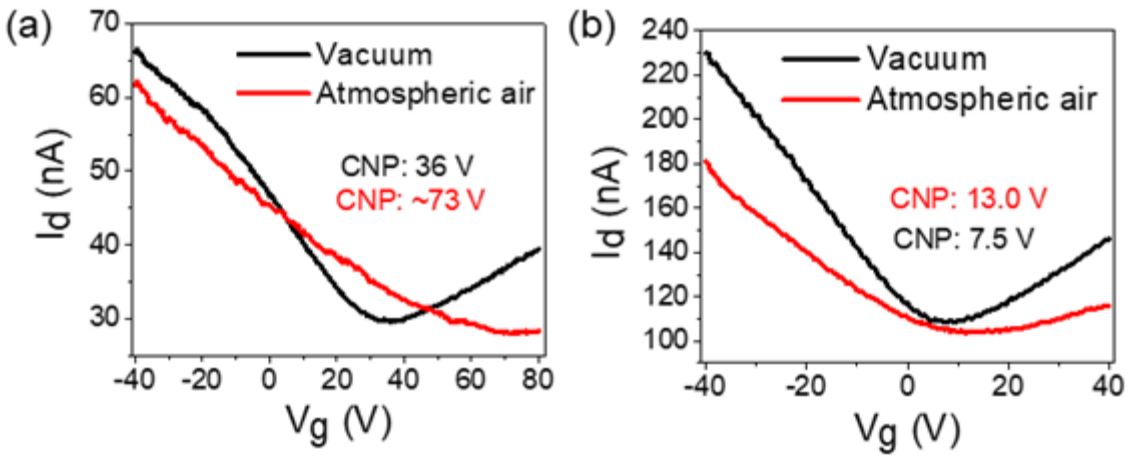

Figure 3.5: Observed p-doping in a-CF-GFET sensor exposed to atmospheric air. (a) Device response after 10 seconds of exposure to atmospheric air for the a-CF-GFET device fabricated without standard cleaning and pre-heating. (b) Device response after 1-minute exposure to atmospheric air for the a-CF-GFET device fabricated with standard cleaning and pre-heating.

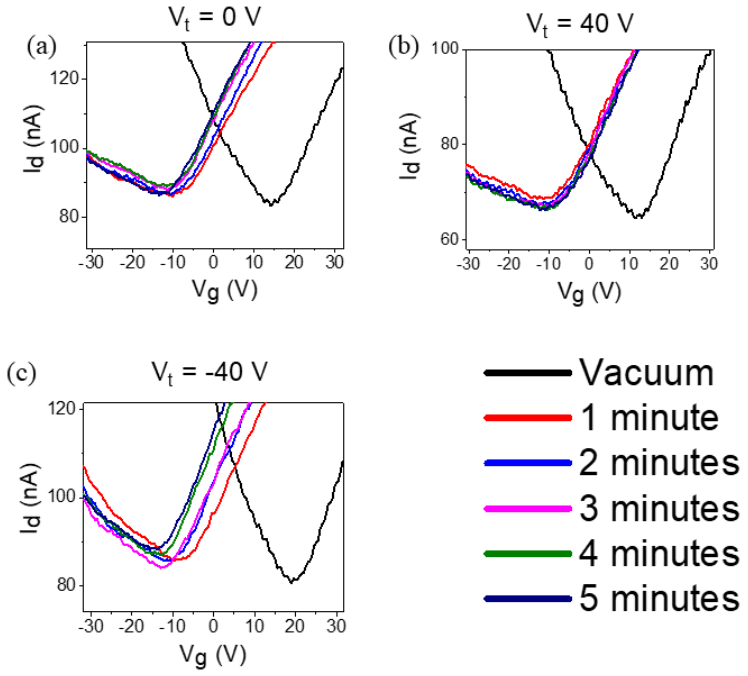

Figure 3.6: Transfer characteristics plot for ammonia adsorption on the a-CF-GFET sensor at different tuning voltages (V_t). (a) V_t = 0 V (b) V_t = 40 V (c) V_t = -40 V. The a-CF-GFET sensor, was changed from its p-doped state to n-doped state due to the n-doping from adsorbed ammonia.

The a-CF-GFET sensor showed n-type response to 84 ppm ammonia in 555 Torr of nitrogen (Figure 3.6a-c) with the doping concentration decreasing with applied back-gate voltage in the order -40 V > 0 V > 40 V in agreement with previous reports for adsorption of ammonia on p-doped graphene.[20–22]

3.7. Gas adsorption induced doping and scattering in a-CF-GFET sensor

To investigate the effect of gas adsorption-induced scattering on the response of the a-CF-GFET sensor, the drain current was monitored at specific tuning voltages of 0 V, -40 V and +40 V separately (Figures 3.7 a-d) applied for 1 minute, 2 minutes, 3 minutes, 4 minutes and 5 minutes (in this order) with ~30 s break taken after each tuning voltage experiment to obtain the transfer characteristics. The corresponding change in field-effect mobility is shown in Figure 3.7e. For the 0 V and -40 V tuning experiments, the a-CF-GFET sensor was originally p-doped before and after V_t application, hence adsorption of ammonia is expected to result in a decrease in conductivity due to electron-hole recombination as observed during the first (1 minute) tuning experiments (Figures 3.7 b,c). After the 1-minute tuning experiments, the a-CF-GFET sensor was n-doped for both tuning voltages (Figures 3.6 a,c) hence, further tuning experiments were expected to increase the conductivity as the residual doping levels increased (Figures 3.6 a,c and 3.8).

It is important to note that the doping concentration measured after applying the V_t does not reflect the exact doping concentration during the V_t experiments, rather it is the residual doping due to V_t modulation of the graphene-molecule van der Waals (vdW) complex interaction.

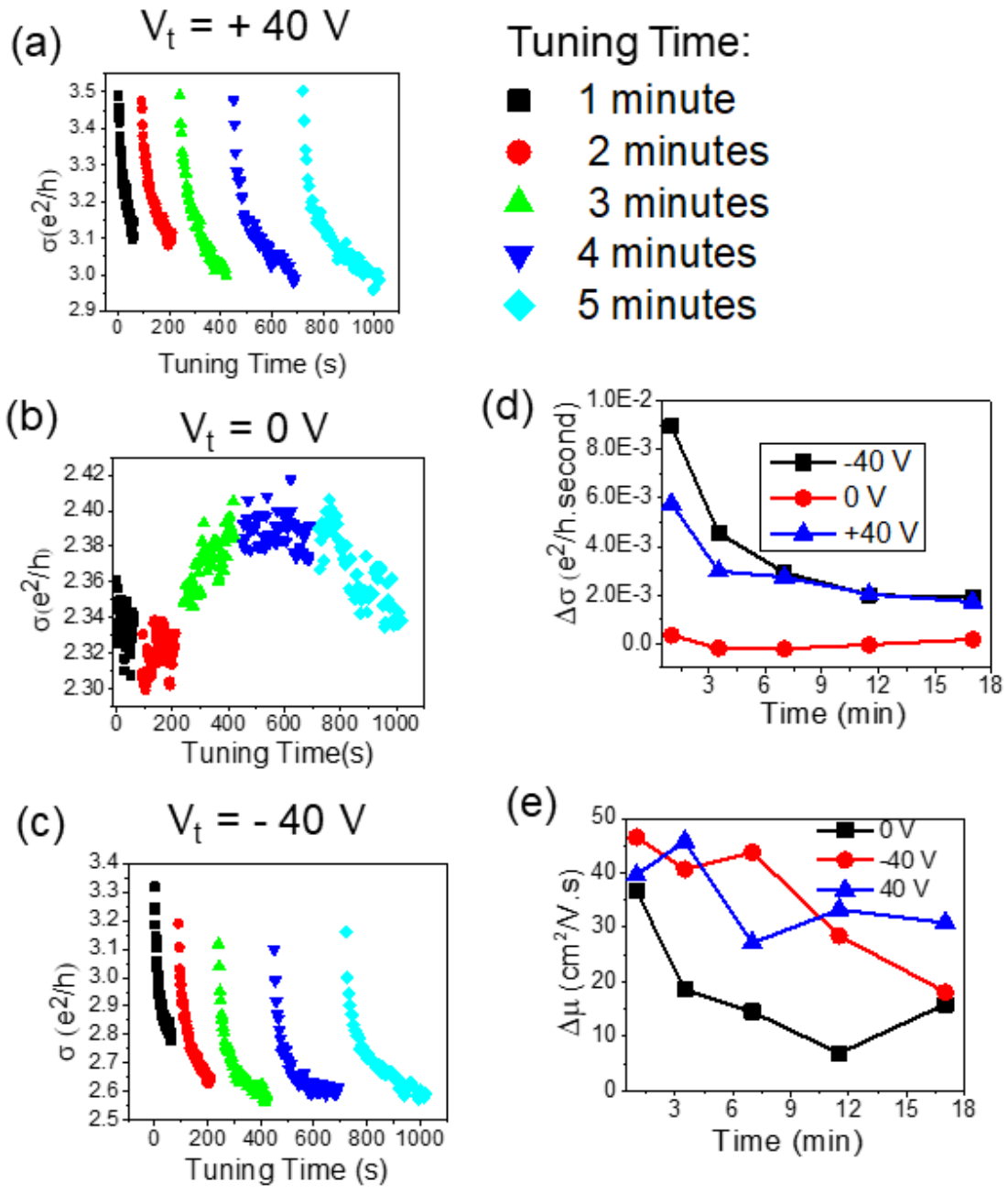

Figure 3.7: Conductivity (σ) response vs time of the a-CF-GFET sensor for (a) V_t = 40 V, (b) V_t = 0 V, and (c) V_t = -40 V. The legend in the top right applies to Figures a-c. (d) Scattering-doping index, Δσ, $(\frac{Initial\ Conductivity(\sigma_i) - Final\ Conductivity(\sigma_f)}{Time})$ for V_t = -40 V, 0 V, 40 V showing minimal scattering for V_t = 0 V. (e) Reduction in field effect mobility ($\Delta\mu = \mu_{\max(vacuum)} - \mu_{\max(gas)}$) due to ammonia gas adsorption for V_t = -40 V, 0 V, 40 V.

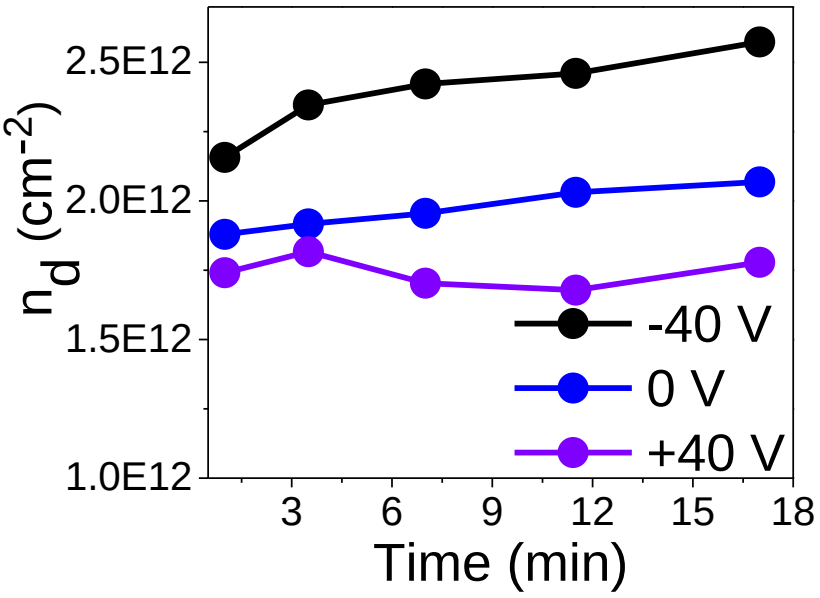

Figure 3.8: Compilation of the results in Figures 3.6 showing a variation of the doping concentration (n_d) with time for 84 ppm ammonia in 555 Torr of N_2 at V_t = -40 V, 0 V, 40 V.

As previously demonstrated, this residual vdW doping has a bonding memory that reflects the nature of charge transfer and carrier scattering during the V_t experiment and so can be used to study doping and scattering effects due to V_t modulation.[23] For the 0 V tuning experiment, the expected increase in conductivity due to carrier accumulation was observed during the 2-minutes and 3-minutes tuning experiments (Figure 3.7b), thereafter the conductivity was stable (during the 4-minutes tuning experiment) and then gradually decreased during the 5-minutes tuning experiment signifying the onset of scattering dominated transport. Since the doping concentration increased consistently during the 0 V tuning experiment (Figure 3.8), the conductivity response during the 1-minute, 2-minutes, and 3-minutes tuning experiments is consistent with doping dominated transport due to carrier accumulation in the channel. For the 40 V tuning experiment, the a-CF-GFET sensor was p-doped before V_t application but electronically n-doped during the V_t

experiment as the applied V_t moves the graphene Fermi level into the conduction band hence n-doping due to ammonia adsorption is expected to result in an increase in conductivity due to carrier accumulation in the channel from ammonia adsorption. However, the conductivity continuously decreased for both the -40 V and 40 V tuning experiments (Figures 3.7 a,c) even after the device was completely n-doped due to ammonia gas adsorption. This continuous decrease in conductivity signifies scattering-dominated transport. The reduction in conductivity may be attributed to both gas adsorption induced scattering, as well as scattering due to activated carbon on the graphene channel.

The competing roles between doping and scattering for the applied tuning voltages are summarized in Figure 3.7d where $(\frac{(\sigma_i - \sigma_f)}{Time})$ vs time, referred to as the scattering-doping index is plotted showing that scattering was in the order -40 V > 40 V > 0 V suggesting that the 0 V tuning experiment has the least scattering despite having higher doping compared to the 40 V vdW complex. This is similar to previous reports for CO_2 adsorption on pristine graphene, in which the 0 V tuning experiment had a lower scattering despite having higher doping concentration. Interestingly for V_t = 0 V, during the 5 minutes tuning experiment where the conductivity decreased and the scattering became dominant, the measured reduction in field-effect mobility ($\Delta\mu = \mu_{\max(vacuum)} - \mu_{\max(gas)}$) also increased (Figure 3.7e) confirming scattering dominated transport. $\mu_{\max(vacuum)}$ is the maximum field-effect electron mobility in vacuum, while $\mu_{\max(gas)}$ represents the maximum field-effect electron mobility in the gas. Though gas adsorption resulted in a decrease in mobility for the 40 V and -40 V tuned complex, the change in mobility in the -40 V and 40 V tuned complexes will be affected by trapped charges in the SiO_2 traps during the V_t experiments hence the relative changes in field-effect mobility (Figure 3.7e) cannot be used to determine the scattering dependence on V_t. This effect has been discussed elsewhere.[23] In

summary, the activated carbon on the graphene channel generally increased both the doping and scattering in graphene.

3.8. Gas Adsorption Mechanism in the a-CF-GFET sensor

The porous nature of the a-C suggests that the adsorbed gases diffuse through the pores of the oxidized activated carbon (which is selective to ammonia gas),[10] to the underlying CVD graphene. The shift in charge neutrality point due to gas adsorption as well as the similarity between pristine graphene's doping-type response and the a-CF-GFET doping-type response to gases, confirms that the observed gas sensing response results from gas adsorption on graphene (underneath the a-C pores). In CVD graphene, defects are the key adsorption sites with their sensitivity increasing with decreasing device sizes,[24–26] consequently in our a-CF-GFET sensor, the main defect adsorption sites on the CVD graphene underneath the a-C pores will be the CVD graphene grain boundaries and the a-C-graphene interface. For all devices used in sensing experiments (i.e. lengths and widths in the range 0.2 - 1μm), ammonia selectivity was observed in nitrogen environment, however in atmospheric air ammonia selectivity was only observed in small devices, ~200 nm in length and width. This may be attributed to the strong p-doping of graphene by atmospheric air as well as the device size dependence of defect dominated gas adsorption typical observed in CVD graphene sensors as discussed below.[24,26] CVD graphene grains are typically a few hundred nanometers or more,[25] hence for a ~200 nm a-CF-GFET device the adsorption sites will be mainly the a-C-graphene interface as the device size limits the possibility of grain boundaries enclosed within the device. Furthermore, graphene samples exposed to air have been reported to show contamination mainly along the grain boundaries,[25] suggesting that grain boundaries are the key adsorption sites for dopants in air. Since with more grain boundaries (as in large devices) the probability for adsorption of dopants in air increases, consequently,

ammonia selectivity is not observed in large devices exposed to atmospheric air due to the adsorption of atmospheric p-dopants (oxygen/H_2O) on the grain boundaries which overcome the n-doping from ammonia adsorption at the a-C-graphene interface. However in ~200nm devices, the predominant adsorption sites will be the a-C-graphene interface as discussed above, hence the adsorption of ammonia is favored due to the ammonia selectivity of the a-C[10] such that the ~200nm devices show ammonia selectivity in atmospheric air, unlike the larger devices. The activated carbon generally promotes gas adsorption induced doping as well as carrier scattering (due to gas adsorption and the activated carbon) on the graphene channel (Figure 3.7). Consequently, the smaller amount of carrier scatters in small devices compared to larger devices could also improve the selective response in small devices by ensuring a better signal-to-noise ratio.

3.9. High sensitivity ammonia detection in dry and atmospheric air

In this work, all results for ammonia detection in air (atmospheric and dry) were obtained from 200nm x 200nm devices. In between the gas sensing experiments, the devices were recovered by annealing at about 150 ^oC for 1-3 h or by vacuuming overnight. The devices generally showed good recovery even by vacuuming for a few hours at room temperature confirming that the gases are physisorbed. The 200nm x 200 nm a-CF-GFET devices showed n-doping response to 500 ppt, 1 ppb, 2 ppb, 5 ppb, 200 ppb, and 84 ppm ammonia gas in atmospheric air and 1 ppb, 2 ppb, 5 ppb, 200 ppb, and 84 ppm ammonia gas in dry air (Figures 3.9 - 3.11).

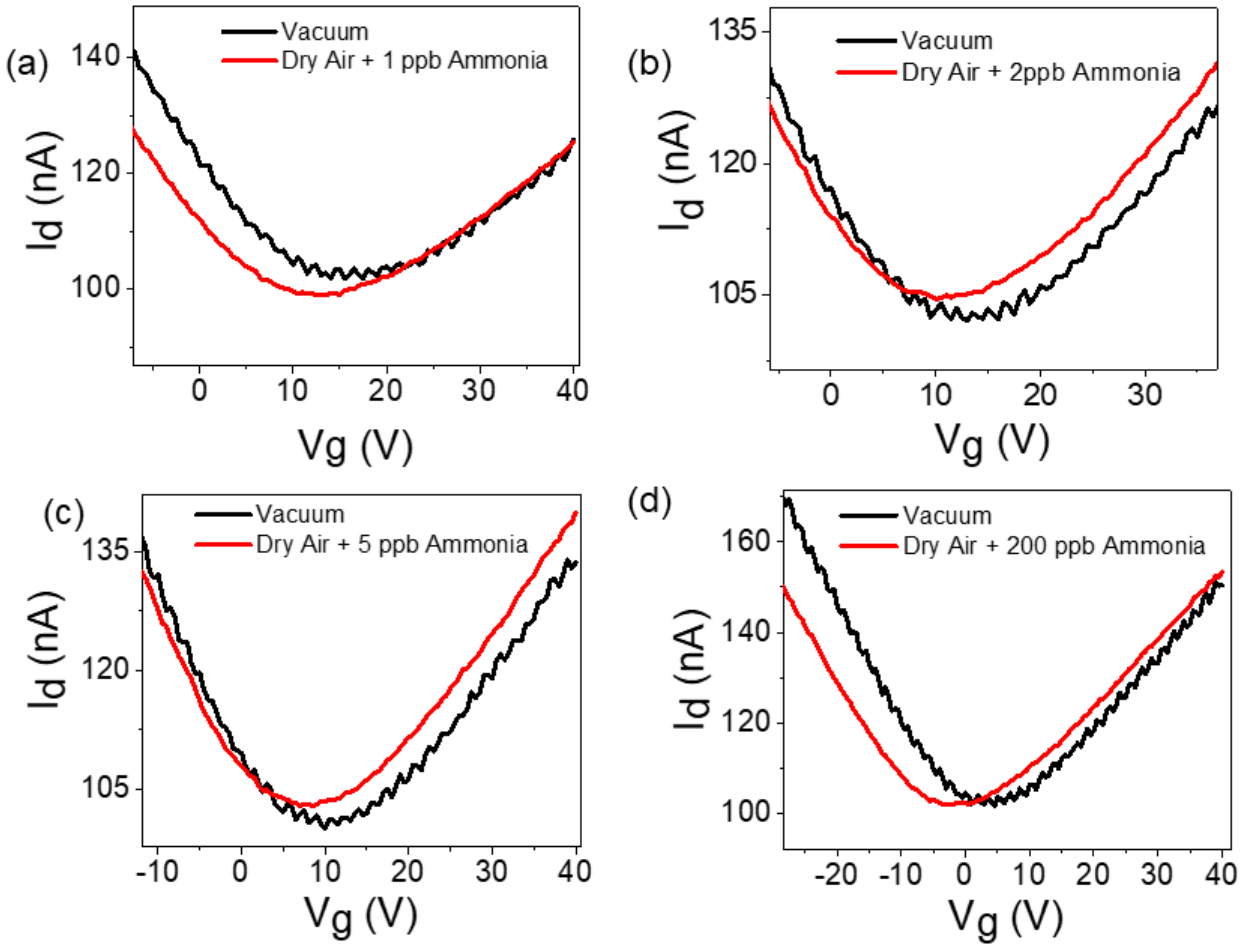

Figure 3.9: n-doping response of the a-CF-GFETs to (a) 1 ppb ammonia (b) 2 ppb ammonia (c) 5 ppb ammonia and (d) 200 ppb ammonia in dry air (155 Torr O_2, 577 Torr N_2).

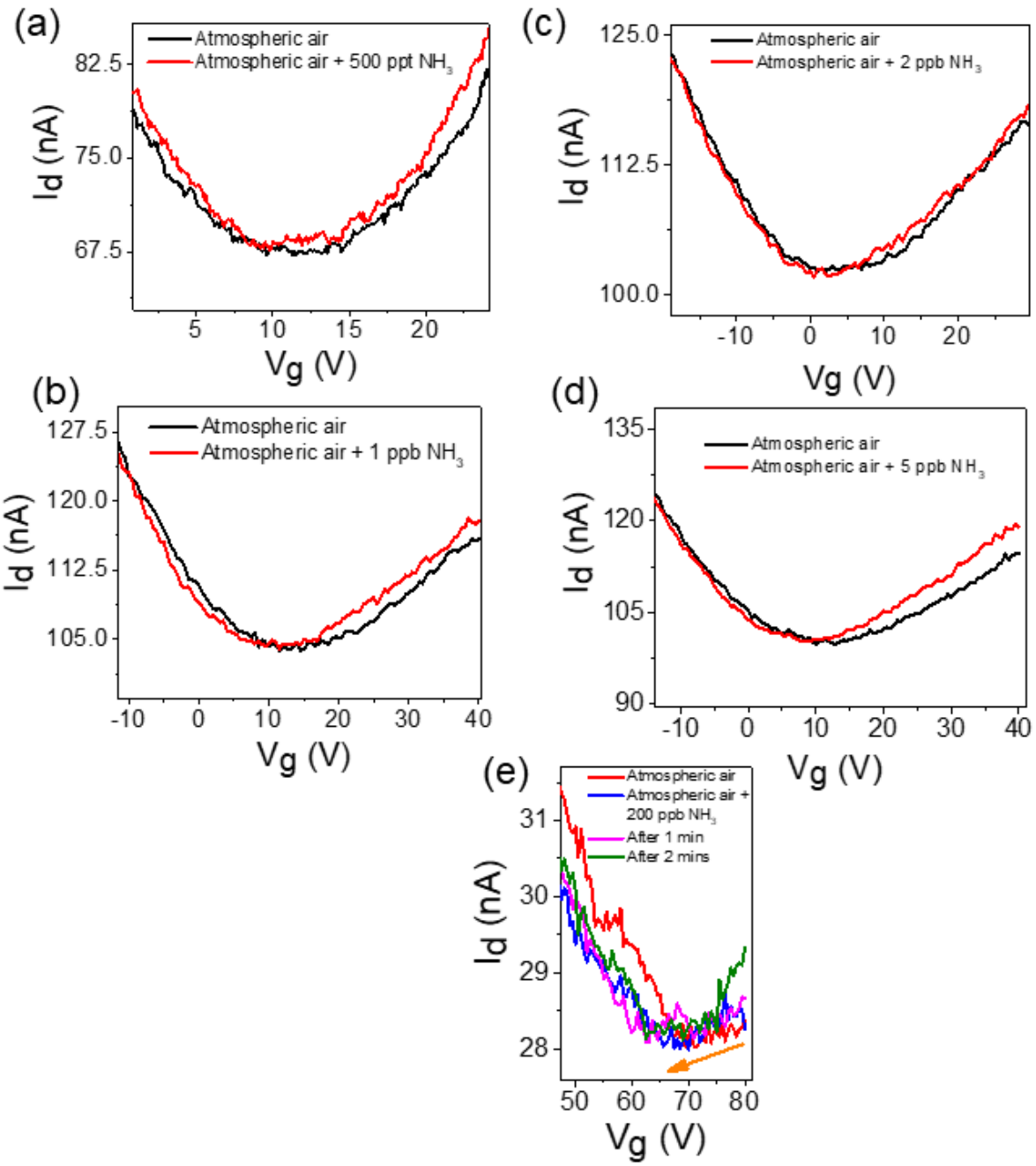

Figure 3.10: CNP shift of a-CF-GFET fabricated with standard cleaning and pre-heating. (a) 500 ppt ammonia in atmospheric air, (b) 1 ppb in atmospheric air (c) 2 ppb ammonia in atmospheric air (d) 5 ppb ammonia in atmospheric air. (e) The response of a-CF-GFET fabricated without standard cleaning and pre-heating to 200 ppb ammonia in atmospheric air.

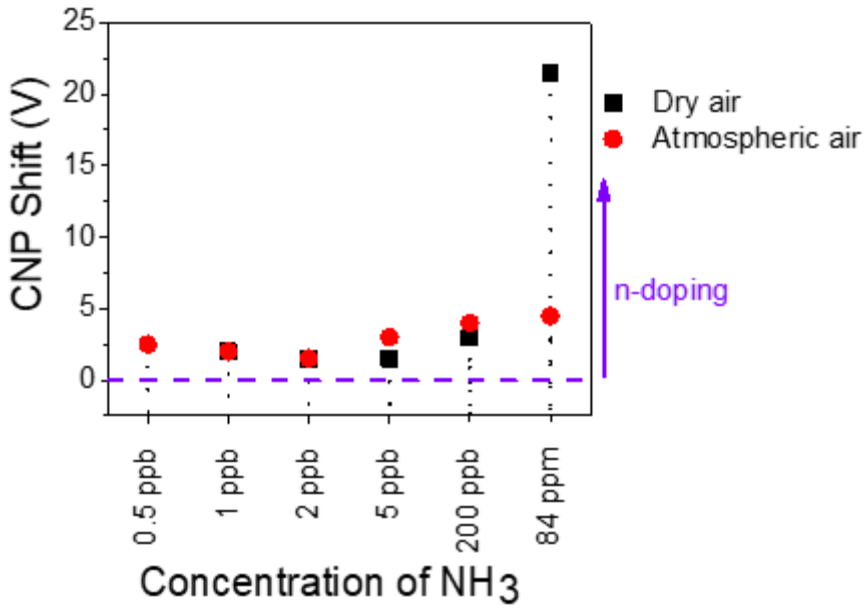

Figure 3.11: Compilation of the results in figures 3.9 and 3.10 and 84 ppm ammonia in atmospheric and dry air. For 84 ppm ammonia in atmospheric air, the concentration of ammonia might be below the expected 84 ppm due to the high pressure in the chamber, consequently, the CNP shift was significantly smaller compared to dry air. All results in atmospheric and dry air were obtained from devices fabricated with standard cleaning and pre-heating except 200 ppb NH_3 in atmospheric air. The relative humidity of atmospheric air in this work was 35% – 69%.

This extreme ammonia sensitivity coupled with the 3 seconds response time (i.e. measurement was done immediately after gas introduction as discussed in the Experimental section) makes the a-CF-GFET sensor the most sensitive and selective room temperature ammonia sensor so far reported. Considering the high relative humidity (35% - 68%) and high pressure (>650 Torr) during measurement in atmospheric air, the a-CF-GFET sensor is suitable for non-invasive medical diagnosis (in clinical gas sensors) as well as environmental monitoring.

Though the a-CF-GFET sensor fabricated without standard cleaning and pre-heating showed higher p-doping in air compared to the sensor fabricated with cleaning and pre-heating, it still

showed extreme sensitivity to ammonia detecting 200ppb ammonia in atmospheric air (Figures 3.10 – 3.11).

3.10. Summary

A selective ammonia gas sensor with good recoverability, room temperature sensitivity of 500 ppt in atmospheric air, and a response time of ~ 3 seconds is presented. The sensor which consists of a 38 nm thick layer of porous oxidized activated carbon on CVD graphene, shows ohmic conductance with carrier mobility as high as 3500 $cm^2/V.S^{-1}$ for an aspect ratio of 6.6. The oxidized activated carbon induces ammonia selectivity while reducing p-doping in atmospheric air. The ammonia sensitivity and selectivity obtained at room temperature suggests the device is suitable for environmental monitoring and non-invasive medical diagnosis of ailments.

References

(1) Rumyantsev, S.; Liu, G.; Shur, M. S.; Potyrailo, R. A.; Balandin, A. A. Selective Gas Sensing with a Single Pristine Graphene Transistor. *Nano Lett.* **2012**, *12* (5), 2294–2298. https://doi.org/10.1021/nl3001293.

(2) Sun, J.; Muruganathan, M.; Mizuta, H. Room Temperature Detection of Individual Molecular Physisorption Using Suspended Bilayer Graphene. *Sci. Adv.* **2016**, *2* (4), e1501518–e1501518. https://doi.org/10.1126/sciadv.1501518.

(3) Schedin, F.; Geim, A. K.; Morozov, S. V.; Hill, E. W.; Blake, P.; Katsnelson, M. I.; Novoselov, K. S. Detection of Individual Gas Molecules Adsorbed on Graphene. *Nat. Mater.* **2007**, *6* (9), 652–655. https://doi.org/10.1038/nmat1967.

(4) Yang, Y.; Brenner, K.; Murali, R. The Influence of Atmosphere on Electrical Transport in

Graphene. *Carbon N. Y.* **2012**, *50* (5), 1727–1733. https://doi.org/10.1016/J.CARBON.2011.12.008.

(5) Hayasaka, T.; Lin, A.; Copa, V. C.; Lopez, L. P.; Loberternos, R. A.; Ballesteros, L. I. M.; Kubota, Y.; Liu, Y.; Salvador, A. A.; Lin, L. An Electronic Nose Using a Single Graphene FET and Machine Learning for Water, Methanol, and Ethanol. *Microsystems Nanoeng.* **2020**, *6* (1), 1–13. https://doi.org/10.1038/s41378-020-0161-3.

(6) Georgakilas, V.; Otyepka, M.; Bourlinos, A. B.; Chandra, V.; Kim, N.; Kemp, K. C.; Hobza, P.; Zboril, R.; Kim, K. S. Functionalization of Graphene: Covalent and Non-Covalent Approaches, Derivatives and Applications. *Chemical Reviews*. American Chemical Society November 14, 2012, pp 6156–6214. https://doi.org/10.1021/cr3000412.

(7) Theodoropoulou, S.; Papadimitriou, D.; Zoumpoulakis, L.; Simitzis, J. Structural and Optical Characterization of Pyrolytic Carbon Derived from Novolac Resin. *Anal. Bioanal. Chem.* **2004**, *379* (5–6), 788–791. https://doi.org/10.1007/s00216-003-2453-5.

(8) Kwon, D.-S.; Nam, H.-G.; Jung, C.-H.; Yang, D.; Kim, S.-T.; Shin, K.; Choi, J.-H. Preparation of Conductive Carbon Films from Novolac Resins by Ion Beam Irradiation and Carbonization. *J. Nanosci. Nanotechnol.* **2018**, *18* (10), 7018–7022. https://doi.org/10.1166/jnn.2018.15474.

(9) Kwon, D.-S.; Choi, H. Y.; Lee, B.-M.; Jeong, Y. G.; Yang, D.; Kim, S.-T.; Choi, J.-H. Electrothermal Application of Novolac-Derived Carbon Micropatterns Prepared by Proton Beam Lithography and Carbonization. *Appl. Surf. Sci.* **2019**, *471*, 328–334. https://doi.org/10.1016/J.APSUSC.2018.11.236.

(10) Gonçalves, M.; Sánchez-García, L.; Oliveira Jardim, E. de; Silvestre-Albero, J.;

Rodríguez-Reinoso, F. Ammonia Removal Using Activated Carbons: Effect of the Surface Chemistry in Dry and Moist Conditions. *Environ. Sci. Technol.* **2011**, *45* (24), 10605–10610. https://doi.org/10.1021/es203093v.

(11) Travlou, N. A.; Ushay, C.; Seredych, M.; Rodríguez-Castellón, E.; Bandosz, T. J. Nitrogen-Doped Activated Carbon-Based Ammonia Sensors: Effect of Specific Surface Functional Groups on Carbon Electronic Properties. *ACS Sensors* **2016**, *1* (5), 591–599. https://doi.org/10.1021/acssensors.6b00093.

(12) Zhou, W.; Yoshino, M.; Kita, H.; Okamoto, K. I. Carbon Molecular Sieve Membranes Derived from Phenolic Resin with a Pendant Sulfonic Acid Group. *Ind. Eng. Chem. Res.* **2001**, *40* (22), 4801–4807. https://doi.org/10.1021/ie010402v.

(13) Mahdyarfar, M.; Mohammadi, T.; Mohajeri, A. Gas Separation Performance of Carbon Materials Produced from Phenolic Resin: Effects of Carbonization Temperature and Ozone Post Treatment. *Xinxing Tan Cailiao/New Carbon Mater.* **2013**, *28* (1), 39–46. https://doi.org/10.1016/S1872-5805(13)60063-3.

(14) Ayyub, O. B.; Behrens, A. M.; Heligman, B. T.; Natoli, M. E.; Ayoub, J. J.; Cunningham, G.; Summar, M.; Kofinas, P. Simple and Inexpensive Quantification of Ammonia in Whole Blood. *Mol. Genet. Metab.* **2015**, *115* (2–3), 95–100. https://doi.org/10.1016/j.ymgme.2015.04.004.

(15) Timmer, B.; Olthuis, W.; Berg, A. van den. Ammonia Sensors and Their Applications—a Review. *Sensors Actuators B Chem.* **2005**, *107* (2), 666–677. https://doi.org/10.1016/J.SNB.2004.11.054.

(16) Narasimhan, L. R.; Goodman, W.; Patel, C. K. Correlation of Breath Ammonia with

Blood Urea Nitrogen and Creatinine during Hemodialysis. *Proc. Natl. Acad. Sci. U. S. A.* **2001**, *98* (8), 4617–4621. https://doi.org/10.1073/pnas.071057598.

(17) Goniszewski, S.; Adabi, M.; Shaforost, O.; Hanham, S. M.; Hao, L.; Klein, N. Correlation of P-Doping in CVD Graphene with Substrate Surface Charges. *Sci. Rep.* **2016**, *6* (1), 1–9. https://doi.org/10.1038/srep22858.

(18) Wu, J.-B.; Lin, M.-L.; Cong, X.; Liu, H.-N.; Tan, P.-H. Raman Spectroscopy of Graphene-Based Materials and Its Applications in Related Devices. *Chem. Soc. Rev.* **2018**, *47* (5), 1822–1873. https://doi.org/10.1039/C6CS00915H.

(19) Some, S.; Xu, Y.; Kim, Y.; Yoon, Y.; Qin, H.; Kulkarni, A.; Kim, T.; Lee, H. Highly Sensitive and Selective Gas Sensor Using Hydrophilic and Hydrophobic Graphenes. *Sci. Rep.* **2013**, *3* (1), 1–8. https://doi.org/10.1038/srep01868.

(20) Muruganathan, M.; Sun, J.; Imamura, T.; Mizuta, H. Electrically Tunable van Der Waals Interaction in Graphene–Molecule Complex. *Nano Lett.* **2015**, *15* (12), 8176–8180. https://doi.org/10.1021/acs.nanolett.5b03653.

(21) Cao, G.; Liu, X.; Liu, W.; Li, Q.; Li, X.; Wang, X. Chemical Environment Dominated Fermi Level Pinning of a Graphene Gas Sensor. *Carbon N. Y.* **2017**, *124*, 57–63. https://doi.org/10.1016/J.CARBON.2017.08.026.

(22) Chen, S.; Cai, W.; Chen, D.; Ren, Y.; Li, X.; Zhu, Y.; Kang, J.; Ruoff, R. S. Adsorption/Desorption and Electrically Controlled Flipping of Ammonia Molecules on Graphene. *New J. Phys.* **2010**, *12* (12), 125011. https://doi.org/10.1088/1367-2630/12/12/125011.

(23) Agbonlahor, O. G.; Muruganathan, M.; Imamura, T.; Mizuta, H. Adsorbed Molecules as Interchangeable Dopants and Scatterers with a Van Der Waals Bonding Memory in Graphene Sensors. *ACS Sensors* **2020**, *5* (7), 2003–2009. https://doi.org/10.1021/acssensors.0c00403.

(24) Salehi-Khojin, A.; Estrada, D.; Lin, K. Y.; Bae, M.-H.; Xiong, F.; Pop, E.; Masel, R. I. Polycrystalline Graphene Ribbons as Chemiresistors. *Adv. Mater.* **2012**, *24* (1), 53–57. https://doi.org/10.1002/adma.201102663.

(25) Huang, P. Y.; Ruiz-Vargas, C. S.; Van Der Zande, A. M.; Whitney, W. S.; Levendorf, M. P.; Kevek, J. W.; Garg, S.; Alden, J. S.; Hustedt, C. J.; Zhu, Y.; et al. Grains and Grain Boundaries in Single-Layer Graphene Atomic Patchwork Quilts. *Nature* **2011**, *469* (7330), 389–392. https://doi.org/10.1038/nature09718.

(26) Yasaei, P.; Kumar, B.; Hantehzadeh, R.; Kayyalha, M.; Baskin, A.; Repnin, N.; Wang, C.; Klie, R. F.; Chen, Y. P.; Král, P.; et al. Chemical Sensing with Switchable Transport Channels in Graphene Grain Boundaries. *Nat. Commun.* **2014**, *5* (1), 1–8. https://doi.org/10.1038/ncomms5911.

Chapter 4

van der Waals Bonding Memory in Graphene Sensors

As described in chapter 2, investigating the stability of the electrically induced van der Waals bonding in graphene sensors is crucial for realizing charge-transfer based molecular identification in gas sensors. In this chapter, the complementary roles of gas adsorption induced doping and scattering on pristine graphene exposed to carbon dioxide are studied and the dependence of doping and scattering on the changes in the graphene-gas molecule vdW bonding which was controlled via tuning voltage modulation is demonstrated. Consequently, the retention of the van der Waals bonding interactions in graphene-molecule complexes is investigated.

4.1. Doping and Scattering in Graphene Conductivity Response

Gas adsorption on the graphene channel in Graphene Field-Effect Transistor (GFET) gas sensors results in van der Waals (vdW) complexes due to the hybridization of the graphene and the adsorbed gas molecular orbitals.[1–4] This hybridization, which can be controlled by an applied electric field, typically alters the density of states[4–7], and as a result, the conductance (or resistance),[8–16] charge neutrality point (CNP)[4,17–20] and even the 1/f noise characteristics[21,22] of the GFET sensor. Monitoring the conductivity (or resistance) response is one of the most commonly used methods in GFET sensors. As expected from the Drude's model ($\sigma = ne\mu$), a change in conductivity, σ, is expected to depend on the carrier concentration (n) and the mobility (μ) of the carriers in graphene, where e is the electronic charge. Nevertheless, such gas adsorption induced changes in conductivity are often associated with carrier depletion due to electron-hole

recombination in the channel[12,23] or carrier accumulation[9,24], while the effect of the gas adsorption induced changes on carrier mobility (or scattering) is often ignored, despite the fact that higher gas adsorption induced doping (*ne*) does not always result in the expected higher conductivity response (σ).[25] Additionally, though tuning voltage (V_t) modulation has been known to alter the vdW bonding, consequently the doping characteristics of adsorbed gases in GFET sensors,[4,20,23,26] a detailed understanding of the corresponding effect of such tuning voltage modulation on the gas adsorption induced scattering is still lacking. Nevertheless, due to its 2D nature, carrier transport in graphene is very sensitive to scattering induced by the substrates,[27–29] as well as defects and impurities in the graphene channel.[7,8,18,30] Indeed, gas adsorption has been shown to induce changes in mobility due to carrier scattering,[10,20,25] with the change in mobility due to adsorption on defective and pristine sites showing different trends.[8,26]

4.2. Device Fabrication and Experimental Methodology

The pristine graphene field-effect transistor sensor was fabricated via mechanical exfoliation of monolayer graphene from highly ordered pyrolytic graphite on an n-doped silicon wafer with a 285-nm thick silicon dioxide layer. First electron beam lithographic (EBL) patterning with polymethyl methacrylate/methylmethacrylate (PMMA/MMA) resist mask and subsequent metal evaporation was done to define the address pattern. Thereafter, graphene was exfoliated from pyrolytic graphite using scotch tape. A PMMA/MMA resist was used as a positive mask to define electrode patterns on graphene using EBL. Thereafter, the exposed graphene was etched with oxygen plasma, and contact electrodes (Au/Cr) were deposited and lift-off done in acetone. Finally, the graphene nanoribbons were defined via EBL, and oxygen plasma etching. Finally, the post-lithographic residues were removed by annealing in an Ar/H_2 environment at 350 ^oC for 3h.

Gas Sensing Measurements: The transfer characteristic of the device in vacuum was obtained, then the conductivity response, I_d vs Time at constant V_t, of the sensor was monitored for about 56 minutes while 100% CO_2 gas was simultaneously fed into the chamber. During this period, the conductivity response was interrupted (for ~ 30 seconds) to obtain the transfer characteristics at intervals of 12 minutes, 27 minutes (chamber full of CO_2 gas), 33 minutes, 37 minutes, 47 minutes, and 56 minutes using a semiconductor analyzer. Thereafter, the tuning experiment was stopped completely and only the transfer characteristic was monitored at intervals of 30 minutes until 206 minutes was reached. After each experiment, the device was recovered by annealing in vacuum at 150^{o}C for 3 h resulting in slightly p-doped graphene. All measurements were performed at room temperature. For all tuning voltages, the same experimental procedure described above was used.

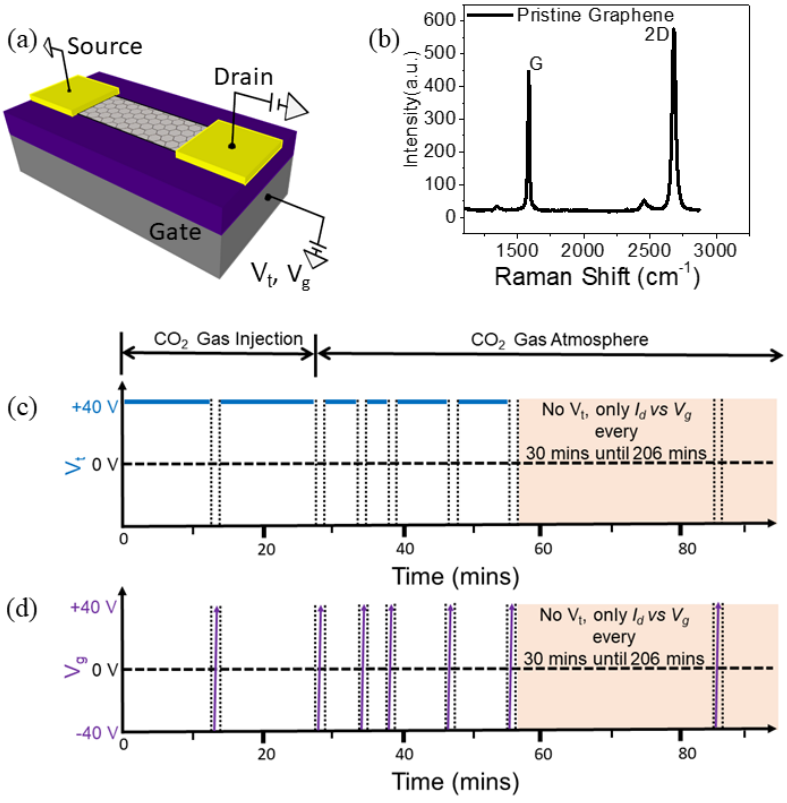

Figure 4.1: (a) Schematic diagram of the GFET sensor. (b) Raman spectra of the graphene. (c) Experimental schematic of the conductivity measurement i.e. V_t experiment for V_t = 40 V. Blue lines = applied V_t. (d) Experimental

schematic for the vdW doping characteristics measurement: purple lines = transfer characteristics (Id vs Vg) measurement; orange region = no V_t applied; white region = V_t applied; the period during which the transfer characteristics were measured is enclosed in dashed lines.

The conductivity was obtained from the drain current (I_d), source-drain bias voltage (V_{ds}) = 1 mV, device length (L), and width (W) using the formula:

$$\sigma = \frac{I_d}{V_{ds}} . \frac{L}{W} \qquad (4.1)$$

The vdW bonding induced doping concentration (n_d) due to gas adsorption hereafter referred to as vdW doping was extracted from the CNP shift with respect to vacuum (ΔV_{CNP}) in the transfer characteristics using the formula:

$$n_d = \frac{C_g}{e} . \Delta V_{CNP} \qquad (4.2)$$

where C_g is the gate capacitance, $\varepsilon_0\varepsilon_r/t_{ox}$, $\boldsymbol{\varepsilon}_o$ and $\boldsymbol{\varepsilon}_r$ permittivity of vacuum and relative permittivity of SiO_2, t_{ox} is the SiO_2 thickness. The field-effect mobility (μ) was obtained from the equation:

$$\mu = g_m\left(\frac{L}{WV_{ds}C_g}\right) \qquad (4.3)$$

where g_m is the transconductance, and the change in field-effect mobility ($\Delta\mu$) was obtained from $\Delta\mu = \mu_{(max)vac} - \mu_{(max)gas}$, where $\mu_{(max)vac}$ is the maximum field-effect mobility in vacuum and $\mu_{(max)gas}$ is the maximum field-effect mobility in the gas environment. For all transfer characteristics measurements, the gate voltage was swept from -40 V to +40 V.

The schematics and Raman spectra of the 2 µm x 1 µm device obtained from mechanically exfoliated graphene on a 285 nm SiO_2 substrate are shown in Figures 4.1a and 4.1b respectively. The experimental procedure is shown schematically in Figures 4.1c and 4.1d.

4.3. Electrically Tunable Gas Adsorption Induced Doping and Scattering

The variation of the conductivity response of the graphene sensor with time upon carbon dioxide adsorption was obtained at each tuning voltage as shown in Figures 4.2 a-e for V_t = 40 V, 36 V, 0 V, -20 V, -40 V. The transfer characteristics measured immediately after each tuning experiment are shown in Figure 4.3. As shown in Figure 4.2 a-e the as-fabricated device was p-doped after vacuum annealing. This is typical for graphene on SiO_2 and is often attributed to the adsorption of organic residues from the lithographic process.[23] In the following discussions, analysis of results obtained in-between the V_t experiments (IV_t) i.e. Figures 4.2 and 4.3 and the white regions in Figures 4.4 a-b are referred to using the prefix IV_t while those taken after the V_t experiments (AV_t) were stopped i.e. the orange region in Figure 4.4 a-b are referred to with the prefix AV_t.

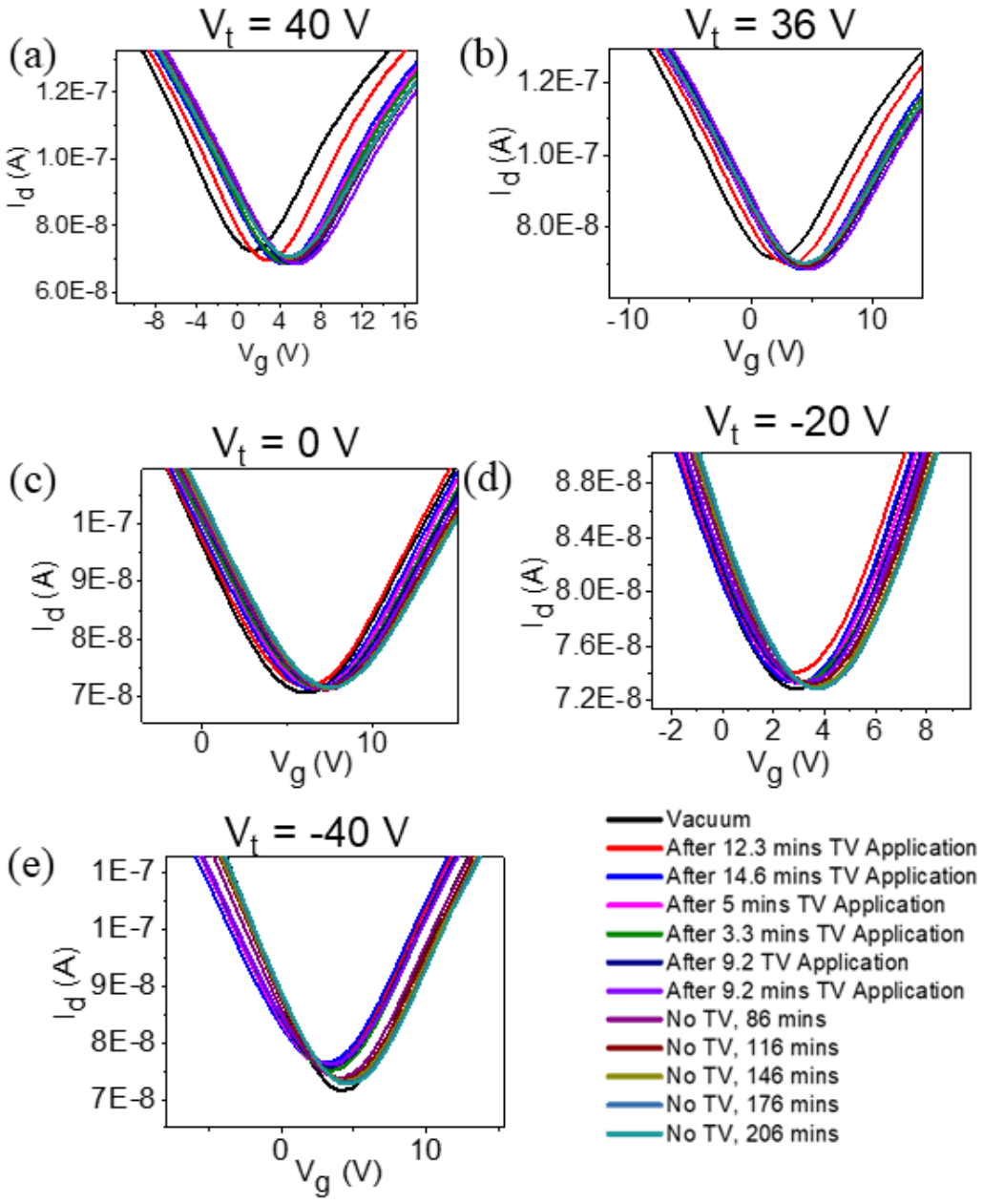

Figure 4.2: Transfer characteristics plot for carbon dioxide adsorption on pristine graphene. (a) 40 V tuning voltage. (b) 36 V tuning voltage. (c) 0 V tuning voltage. (d) -20 V tuning voltage. (e) -40 V tuning voltage.

As shown in Figures 4.4a and 4.2, the amount of IV_t- and AV_t- vdW hole doping induced by the adsorbed CO_2 molecules decreased in the order: 40 V > 36 V > 0 V > -20 V > -40 V. This is consistent with previous reports in which p-doping decreased as the tuning voltage decreased due

to carbon dioxide acting as an acceptor at positive V_t and $V_t = 0$ while showing weak n-doping (donor properties) at negative tuning voltages,[4] which decreased with time and gradually became p-doping. This vdW doping represents the residual vdW bonding-induced doping in the graphene-molecule complex due to V_t modification of the graphene-molecule vdW bonding interactions. vdW doping is often used to probe the effect of V_t on the graphene-molecule vdW complex.[4,20] Interestingly, even after the V_t tuning experiment was completely stopped (after 56 minutes) and the transfer characteristics measured periodically (i.e. in intervals of 30 mins), the different V_t-induced graphene-CO_2 complexes still exhibited vdW doping characteristics unique to each V_t for up to 2 h (see Figure 4.4a, orange region), suggesting that the V_t-tuned graphene-molecule vdW complexes are not completely lost after the V_t is turned off or after a gate voltage sweep. In short, the V_t-induced graphene-molecule complexes 'remember' their bonding states i.e. they have a 'vdW bonding memory'. The observation of 'vdW bonding memory' is particularly useful in developing a method for the molecular identification of gas molecules based on their tunable charge-transfer characteristics[4,26] and shows that the characteristics of the vdW complexes can be studied even after turning off the V_t. It is important to note that though the transfer characteristics were obtained by sweeping the gate voltage from -40 V to +40 V, the states induced by the negative tuning voltages (-40 V and -20 V) and the calculated doping concentration, will only be marginally altered (by the change in voltage polarity during this gate voltage sweep) as previously demonstrated.[4] This was further confirmed by the observation of a tuning voltage-dependent 'vdW bonding memory' for the graphene-CO_2 complexes, which lasted for several minutes, even for the negative tuning voltages, as discussed above (Figure 4.4a, orange region).

Next, the properties of the graphene-CO_2 vdW complex based on the vdW doping and mobility changes induced in the vdW complexes is investigated and the effects of these V_t-induced

interactions on the observed conductivity response discussed. For the 0 V, -20 V, and -40 V V_t vdW complexes, the device remained p-doped (in vacuum, during V_t tuning, and after gas injection). Hence, it is expected that the conductivity will increase progressively with time as the hole concentration increased, while it should decrease for the states where n-doping was observed. For the 0 V tuned complex, the hole concentration increased with time as evident in the increase in the vdW doping (Figure 4.4a). Hence, the conductivity progressively increased with time due to carrier accumulation and minimal gas adsorption induced scattering, suggesting that the conductivity response is doping dominated. However, for the -40 V tuning experiment, during the 12.3- and 14.6-minute tuning experiments, a decrease in conductivity was observed as expected from electron-hole recombination due to n-doping in graphene, as evident in the vdW doping in Figure 4.4a. Thereafter, the overall conductivity increased from one tuning experiment to the next due to increasing p-doping (as evident in the vdW doping) but remained relatively stable over time during individual tuning experiments due to the high gas adsorption induced scattering in the vdW complex at negative V_t. This stable conductivity value observed was in contrast to the expected rising conductivity with time when vdW p-doping increased in doping dominated transport (as seen for 0 V, Figure 4.3c) and is attributed to gas adsorption induced scattering.

Similar results to the -40 V tuning experiments were obtained for the -20 V tuning experiment. For the +40 V and +36 V tuning experiments, though the device remained p-doped in vacuum and after the V_t experiments, it was n-doped during the V_t experiment as the applied V_t moved the Fermi level of graphene into the conduction band. As seen in the vdW doping, hole concentration increased with time after V_t-application suggesting that the applied V_t increased the acceptor properties of the adsorbed CO_2 molecules on graphene. Hence, the conductivity decreased with time as shown in

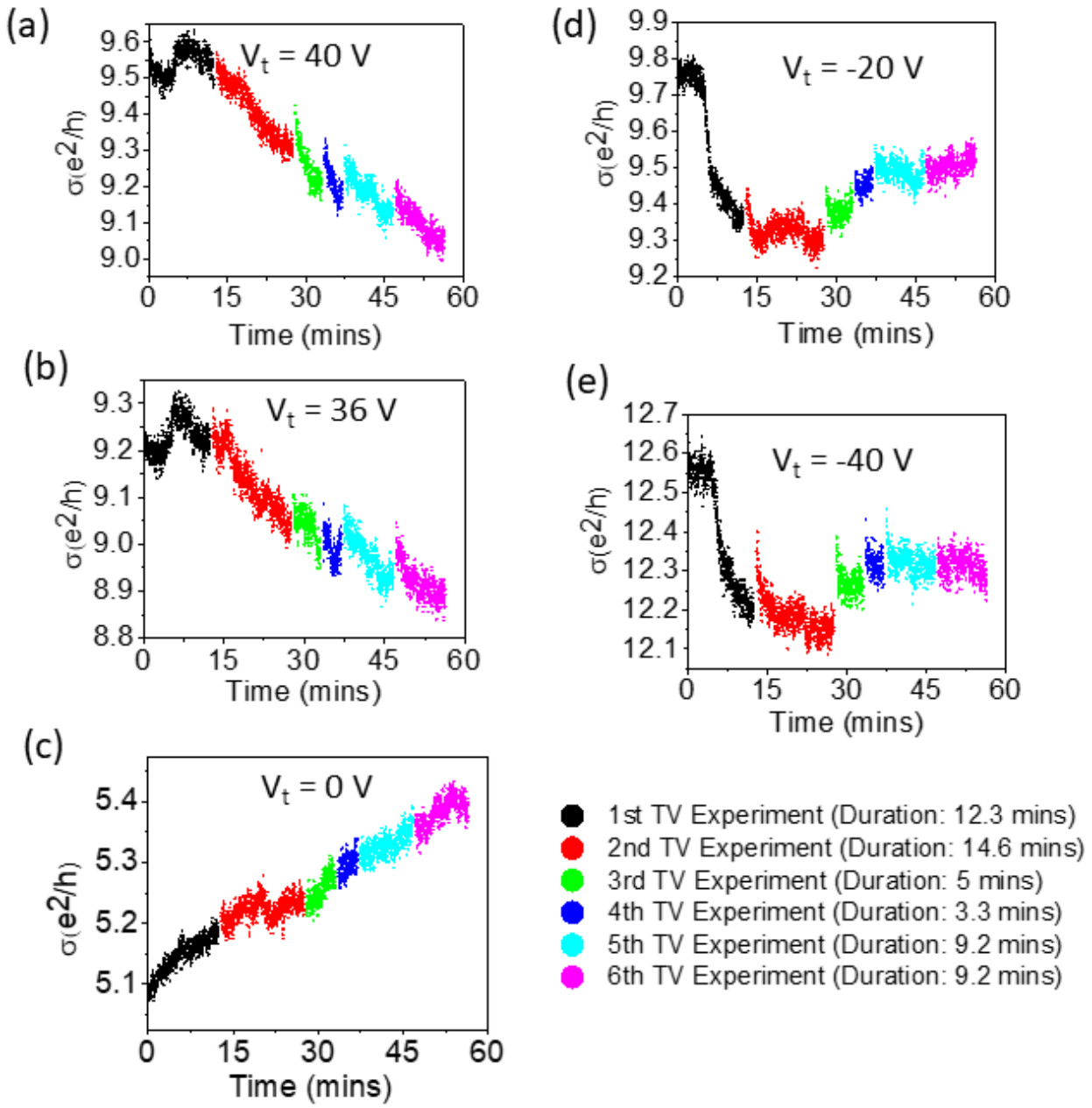

Figure 4.3: The conductivity (σ) vs time for CO_2 adsorption on pristine graphene for various V_t. (a) V_t = 40 V (b) V_t = 36 V (c) V_t = 0 V (a) V_t = -20 V (e) V_t = -40 V.

Figures 4.3a,b due to electron-hole recombination and gas adsorption induced scattering. Since both of these effects reduce the conductivity, it does not show saturation unlike in V_t = -40 V and -20 V vdW complexes (Figures 4.4d,e).

The effect of gas adsorption induced scattering on the observed AV_t-$\Delta\mu$ was in the order: 40 V > -40 V > 36 V > 0 V ~ -20 V suggesting that gas adsorption induced scattering increases with V_t and is higher for $+V_t$. However, such a clear trend was not observed for the IV_t-$\Delta\mu$. Notably, the IV_t-$\Delta\mu$ for 36 V was unexpectedly low suggesting that factors besides gas adsorption induced scattering are also influencing the observed IV_t-$\Delta\mu$. For V_t-experiments in graphene on SiO_2 devices, charge traps in the SiO_2 layer typically result in trapping/de-trapping processes with a timescale of sub-nanoseconds to microseconds. Additionally, retention of charges for several minutes in deep traps after turning off the V_t also occurs.[31] This charge retention by the traps after V_t experiments typically influence the observed field-effect mobility[32,33] by altering the effective gate voltage experienced when a transfer characteristic measurement is done immediately after (as in our experiment), such that the $+V_t$ and $-V_t$ tuned complexes will be affected differently depending on whether the traps are acceptor-type or donor-type. The irregularity in IV_t-$\Delta\mu$ may be attributed to this effect. Hence AV_t-$\Delta\mu$ (i.e. the "NO V_t", the orange region in Figure 4.4b) was used to ascertain the effect of gas adsorption induced scattering on the mobility since this region did not involve V_t experiments. Evidence of the synergistic effect of the V_t experiments and the traps is seen in the fact that unlike the IV_t-$\Delta\mu$, the AV_t-$\Delta\mu$ is consistent with the expected gas adsorption induced scattering based on electron difference analysis as discussed below. It is important to note that these deep traps marginally affect the Dirac point of graphene as the tunneling barrier is large,[31,33] hence the traps will have a negligible effect on the observed IV_t-n_d and AV_t-n_d. Notably, though the 0 V tuned complex has a higher hole concentration than the -40 V complex (Figure 4.4a), it exhibits lower gas adsorption induced scattering than the -40 V complex (Figure 4,4b,c) demonstrating that higher gas adsorption induced-doping does not always translate into higher gas adsorption induced scattering.

The competing role between doping and scattering is summarized in Figure 4.4c, in which the rate of change in conductivity per second, (Initial Conductivity (σ_i) – Final Conductivity (σ_f))/Time, which in this work is termed the scattering-doping index ($\Delta\sigma$) for each tuning experiment was plotted against time starting from the second tuning experiment (14.6 minutes), at which point the effects of gas adsorption induced scattering became more obvious. To calculate $\Delta\sigma$, the initial conductivity was taken as the mean of the first ten conductivity values, while the final conductivity value was taken as the mean of the last ten conductivity values, so that for $\Delta\sigma$ values > 0

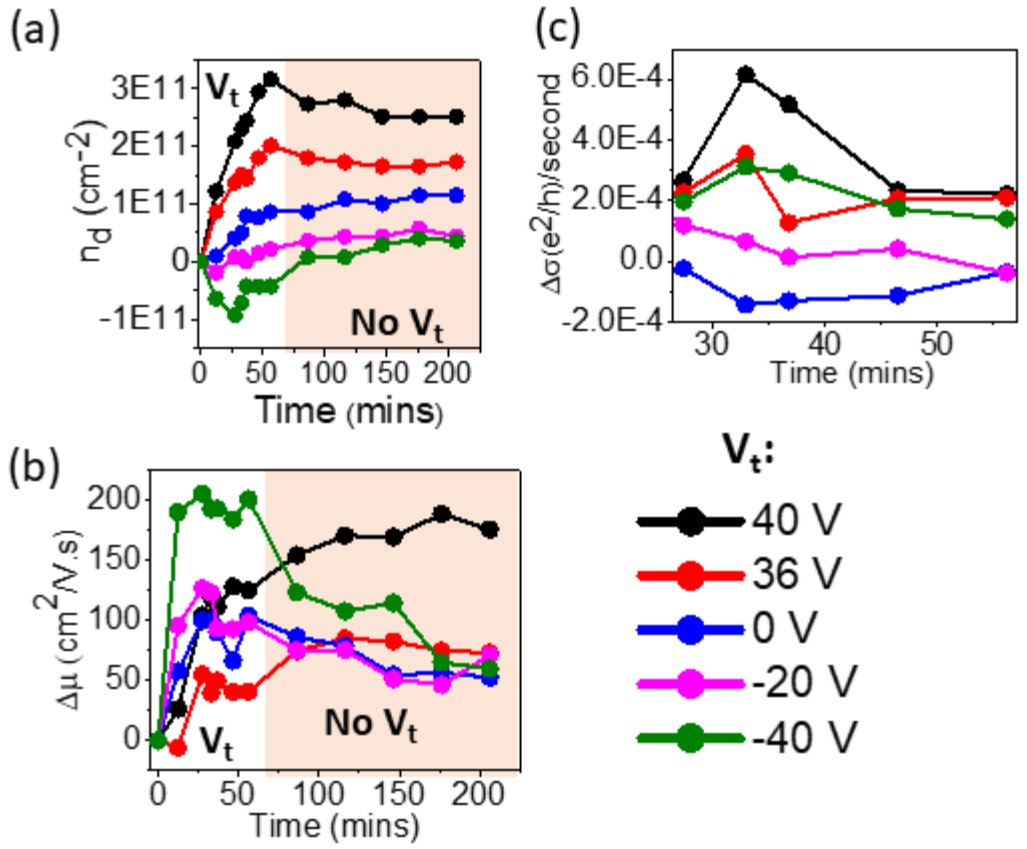

Figure 4.4: Doping concentration and mobility response vs time for CO_2 adsorption on graphene. (a) vdW doping concentration vs time for V_t = 40 V, 36 V, 0 V, -20 V, -40 V: white region = tuning voltage applied region i.e. the region with the conductivity shown in Figures 4.3a-e, orange region = no tuning voltage applied (vdW bonding

memory region). (b) Change in hole mobility vs time of pristine graphene exposed to CO_2. (e) $\Delta\sigma$, the scattering-doping index, $\left(\frac{Initial\ Conductivity(\sigma_i) - Final\ Conductivity(\sigma_f)}{Tuning\ Time}\right)$ vs time for V_t = 40 V, 36 V, 0 V, -20 V, -40 V i.e. a summary of Figures 4.3a-e. For $\Delta\sigma > 0$, scattering dominates the transport, while for $\Delta\sigma<0$ doping dominates the transport.

scattering dominates the transport, while for $\Delta\sigma < 0$ doping dominates the transport. This interpretation of $\Delta\sigma$ is only applicable to the $-V_t$ and $V_t = 0$ states since for the $+V_t$, both doping and scattering resulted in a decrease in the conductivity. To explain the observed doping and scattering trends discussed above, the effect of the tuning voltage on the graphene-CO_2 molecule vdW bonding was examined via simulations.

4.4. DFT Simulations on Graphene-CO_2 vdW Bonding

First-principles calculations were performed using the density functional theory (DFT) code[34] based on a linear combination of numerical atomic orbitals and PseudoDojo pseudopotentials with medium basis set. Grimme DFT-D3 van der Waals corrections with three-body energy term were included to account for the long-range van der Waals (vdW) interaction more accurately.[35] In these simulations, the revised Perdew-Burke-Ernzerhof (revPBE) functional was used[36] to obtain the best results for the interlayer distance and charge-transfer,[35] with a 10 Å vacuum distance maintained in the non- periodic direction to avoid any spurious interactions with the adjacent supercell. The dimensions of the simulated graphene-CO_2 supercell were 25 Å × 14.766 Å × 17.0503 Å and a single molecule was adsorbed in the central region of the graphene. The k-points of 1 × 2 × 2 were used for the Brillouin zone integration. Initially, the configurations of the graphene – CO_2 system were optimized under different electric fields by fully relaxing the atomic structures until the remaining residual force was smaller than 0.01 eV/Å. This optimized structure was supplemented with three-body energy term $E^{(3)}$ in DFT-D3 correction for a more

accurate evaluation of the vdW forces. Figure 4.5a shows the geometrically optimized graphene-CO_2 atomic structure under zero electric field. As the graphene was adsorbed on the SiO_2 surface in the experiment, the graphene atoms during geometrical optimization was fixed and the CO_2 molecule was allowed to move. The electric field strength above the graphene surface was calculated for the corresponding experimental tuning voltage by finite element simulation resulting in an electric field strength of 0.15 and -0.15 V/Å for the applied tuning voltages of 40 and -40 V respectively. The binding energy of the CO_2 molecule on graphene was calculated for the different electric fields and was defined as $E_{Bind} = E_{(gra\text{-}mol)} - (E_{gra}+E_{mol})$, where $E_{gra\text{-}mol}$ is the total energy of the graphene - molecule system and E_{gra} and E_{mol} are the total energies of the graphene and the isolated CO_2 molecule, respectively. The calculated binding energies were 290, 291, and 297 meV for the electric fields of 0.15, 0, and -0.15 V/Å, respectively. These binding energies indicate that: i) molecules are physisorbed onto the graphene surface, and ii) as binding energies are much higher than thermal energies, the vdW bonding states are not completely lost even after the V_t was turned off in the experiment, hence 'vdW bonding memory' was observed as discussed above. By nature, vdW interactions are weak and reversible. This is evident in the vdW bonding memory of the -40 V complex after 146 minutes as AV_t-n_d became similar to the -20 V AV_t-n_d. A similar trend was observed after 146 minutes in the AV_t-$\Delta\mu$ (Figure 4.4c). This suggests that the -40 V has the least favorable interaction of the V_t-complexes.

Table 1. Electric field modulated charge-transfer and molecular re-orientation of CO_2 molecule adsorbed on graphene

		Distance from Graphene Surface				
Electric field [V/m]	Tuning voltage [V]	Carbon [Å]	Oxygen 1 [Å]	Oxygen 2 [Å]	Angle [$\boldsymbol{\theta}$]	Excess charge on CO_2 (e)
- 0.30	-80 V	3.0257	2.9935	3.0245	180.46	0.005
- 0.15	-40 V	3.0207	3.0207	3.0264	179.72	0.001
0.00	0 V	3.0517	3.0598	3.0652	178.95	-0.003
0.15	40 V	3.0126	3.0311	3.0321	178.16	-0.010
0.30	80 V	3.0121	3.0371	3.0418	177.35	-0.015

Table 1 shows the electric fields, the corresponding tuning voltages, the carbon of CO_2 and the oxygen of CO_2 adsorption distances from graphene, O=C=O bond angle, and the excess charge on the CO_2 molecule (i.e. charge-transfer) after interaction with graphene. CO_2 acted as a donor for negative electric fields and an acceptor for zero- and positive electric fields, which are consistent with the experimental results for the different tuning voltages (Figure 4.4a). In the case of the negative electric field, the CO_2 molecule moved closer to the graphene surface compared to the zero electric field, but farther away from the graphene surface when compared to the positive electric field. Moreover, as the negative electric field strength increased, the oxygen atoms of the CO_2 molecule moved closer to the graphene surface, while an increase in the positive electric field resulted in the oxygen atoms of the CO_2 molecule moving farther away from the graphene surface compared to the carbon of the CO_2 molecule.

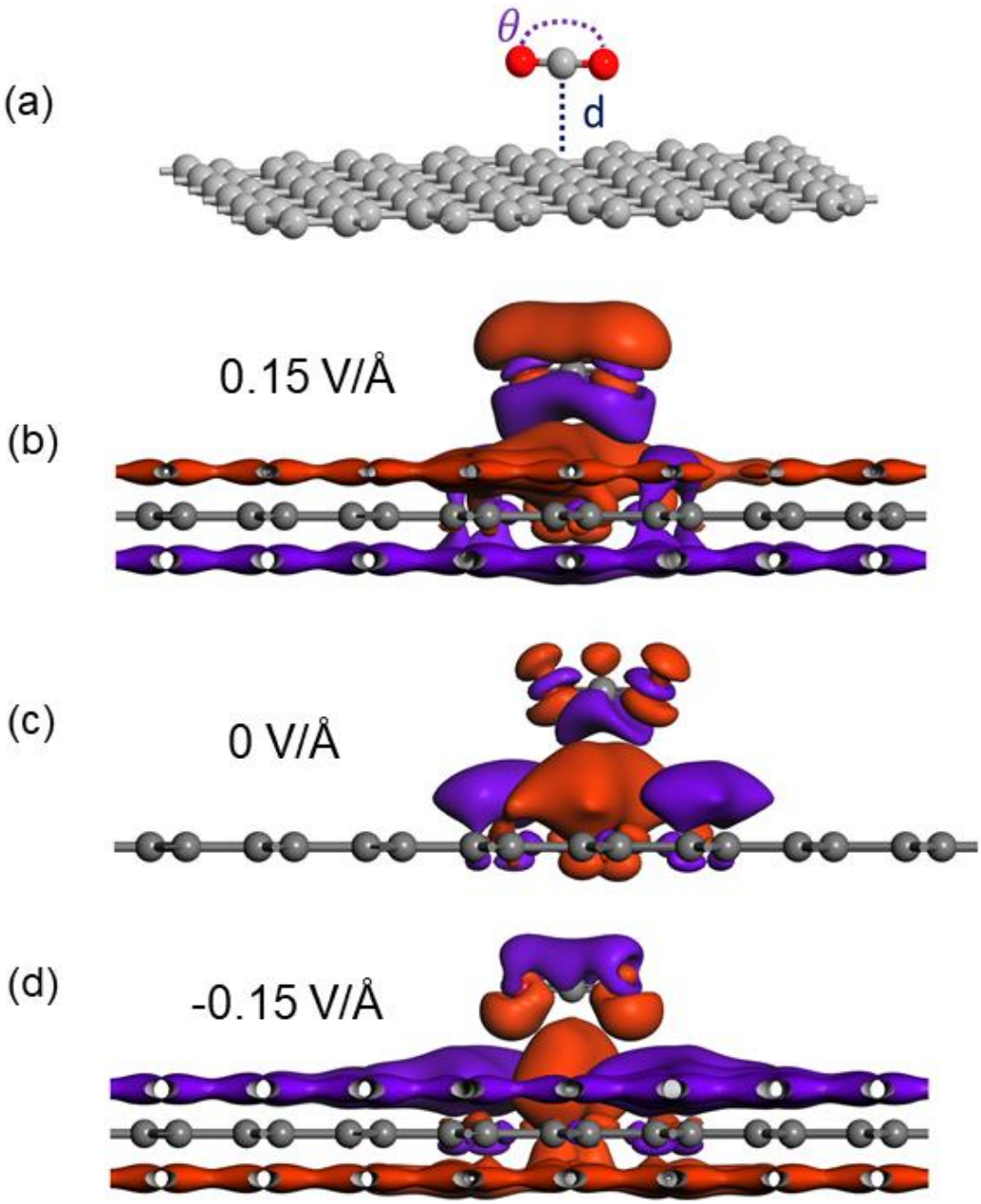

Figure 4.5: (a) The geometrically optimized graphene-CO_2 atomic structure under zero electric field. Visualization of the electron difference density at an iso-value of 8×10^{-4} electron/Å^3 for a CO_2 molecule adsorbed on the graphene surface at different tuning voltages of (b) 0.15 V/Å (i.e. V_t = 40 V), (c) 0.0 V/Å (i.e. V_t = 0 V), (d) -0.15 V/Å (i.e. V_t = -40 V). Red regions = electron-rich regions, purple regions = electron-deficient regions.

These distances are consistent with an increase in the O=C=O bond angle from the highest positive electric field strength to the negative electric field strength as shown in Table 1. Since, the closer the scattering centers in the CO_2 molecule (i.e. the carbon and oxygen atoms of CO_2) move toward the graphene sheet, the higher the scattering potential experienced on the graphene surface and the stronger the scattering becomes, these results indicate that scattering due to the CO_2 molecule will be minimum for zero electric field as CO_2 molecule is far from the graphene surface and maximum for the positive electric field as CO_2 molecule moves closer to graphene. For the negative electric field, scattering will be lower than the positive electric field, but higher than the zero electric field as the CO_2 molecule is situated in between the positive and negative electric field positions. These effects were visualized using the electron difference density plot shown in Figures 4.5b-d for V_t = 40 V (0.15 V/Å), 0 V (0 V/Å), and -40 V (-0.15 V/Å) respectively. The electron difference density of graphene - CO_2 vdW complex is defined as $\rho_{Ad} = \rho_{CO_2+Gra} - \rho_{CO_2} - \rho_{Gra}$, where ρ_{CO_2+Gra}, ρ_{Gra}, and ρ_{CO_2} are the electron densities of the graphene - CO_2 vdW complex, the pristine graphene, and an isolated CO_2 molecule respectively for the given electric fields. The red regions in the plot are the electron-rich regions, while the purple regions are the electron-deficient regions. At electric fields of 0.15 V/Å and -0.15 V/Å, the electron difference density is more delocalized compared to the 0 V/Å tuning voltage, furthermore, for 0.15 V/Å, the electron difference density around the CO_2 is much closer to the graphene surface compared to the -0.15 V/Å, suggesting that scattering will be in the order: 0.15 V/Å > -0.15 V/Å > 0 V/Å i.e. 40 V > -40 V > 0 V which agrees with the experimental results for AV_t-$\Delta\mu$ as discussed earlier.

Furthermore, the number of adsorbed CO_2 molecules on graphene (Figure 4.6) at three tuning voltages (40 V, 0 V, and -40 V) is calculated using the formula:

$$N = \frac{n_d . 2 \times 10^{-8}}{Q}$$

where n_d is the vdW doping concentration from Figure 4.4a, Q is the estimated charge-transfer for one adsorbed molecule from DFT calculations (Table 1), and 2×10^{-8} is a conversion factor from cm^{-2} to the actual device dimension (L = 2 μm, W = 1 μm).

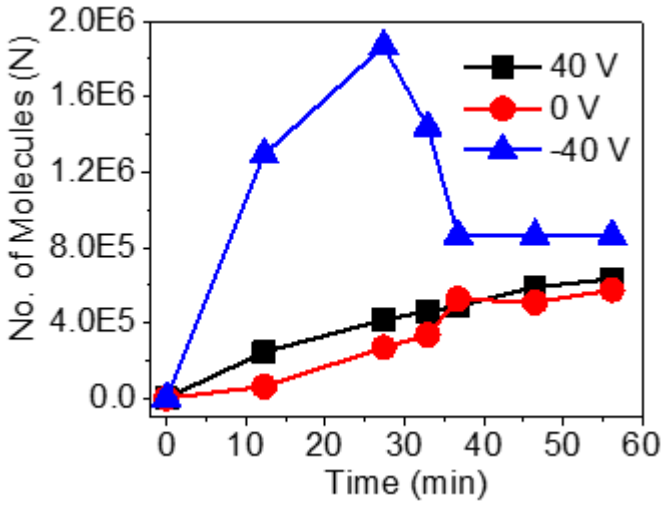

Figure 4.6: Estimated number of adsorbed CO_2 molecules on pristine graphene.

In this equation, it is arbitrarily assumed that at each tuning voltage, each adsorbed molecule has the same charge-transfer and for all tuning voltage experiments, the device has the same number of adsorption sites. The result shows that the number of adsorbed molecules per second (188 molecules for 40 V, 171 molecules for 0 V, and 256 molecules for -40 V) are of similar order for the three tuning voltages, confirming that the graphene-CO_2 vdW bonding as described above, not the difference in the number of adsorbed molecules, is the major factor responsible for the scattering and doping trends observed in the experimental results.

4.5. Summary

It is shown that adsorption induced scattering in the graphene channel does not always increase with the doping concentration or the number of adsorbed molecules, but is controlled by the graphene-molecule vdW bonding, which is electrically tunable. Using an applied tuning voltage to vary the nature of the graphene-gas vdW bonding, the conductivity measurements, changes in field-effect mobility, and DFT simulations show that doping dominated transport is observed at $V_t = 0$ V, while scattering increased when a tuning voltage was applied i.e. at $V_t \neq 0$ V. The gas adsorption induced scattering was also evident in the decrease in field-effect mobility with time. Using DFT simulations for CO_2 adsorption on pristine graphene, the observed scattering trend was shown to depend on the nature of the graphene-CO_2 vdW bonding, which was evident in the smaller graphene sheet distance from the scattering centers in the CO_2 molecule (i.e. the carbon and oxygen atoms of CO_2) upon V_t application, as well as the V_t-dependent charge re-distribution and delocalization in the graphene-gas molecule vdW complex as shown in the electron difference density plots.

Consequently, our results show that tuning voltage application generally results in stronger scattering due to the increased interaction between the adsorbed gas molecules and graphene, such that charge localization and higher graphene-gas adsorption distance reduces gas adsorption induced scattering. Furthermore, after turning off the V_t, the tuning voltage induced graphene-CO_2 vdW complexes 'remembered' their respective V_t-induced vdW bonding states (i.e. possessed a 'vdW bonding memory') by maintaining distinct V_t-dependent doping levels for several minutes. This effect was attributed to the high binding energies associated with these bonding states. This

'vdW bonding memory' is particularly useful in developing a method for the identification of gas molecules based on their tunable charge-transfer.[4,26]

References

(1) Leenaerts, O.; Partoens, B.; Peeters, F. M. Adsorption of H_2O, NH_3, CO, NO_2, and NO on Graphene: A First-Principles Study. *Phys. Rev. B* **2008**, *77* (12), 125416. https://doi.org/10.1103/PhysRevB.77.125416.

(2) Kong, L.; Enders, A.; Rahman, T. S.; Dowben, P. A. Molecular Adsorption on Graphene. *J. Phys. Condens. Matter* **2014**, *26* (44), 443001. https://doi.org/10.1088/0953-8984/26/44/443001.

(3) Qin, H.; Feng, C.; Luan, X.; Yang, D. First-Principles Investigation of Adsorption Behaviors of Small Molecules on Penta-Graphene. *Nanoscale Res. Lett.* **2018**, *13* (1), 264. https://doi.org/10.1186/s11671-018-2687-y.

(4) Muruganathan, M.; Sun, J.; Imamura, T.; Mizuta, H. Electrically Tunable van Der Waals Interaction in Graphene–Molecule Complex. *Nano Lett.* **2015**, *15* (12), 8176–8180. https://doi.org/10.1021/acs.nanolett.5b03653.

(5) Zhang, Z.; Zhang, X.; Luo, W.; Yang, H.; He, Y.; Liu, Y.; Zhang, X.; Peng, G. Study on Adsorption and Desorption of Ammonia on Graphene. *Nanoscale Res. Lett.* **2015**, *10* (1), 359. https://doi.org/10.1186/s11671-015-1060-7.

(6) Junkermeier, C. E.; Solenov, D.; Reinecke, T. L. Adsorption of NH_2 on Graphene in the Presence of Defects and Adsorbates. *J. Phys. Chem. C* **2013**, *117* (6), 2793–2798. https://doi.org/10.1021/jp309419x.

(7) Kumar, S.; Malhotra, M.; Sharma, H. Adsorption of Gas Molecules on Ultra-Thin Pristine and Doped Graphene Nanoribbons. *Mater. Res. Express* **2018**, *5* (10), 105007. https://doi.org/10.1088/2053-1591/aadaa8.

(8) Blechta, V.; Drogowska, K. A.; Vales, V.; Kalbac, M. Adsorption Site-Dependent Mobility Behavior in Graphene Exposed to Gas Oxygen. *J. Phys. Chem. C* **2018**, *122* (37), 21493–21499. https://doi.org/10.1021/acs.jpcc.8b06906.

(9) Jaaniso, R.; Kahro, T.; Kozlova, J.; Aarik, J.; Aarik, L.; Alles, H.; Floren, A.; Gerst, A.; Kasikov, A.; Niilisk, A.; et al. Temperature Induced Inversion of Oxygen Response in CVD Graphene on SiO2. *Sensors Actuators B Chem.* **2014**, *190*, 1006–1013. https://doi.org/10.1016/J.SNB.2013.09.068.

(10) Hayasaka, T.; Kubota, Y.; Liu, Y.; Lin, L. The Influences of Temperature, Humidity, and O2 on Electrical Properties of Graphene FETs. *Sensors Actuators B Chem.* **2019**, *285*, 116–122. https://doi.org/10.1016/J.SNB.2019.01.037.

(11) Mortazavi Zanjani, S. M.; Sadeghi, M. M.; Holt, M.; Chowdhury, S. F.; Tao, L.; Akinwande, D. Enhanced Sensitivity of Graphene Ammonia Gas Sensors Using Molecular Doping. *Appl. Phys. Lett.* **2016**, *108* (3), 033106. https://doi.org/10.1063/1.4940128.

(12) Chen, G.; Paronyan, T. M.; Harutyunyan, A. R. Sub-Ppt Gas Detection with Pristine Graphene. *Appl. Phys. Lett.* **2012**, *101* (5), 053119. https://doi.org/10.1063/1.4742327.

(13) Kim, Y. H.; Kim, S. J.; Kim, Y.-J.; Shim, Y.-S.; Kim, S. Y.; Hong, B. H.; Jang, H. W. Self-Activated Transparent All-Graphene Gas Sensor with Endurance to Humidity and Mechanical Bending. *ACS Nano* **2015**, *9* (10), 10453–10460.

https://doi.org/10.1021/acsnano.5b04680.

(14) Kim, Y.; Choi, Y. S.; Park, S. Y.; Kim, T.; Hong, S. P.; Lee, T. H.; Moon, C. W.; Lee, J. H.; Lee, D.; Hong, B. H.; et al. Au Decoration of a Graphene Microchannel for Self-Activated Chemoresistive Flexible Gas Sensors with Substantially Enhanced Response to Hydrogen. *Nanoscale* **2019**, *11* (6), 2966–2973. https://doi.org/10.1039/c8nr09076a.

(15) Tang, X.; Mager, N.; Vanhorenbeke, B.; Hermans, S.; Raskin, J. P. Defect-Free Functionalized Graphene Sensor for Formaldehyde Detection. *Nanotechnology* **2017**, *28* (5). https://doi.org/10.1088/1361-6528/28/5/055501.

(16) Yang, C. S.; Mahmood, A.; Kim, B.; Shin, K.; Jeon, D. H.; Han, J. K.; Bu, S. D.; Park, S.; Choi, W.; Doudin, B.; et al. Enhancing Gas Sensing Properties of Graphene by Using a Nanoporous Substrate. *2D Mater.* **2016**, *3* (1). https://doi.org/10.1088/2053-1583/3/1/011007.

(17) Sun, J.; Muruganathan, M.; Mizuta, H. Room Temperature Detection of Individual Molecular Physisorption Using Suspended Bilayer Graphene. *Sci. Adv.* **2016**, *2* (4), e1501518–e1501518. https://doi.org/10.1126/sciadv.1501518.

(18) Yang, Y.; Brenner, K.; Murali, R. The Influence of Atmosphere on Electrical Transport in Graphene. *Carbon N. Y.* **2012**, *50* (5), 1727–1733. https://doi.org/10.1016/J.CARBON.2011.12.008.

(19) Chen, S.; Cai, W.; Chen, D.; Ren, Y.; Li, X.; Zhu, Y.; Kang, J.; Ruoff, R. S. Adsorption/Desorption and Electrically Controlled Flipping of Ammonia Molecules on Graphene. *New J. Phys.* **2010**, *12* (12), 125011. https://doi.org/10.1088/1367-2630/12/12/125011.

(20) Sato, Y.; Takai, K.; Enoki, T. Electrically Controlled Adsorption of Oxygen in Bilayer Graphene Devices. *Nano Lett.* **2011**, *11* (8), 3468–3475. https://doi.org/10.1021/nl202002p.

(21) Rumyantsev, S.; Liu, G.; Shur, M. S.; Potyrailo, R. A.; Balandin, A. A. Selective Gas Sensing with a Single Pristine Graphene Transistor. *Nano Lett.* **2012**, *12* (5), 2294–2298. https://doi.org/10.1021/nl3001293.

(22) Amin, K. R.; Bid, A. Effect of Ambient on the Resistance Fluctuations of Graphene. *Appl. Phys. Lett.* **2015**, *106* (18), 183105. https://doi.org/10.1063/1.4919793.

(23) Cao, G.; Liu, X.; Liu, W.; Li, Q.; Li, X.; Wang, X. Chemical Environment Dominated Fermi Level Pinning of a Graphene Gas Sensor. *Carbon N. Y.* **2017**, *124*, 57–63. https://doi.org/10.1016/J.CARBON.2017.08.026.

(24) Dan, Y.; Lu, Y.; Kybert, N. J.; Luo, Z.; Johnson, A. T. C. Intrinsic Response of Graphene Vapor Sensors. *Nano Lett.* **2009**, *9* (4), 1472–1475. https://doi.org/10.1021/nl8033637.

(25) Cadore, A. R.; Mania, E.; Alencar, A. B.; Rezende, N. P.; de Oliveira, S.; Watanabe, K.; Taniguchi, T.; Chacham, H.; Campos, L. C.; Lacerda, R. G. Enhancing the Response of NH3 Graphene-Sensors by Using Devices with Different Graphene-Substrate Distances. *Sensors Actuators B Chem.* **2018**, *266*, 438–446. https://doi.org/10.1016/j.snb.2018.03.164.

(26) Liu, Y.; Liu, H.; Chu, Y.; Cui, Y.; Hayasaka, T.; Dasaka, V.; Nguyen, L.; Lin, L. Defect-Induced Gas Adsorption on Graphene Transistors. *Adv. Mater. Interfaces* **2018**, *5* (9), 1701640. https://doi.org/10.1002/admi.201701640.

(27) Kumar, B.; Min, K.; Bashirzadeh, M.; Farimani, A. B.; Bae, M.-H.; Estrada, D.; Kim, Y. D.; Yasaei, P.; Park, Y. D.; Pop, E.; et al. The Role of External Defects in Chemical Sensing of Graphene Field-Effect Transistors. *Nano Lett.* **2013**, *13* (5), 1962–1968. https://doi.org/10.1021/nl304734g.

(28) Iwasaki, T.; Muruganathan, M.; Schmidt, M. E.; Mizuta, H. Partial Hydrogenation Induced Interaction in a Graphene–SiO_2 Interface: Irreversible Modulation of Device Characteristics. *Nanoscale* **2017**, *9* (4), 1662–1669. https://doi.org/10.1039/C6NR08117G.

(29) Kulothungan, J.; Muruganathan, M.; Mizuta, H. Modulation of Twisted Bilayer CVD Graphene Interlayer Resistivity by Order of Magnitude Based on In-Situ Annealing. *Carbon N. Y.* **2019**, *153*, 355–363. https://doi.org/10.1016/j.carbon.2019.07.036.

(30) Hwang, E. H.; Adam, S.; Das Sarma, S. Transport in Chemically Doped Graphene in the Presence of Adsorbed Molecules. *Phys. Rev. B* **2007**, *76* (19), 195421. https://doi.org/10.1103/PhysRevB.76.195421.

(31) Ramamoorthy, H.; Somphonsane, R.; Radice, J.; He, G.; Nathawat, J.; Kwan, C.-P.; Zhao, M.; Bird, J. P. Probing Charge Trapping and Joule Heating in Graphene Field-Effect Transistors by Transient Pulsing. *Semicond. Sci. Technol.* **2017**, *32* (8), 084005. https://doi.org/10.1088/1361-6641/aa7ba3.

(32) Lee, Y. G.; Kang, C. G.; Jung, U. J.; Kim, J. J.; Hwang, H. J.; Chung, H. J.; Seo, S.; Choi, R.; Lee, B. H. Fast Transient Charging at the Graphene/ SiO2 Interface Causing Hysteretic Device Characteristics. *Appl. Phys. Lett.* **2011**, *98* (18), 183508. https://doi.org/10.1063/1.3588033.

(33) Zhu, J.; Jhaveri, R.; Woo, J. C. S. The Effect of Traps on the Performance of Graphene

Field-Effect Transistors. *Appl. Phys. Lett.* **2010**, *96* (19), 193503. https://doi.org/10.1063/1.3428785.

(34) QuantumATK Atomic-Scale Modeling for Semiconductor & Materials https://www.synopsys.com/silicon/quantumatk.html (accessed Nov 11, 2019).

(35) Grimme, S.; Antony, J.; Ehrlich, S.; Krieg, H. A Consistent and Accurate Ab Initio Parametrization of Density Functional Dispersion Correction (DFT-D) for the 94 Elements H-Pu. *J. Chem. Phys.* **2010**, *132* (15). https://doi.org/10.1063/1.3382344.

(36) Hammer, B.; Hansen, L. B.; Nørskov, J. K. Improved Adsorption Energetics within Density-Functional Theory Using Revised Perdew-Burke-Ernzerhof Functionals. *Phys. Rev. B - Condens. Matter Mater. Phys.* **1999**, *59* (11), 7413–7421. https://doi.org/10.1103/PhysRevB.59.7413.

Chapter 5

Charge Neutrality Point Disparity for Molecular Identification: Proof-of-Concept

In chapter 2, the prospect for molecular identification based on the electrically tunable charge-transfer of graphene-gas molecule van der Waals (vdW) complexes was introduced. To this end, it was demonstrated in Chapter 4 that adsorbed gases on graphene possess a vdW bonding memory which is crucial for achieving charge-transfer based molecular identification as it ensures that the electrically tunable charge-transfer can be experimentally measured after turning off the V_t.

Consequently, in this chapter, a charge-transfer based molecular identification technique, 'Charge Neutrality Point Disparity' (CNPD) method for the empirical characterization of adsorbed molecules on graphene is demonstrated.

5.1. CNPD Method: Experimental Procedure

After the steps described in chapter 3 for measurements in dry air and atmospheric air, a specified tuning voltage was applied for a specific time after which the transfer characteristic was measured. Then a tuning voltage of opposite polarity (but equal magnitude) was applied for the same time, and the transfer characteristic measured again. This was repeated several times while keeping the order of tuning voltage application the same and the time lag between successive transfer characteristics and tuning voltage experiments to the barest minimum (< 10 seconds). For all CNPD results presented in this work, $-V_t$ was always applied before $+V_t$ and the gate voltage was always swept from -40 V to + 40 V during transfer characteristics measurement. The difference in the CNP positions between successive measurements was calculated. This value,

hereafter referred to as the CNPD value was found to be distinct for different gas environments and alike for ambience of similar composition. Results in this chapter are for both the a-CF-GFET and pristine graphene. When results for pristine graphene are presented, this will be clearly stated, hence except otherwise stated the presented results will be for a-CF-GFET.

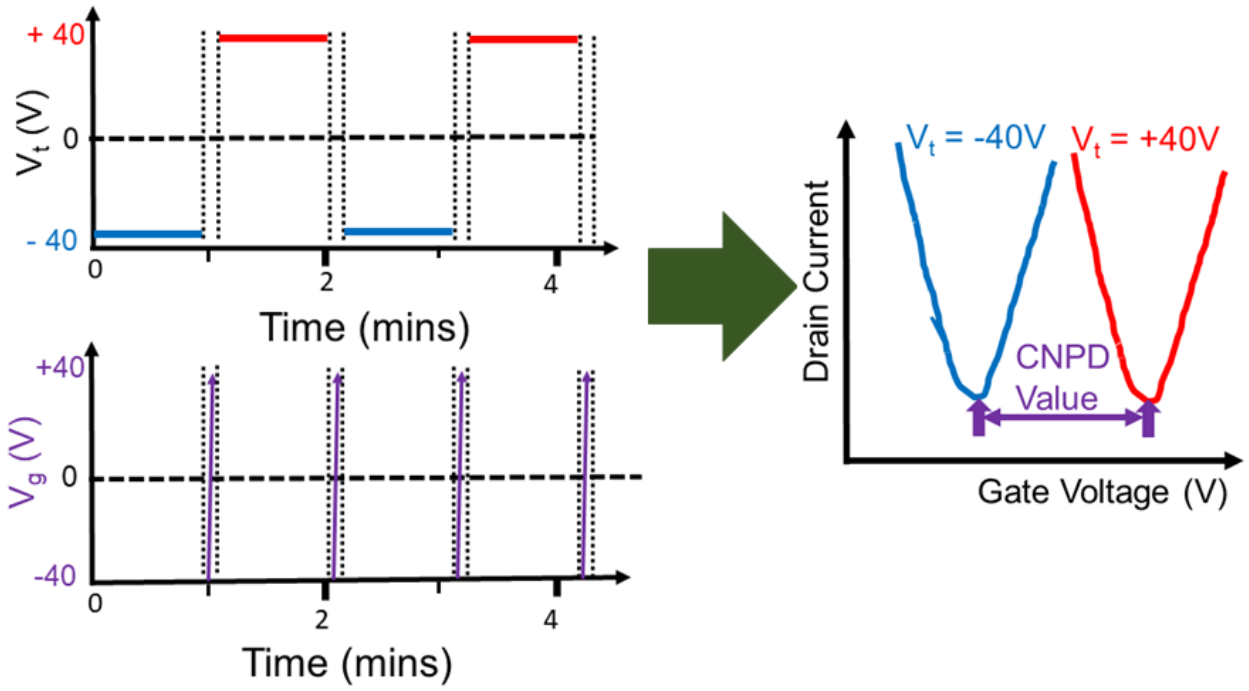

Figure 5.1: Experimental schematic for the CNPD method (left) and definition of the CNPD value for consecutive -V_t and +V_t transfer characteristics measurements (right).

The CNP was obtained by fitting the measured source-drain resistance (R_{tot}) of the device to the model:[1]

$$R_{tot} = R_c + R_{channel} = R_c + \frac{N_{sq}}{n_{tot} e \mu} \quad (5.1)$$

where R_c is the contact resistance, $R_{channel}$ = device channel resistance, N_{sq} denotes the number of squares of the gated area (L/W), e is the electronic charge and μ is the mobility. n_{tot} =

$\sqrt{n_o^2 + n[V_{TG}^*]^2}$ where n_o is the intrinsic carrier concentration of graphene at the charge neutrality point and $n[V_{TG}^*]$ is the gate-induced carrier concentration away from the charge neutrality point i.e. $V_{TG}^* = V_{TG} - V_{TG,Dirac}$. V_{TG}^* is related to the quantum capacitance, gate capacitance (C_{ox}) and V_{TG} thus:

$$V_{TG} - V_{TG,Dirac} = \frac{en}{C_{ox}} + \frac{\hbar v_F \sqrt{\pi n}}{e} \quad (5.1)$$

where $\hbar$ = reduced planck constant, v_F = Fermi velocity, and n carrier concentration.

The charge neutrality point is the gate voltage with the maximum resistance in the modeled data. A sample of the model fit to the raw data is shown in Figure 5.2 below.

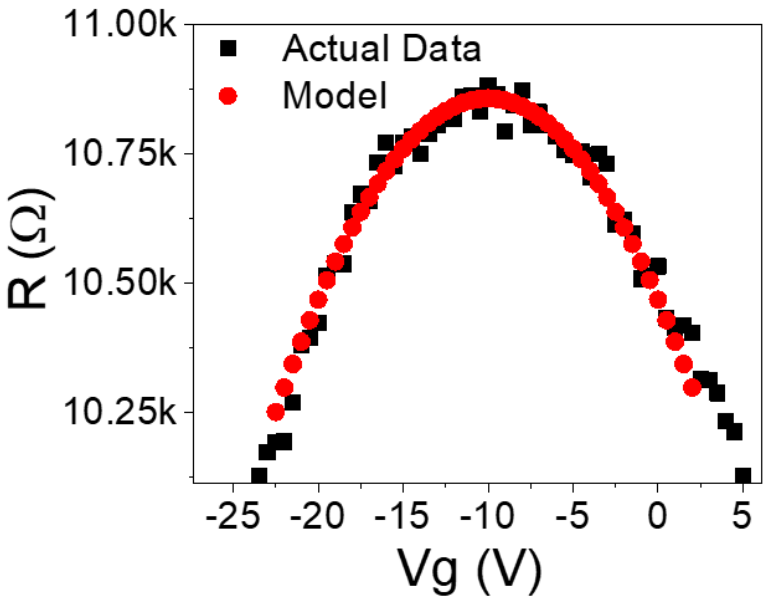

Figure 5.2: Model fitting to the experimental data. The model fitting was performed using 50 data points around the CNP. The total transfer characteristics had 161 data points.

5.2. Dependence of CNPD Values on Applied Electric Field

First, the dependence of the CNPD value on the applied tuning voltage (Figure 5.3a) was investigated by exposing a single 200 nm x 200 nm device to 200 ppb ammonia in dry air at room temperature and tuning voltages of $\mp 20\ V$, $\mp 30\ V$, $\mp 40\ V$ separately.

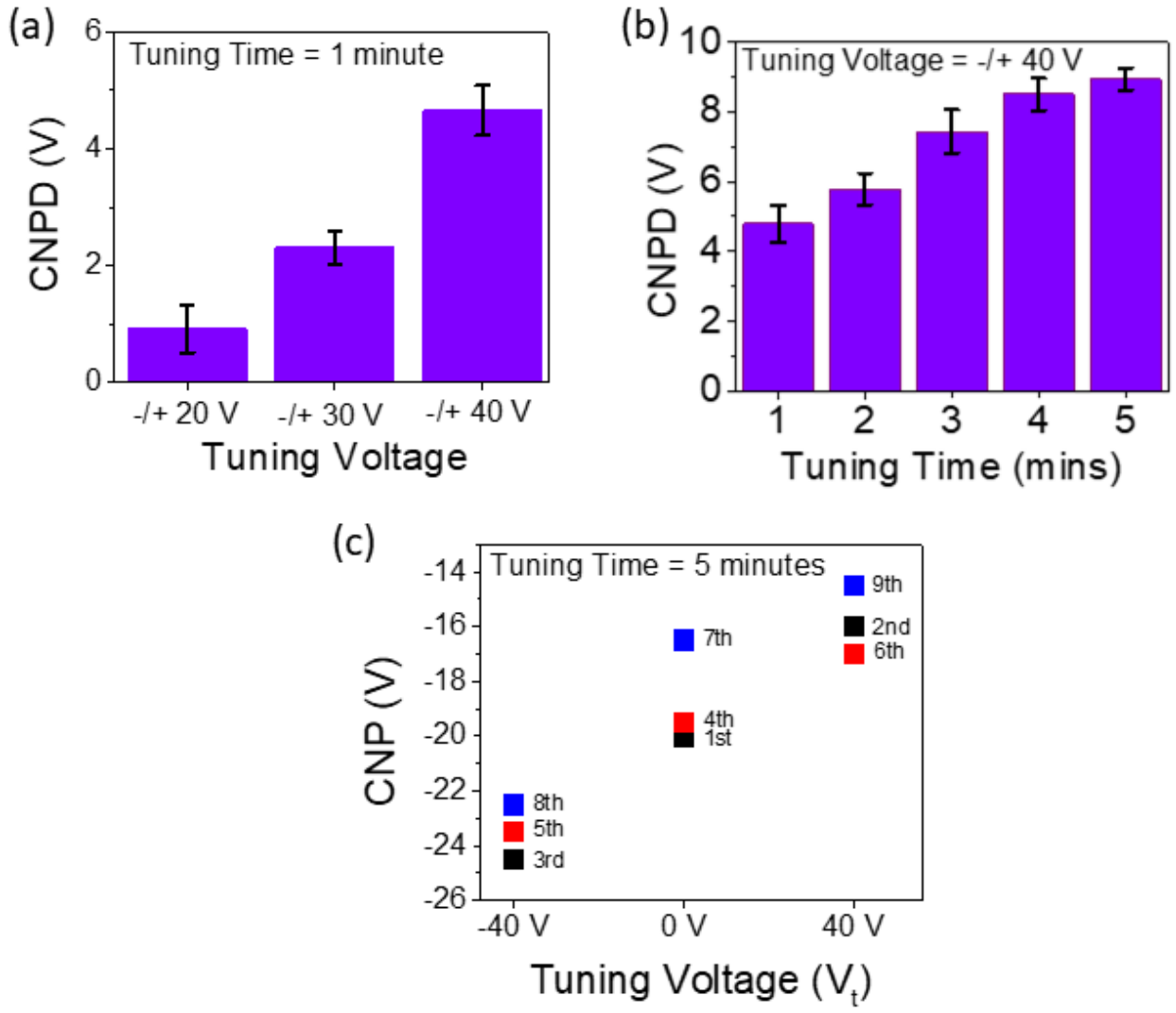

Figure 5.3: CNPD tuning voltage dependence and reversibility. (a) Dependence of the CNPD value on the tuning time. Error bars represent the standard deviation in the data set. (b) Dependence of the CNPD value on the applied tuning voltage. (c) Reversibility of the V_t-induced van der Waals complexes with changing V_t (-40 V, 0 V, and +40

V) for 84 ppm ammonia in dry air, tuning time = 5 mins. Labels show the order of V_t application from 1st to 9th measurement with the respective applied V_t in the x-axis and the corresponding CNP position after V_t application in the y-axis.

The resulting CNPD value decreased with decreasing tuning voltage (Figure 5.3a). For 84 ppm ammonia in dry air at a V_t of $\mp 40\ V$(Figure 5.3b), the obtained CNPD values also decreased with tuning time confirming that the CNPD value is electric-field induced as less tuning voltage application implies a smaller difference between the $\mp V_t$ induced graphene-molecule vdW complex bonding states. Since the measured CNPD values depend on both the applied V_t and tuning time, the same tuning voltage ($\mp 40\ V$), tuning time (1 minute) were used for all comparative analysis in this work, except otherwise stated. It is important to note that the V_t induced states have a van der Waals bonding memory (as demonstrated in chapter 4), and so are not completely lost immediately after turning off the V_t,[2] however as shown in Figure 5.3c the electrically induced graphene-molecule van der Waals complex can also be switched between different V_t induced states in real-time. This is important as it enables the quick measurement of the V_t-induced vdW bonding characteristics in real-time.

5.3. CNPD Values in Various Gas Environments

To ascertain the applicability of the CNPD method for characterizing various environments, the CNPD value of a pristine CVD graphene device exposed to acetone/N_2 and ammonia/N_2 at ppb concentrations was measured (Figure 5.4a) showing two distinct mean CNPD value ranges of 2.86 – 3.27 V for acetone and 3.32 – 4.59 V, successfully differentiating both environments. The higher CNPD value for ammonia can be attributed to the larger polarity of ammonia facilitating more graphene-gas interaction.

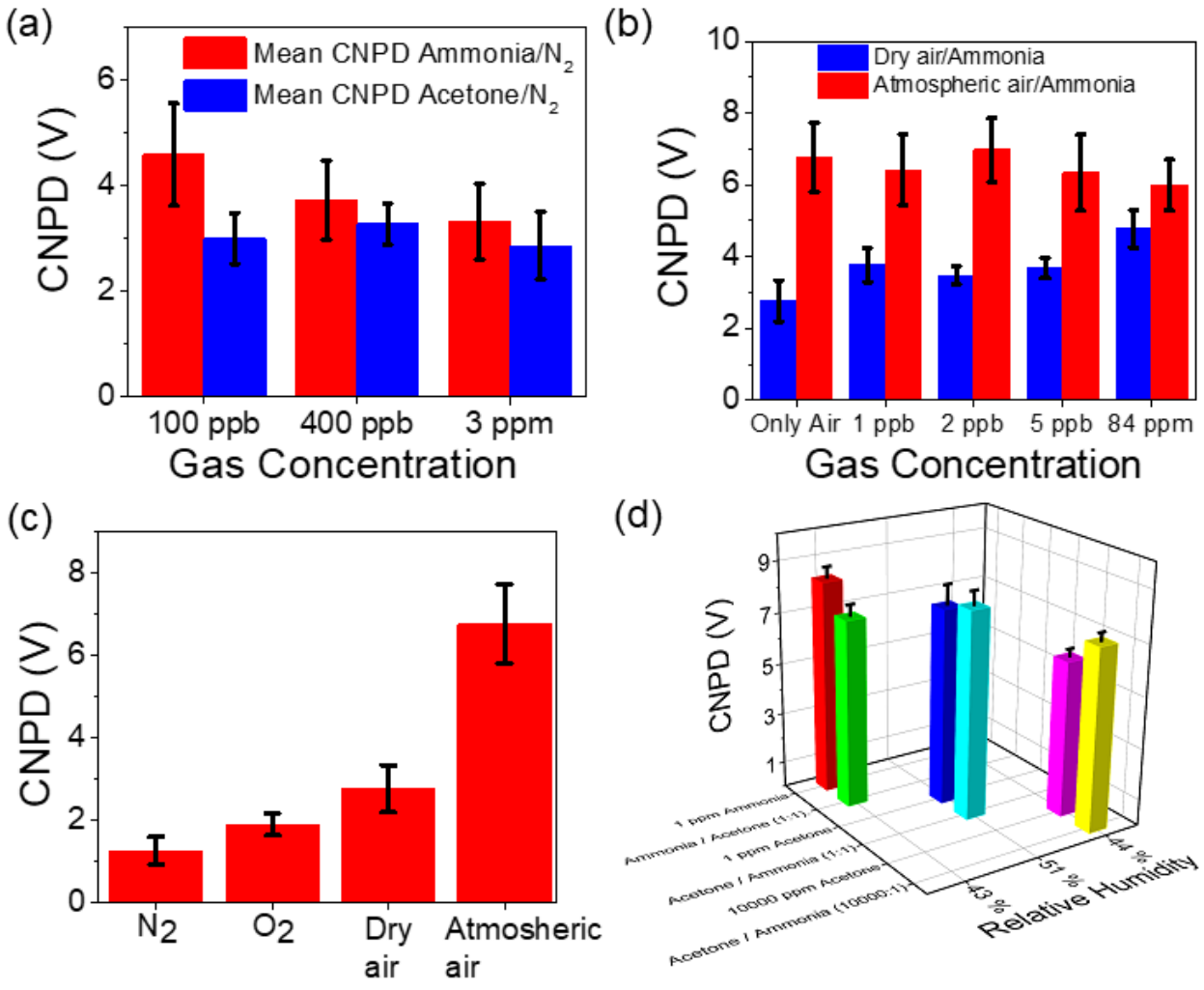

Figure 5.4: CNPD dependence on the gas environment. (a) Variation of CNPD value for ammonia and acetone using pristine graphene. (b) Variation of the CNPD value for ammonia in atmospheric/dry air using the a-CF-GFET device. (c) Dependence of the CNPD value of the a-CF-GFET device to various gas environments. (d) Variation of the CNPD value at 110°C for three separate experiments (i-iii below) for sequential addition of (i) 1 ppm NH_3 (red bar) and 1 ppm acetone to atmospheric air (green bar), (ii) 1 ppm acetone (blue bar) and 1 ppm NH_3 to atmospheric air (cyan bar) (iii) 10000 ppm acetone (violet bar) and 1 ppm NH_3 (yellow bar) to atmospheric air. Error bars represent the standard deviation in the data set.

The 200 x 200 nm a-CF-GFET sensor was also used to characterize 1 ppb, 2 ppb, 5 ppb, and 84 ppm of ammonia in atmospheric and dry air (Figure 5.4b) showing a mean CNPD value range of 3.47 – 4.79 V in dry air which increased to 6.00 – 6.97 V in atmospheric air. The

specificity of the CNPD values to various gas environments makes it a useful index in improving the performance of machine learning algorithms in e-nose single graphene sensors as gas specific signals hugely improve the accuracy of the machine learning models while reducing the number of dimensions needed for model training.[3]

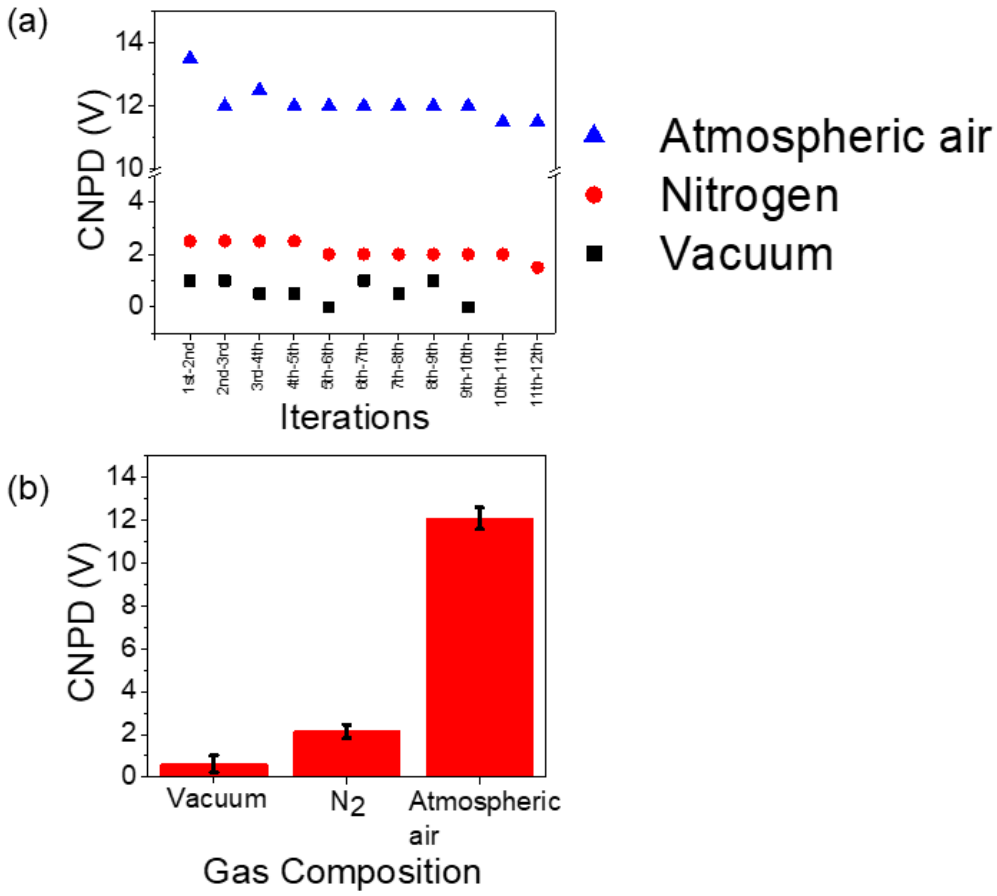

Figure 5.5: CNPD of the a-CF-GFET device in vacuum, nitrogen, and air. (a) Individual CNPD values for the different iterations. (b) Mean CNPD from (a). The error bar represents the standard deviation in the data set.

The CNPD value gradually increased with the polarity of the environment on exposure to various typical gas sensing environments: nitrogen, oxygen, dry air, and atmospheric air, (Figure 5.4c) with smaller CNPD values for relatively inert environments (nitrogen, oxygen, dry air) and larger CNPD for atmospheric air.

The higher CNPD in more oxidizing environments (Figures 5.4 b,c) can be attributed to the fact that the CNPD is charge-transfer based and so will be more sensitive to gas adsorption in more polar environments. The CNPD value response to periodic changes in atmospheric air at 110 ^{o}C to mixtures of air/ammonia/acetone is shown in Figure 5.4d. Before the CNPD measurement, the gas was exposed to UV light for 1 minute to improve the acetone response.[4] The CNPD increased with the introduction of ammonia and decreased with acetone which agrees with the generally higher CNPD values obtained for the pristine graphene-ammonia complex compared to the pristine graphene-acetone complex (Figures 5.4a,b). Besides the gas molecules introduced into the chamber, adsorbed molecules on graphene from the device fabrication steps as well as the activated carbon on the graphene channel have a small contribution to the CNPD (as shown in Figures 5.5 a,b) where a residual CNPD was observed in vacuum for a 300 nm x 1 µm device measured at 110 ^{o}C (tuning time = 2 minutes, $V_t = (\mp 40\ V)$.

5.4. Summary

Following the demonstration of the vdW bonding memory of graphene-molecule complexes in chapter 4,[2] the reversible switching between the $-V_t$ and $+V_t$ van der Waals bonding states in real-time is shown in this chapter. Consequently, a proof-of-concept (the CNPD method) for characterizing adsorbates on the graphene channel is demonstrated. The CNPD method which is based on the signature V_t induced charge-transfer of adsorbates on the graphene channel measures the difference in the CNP of the V_t-tuned graphene-molecule vdW complexes at opposite V_t polarities. The CNPD values are shown to be electrically tunable, increasing with the applied V_t and tuning time. The specificity of the CNPD value to individual gas environments makes it a good index for e-nose sensing using a single graphene sensor as signal specificity to adsorbate has been shown to improve the performance of machine learning e-nose algorithms.

References

(1) Hassanpour Amiri, M.; Heidler, J.; Müllen, K.; Asadi, K. Design Rules for Memories Based on Graphene Ferroelectric Field-Effect Transistors. *ACS Appl. Electron. Mater.* **2020**, *2* (1), 2–8. https://doi.org/10.1021/acsaelm.9b00532.

(2) Agbonlahor, O. G.; Muruganathan, M.; Imamura, T.; Mizuta, H. Adsorbed Molecules as Interchangeable Dopants and Scatterers with a Van Der Waals Bonding Memory in Graphene Sensors. *ACS Sensors* **2020**, *5* (7), 2003–2009. https://doi.org/10.1021/acssensors.0c00403.

(3) Hayasaka, T.; Lin, A.; Copa, V. C.; Lopez, L. P.; Loberternos, R. A.; Ballesteros, L. I. M.; Kubota, Y.; Liu, Y.; Salvador, A. A.; Lin, L. An Electronic Nose Using a Single Graphene FET and Machine Learning for Water, Methanol, and Ethanol. *Microsystems Nanoeng.* **2020**, *6* (1), 1–13. https://doi.org/10.1038/s41378-020-0161-3.

(4) Yang, C. M.; Chen, T. C.; Yang, Y. C.; Meyyappan, M.; Lai, C. S. Enhanced Acetone Sensing Properties of Monolayer Graphene at Room Temperature by Electrode Spacing Effect and UV Illumination. *Sensors Actuators, B Chem.* **2017**, *253*, 77–84. https://doi.org/10.1016/j.snb.2017.06.116.

Chapter 6

Conclusions and prospects

In this work, a facile and scalable technique for fabricating highly sensitive and selectivity activated carbon functionalized graphene-based ammonia gas sensors with room temperature sensitivity of 500 parts per trillion in atmospheric air and a response time of 3 seconds is demonstrated. (Chapter 3). The ammonia sensitivity and selectivity of the fabricated device makes it suitable for applications in clinical and environmental sensors. Additionally, it is shown that the electrically tunable charge-transfer of adsorbed gases on graphene exhibits a van der Waals bonding memory with carrier scattering dependent on the graphene-gas adsorption distance (Chapter 4). Finally, a proof-of-concept, CNPD method for characterizing various gas environments using both the pristine CVD graphene and activated carbon functionalized graphene is demonstrated (Chapter 5). In this chapter, the prospects for this work is discussed.

First, preliminary research results on the effect of temperature and pressure on the obtained CNPD transfer characteristics (Figures 6a-d) are presented.

6.1. Procedure for Temperature and Pressure Dependence of the CNPD Reversibility

First, the a-CF-CFET device was recovered and left at the desired measurement temperature. Next the transfer characteristics in vacuum was observed, and thereafter, the desired gas or air was introduced into the chamber and the transfer characteristics measured again. For measurements in atmospheric air, the pressure in the chamber was reduced to about 600 Torr, and the transfer characteristics measured (for gases in air, the desired concentration of gas was introduced into the

chamber now and the transfer characteristics measured again). Thereafter, (for all gas environments) the chamber was left for 5 minutes without any measurement, and the transfer characteristics measured after this 5 minutes wait. Next, the gases were exposed to UV light for 1 minute, and the transfer characteristics measured again. Then the CNPD measurement i.e. alternative $\mp V_t$ and transfer characteristics measurement was done as described in chapter 5.

6.2. CNPD Reversibility: Preliminary Results

As shown in Figures 6a-d, at high temperature (~110 ^oC) and atmospheric pressure, the -40 V and +40 V states of the graphene-molecule vdW complexes become easily reversible (Figure 6d) while at lower pressure the V_t-induced vdW complexes became less reversible (Figure 6a-c).

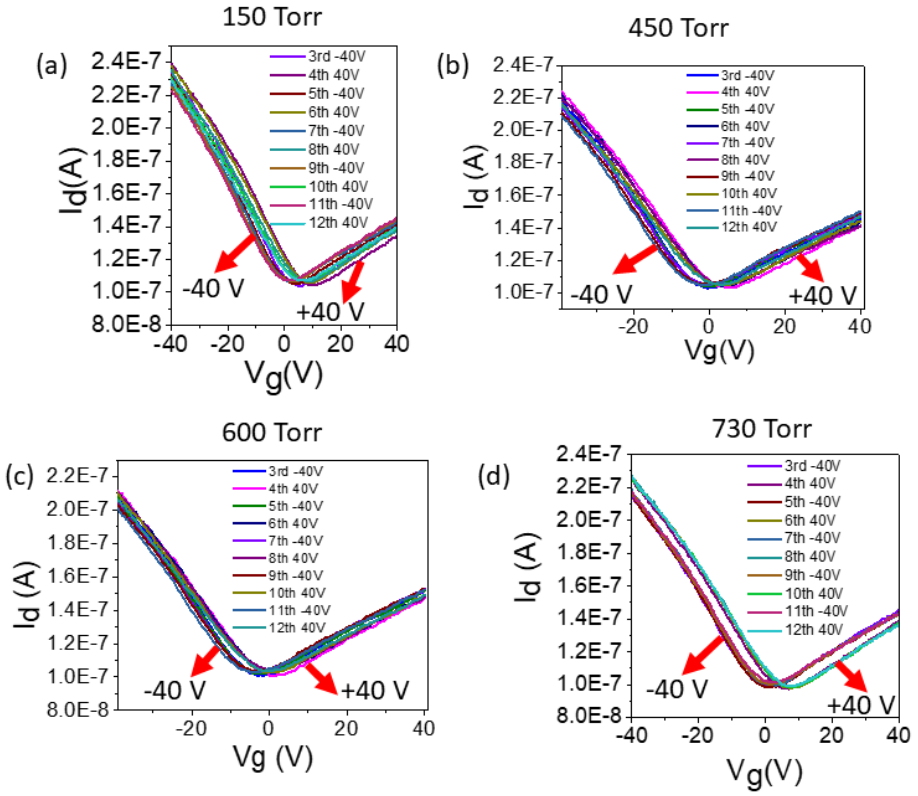

Figure 6.1: Pressure dependence of CNPD transfer characteristics in pure nitrogen. (a) 150 Torr (b) 450 Torr (c) 600 Torr (d) 730 Torr.

Furthermore, this temperature and pressure dependence of the CNPD reversibility was independent of the gas showing a similar trend in nitrogen (Figure 6.1), acetone/nitrogen (Figure 6.2), and atmospheric air (Figure 6.3a-c). As shown in Figure 6.3b, at room temperature and high pressure (730 Torr), this reversibility could not be achieved. Hence, for easy reversibility in the CNPD transfer characteristics, high temperature (110 ^{o}C) and pressure (730 Torr) are required. Additionally, the reversibility is affected by the presence or absence of a wait time of about 5 minutes (Figure 6.3a,c) in which the gases were left undisturbed in the chamber as described in the experimental section. Though the reasons for the above observations are not very clear, it may be attributed to the high kinetic energy of the gases at higher temperatures and pressures resulting in easy reversibility of the vdW bonding interaction upon V_t application. Additionally, at 110 ^{o}C degrees, the effect of p-doping due to adsorbed water is reduced resulting in less changes in the CNP and transfer characteristics of the device. Consequently, a quasi-equilibrium distribution of adsorbed gases on graphene is readily formed at high pressure and temperature. Further, investigation on the pressure and temperature dependence of the CNPD reversibility to clarify the molecular dynamic effects involved is needed. Additionally, the measured CNPD values could be fit into different isotherms to provide better insight on the pressure and temperature dependence of the CNPD.

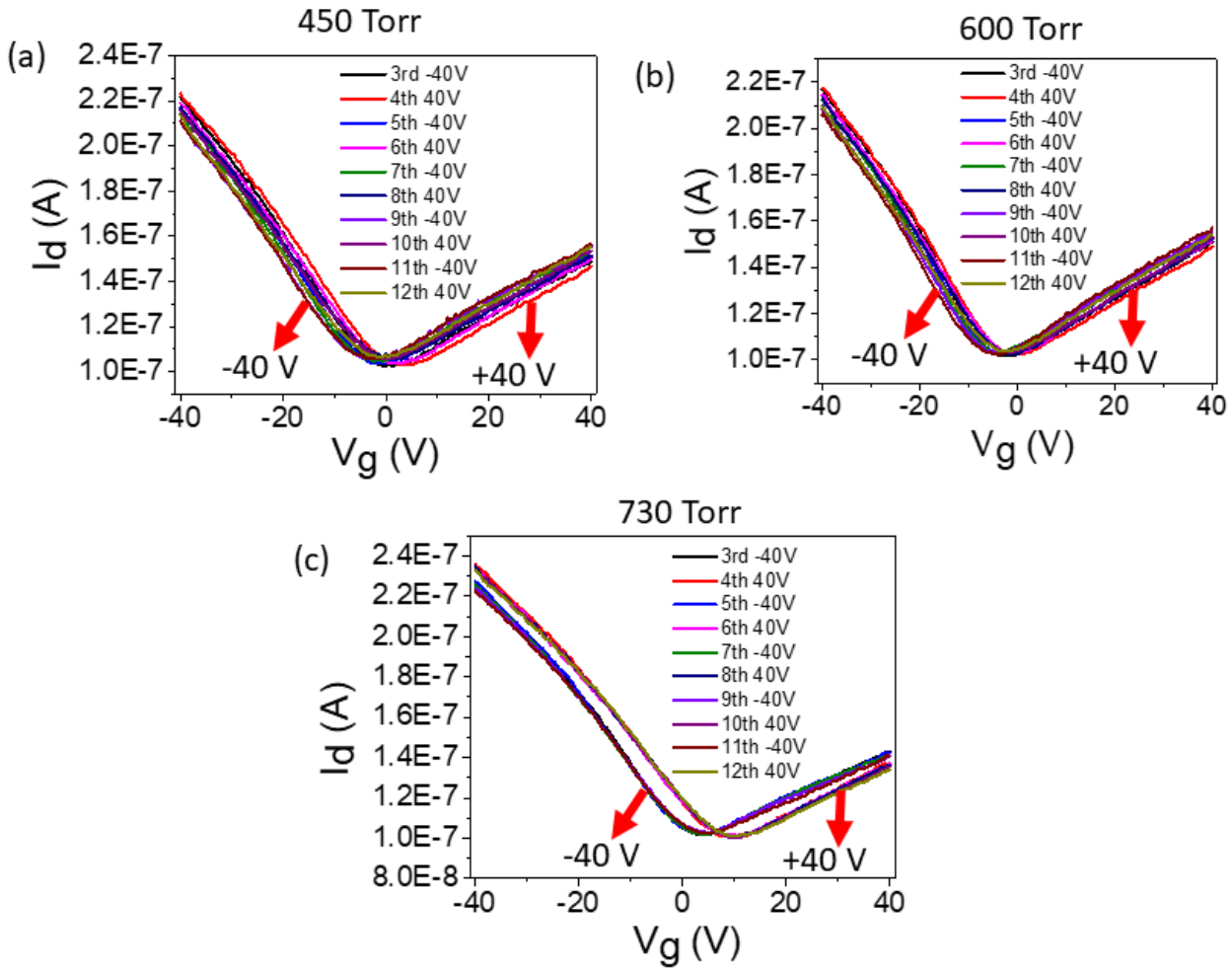

Figure 6.2: Pressure dependence of CNPD transfer characteristics at 110 ^{o}C for Acetone/N_2. (a) 450 Torr, (b) 600 Torr, (c) 730 Torr.

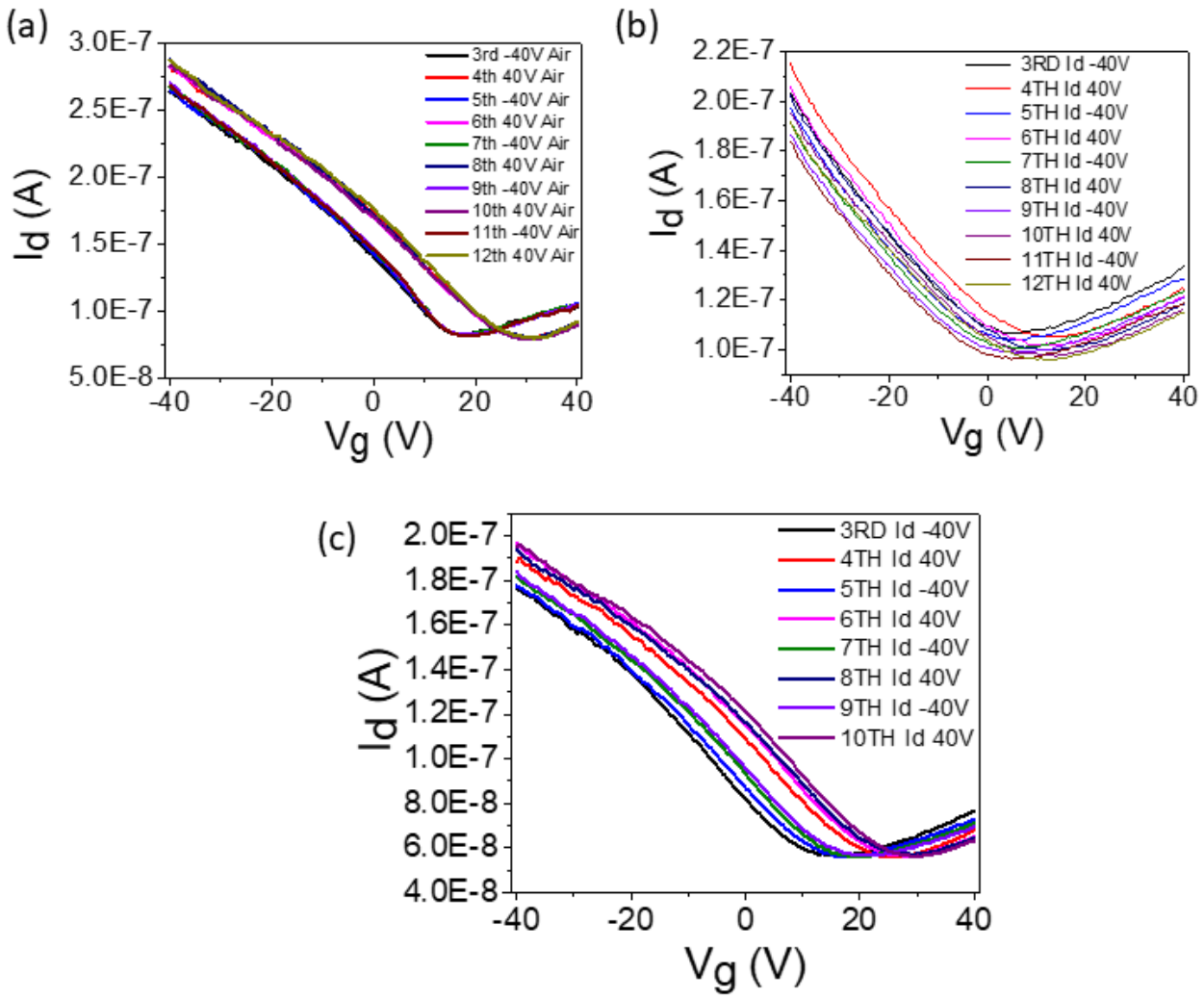

Figure 6.3: Pressure dependence of CNPD transfer characteristics for atmospheric air. (a) 110 ^{o}C with 5 minutes wait, (b) room temperature without 5 minutes wait (c) 110 ^{o}C without 5 minutes wait.

Furthermore, the effect of annealing temperature, device size, and annealing environment on the porosity distribution and gas selectivity should be studied to better understand the properties of the a-CF-GFET sensor. Finally, the application of the CNPD values in machine learning algorithms for the molecular identification of various gases is needed to ascertain the effectiveness of the gas-specific CNPD signature values for pattern recognition of adsorbed gases.

Publication List

1. Osazuwa G. Agbonlahor, Manoharan Muruganathan, Tomonori Imamura, and Hiroshi Mizuta. Adsorbed Molecules as Interchangeable Dopants and Scatterers with a Van der Waals Bonding Memory in Graphene Sensors. ACS Sensors 5, 2003–2009 (2020).
2. Takuya Iwasaki, Shu Nakamura, Osazuwa G. Agbonlahor, Manoharan Muruganathan, Masashi Akabori, Yoshifumi Morita, Satoshi Moriyama, Shinichi Ogawa, Yutaka Wakayama, Hiroshi Mizuta, Shu Nakaharai. Room-temperature negative magnetoresistance of helium-ion-irradiated defective graphene in the strong Anderson localization regime. *Carbon (Under Review).*
3. Osazuwa G. Agbonlahor, Manoharan Muruganathan, Sankar Ganesh Ramaraj, Zhongwang Wang, Ahmed M.M. Hammam, Afsal Kareekunnan, Hisashi Maki, Masashi Hattori, Kenichi Shimomai, and Hiroshi Mizuta. Room temperature atmospheric ppt-level gas sensing and molecular identification in nanopored activated-carbon functionalized graphene. *Nature Nanotechnology (Submitted).*

Patents

1. 'Sensor devices and their manufacturing method'. Manoharan Muruganathan, Gabriel Agbonlahor, Amit Banerjee, Hiroshi Mizuta, and 4 other co-inventors. Filing number: 2020-063788 (Filing Date: 31 March 2020)
2. 'Sensor devices, their manufacturing method and gas identification method'
   Manoharan Muruganathan, Gabriel Agbonlahor, Amit Banerjee, Hiroshi Mizuta, and 4 other co-inventors. Filing number: 2020-063789 (Filing Date: 31 March 2020)

3. 'Gas identification method and gas identification system' Manoharan Muruganathan, Gabriel Agbonlahor, and four co-inventors Filing number: 2019-157961 (Filing Date: 30 August 2019)

International Conferences

1. **Adsorption Distance Effects on Gas Adsorption Induced Scattering in Graphene Gas Sensors**. Osazuwa Gabriel Agbonlahor, Manoharan Muruganathan, Tomonori Imamura, Hisashi Maki, Masashi Hattori, Hiroshi Mizuta 2020 International Conference on Solid State Devices and Materials (SSDM2020), 27-30 Sept 2020, Toyama, Japan (Online)

2. **Observation of charge carrier localization-induced negative magnetoresistance at room temperature in helium-ion-irradiated defective graphene.** Takuya Iwasaki, Shu Nakamura, Osazuwa Gabriel Agbonlahor, Manoharan Muruganathan, Masashi Akabori, Yoshifumi Morita, Satoshi Moriyama, Shinichi Ogawa, Yutaka Wakayama, Hiroshi Mizuta, Shu Nakaharai 2020 International Conference on Solid State Devices and Materials (SSDM2020), 27-30 Sept 2020, Toyama, Japan (Online)

3. **Observation of charge carrier localization-induced negative magnetoresistance at room temperature in helium-ion-irradiated defective graphene.** Takuya Iwasaki, Shu Nakamura, Osazuwa Gabriel Agbonlahor, Manoharan Muruganathan, Masashi Akabori, Yoshifumi Morita, Satoshi Moriyama, Shinichi Ogawa, Yutaka Wakayama, Hiroshi Mizuta, Shu Nakaharai

2020 International Conference on Solid State Devices and Materials (SSDM2020), 27-30 Sept 2020, Toyama, Japan (Online)

4. **Graphene NEMS technology for advanced sensing and phonon engineering** H. Mizuta, S. Nakano, Y. Furukawa, H. Miyashita, G. Agbonlahor, M. Haque, S. Ogawa, Y. Morita, J. Kulothungan, A. Hammam, S Ramaraj, A. Banerjee, F. Liu, M. Schmidt and M. Muruganathan. 5th Malaysia-Japan Nanotechnology Conference, Japan, 8-9 March, 2020

5. **Graphene Nano-Electro-Mechanical (NEM) Devices and Extension to Sensor Applications (Invited Talk).** H. Mizuta, G. Agbonlahor, H. Miyashita, K. Taketomi, J. Lee, N. Huynh and M. Muruganathan. The Semiconductor Process Integration 11 Symposium in 236th ECS Meeting, Atlanta, 13-17 October, 2019

6. **Downscaled graphene devices for extreme sensing, sub-thermal switching and heat phonon engineering (Invited Talk).** H. Mizuta, M. Haque, S. Kubo, G. Agbonlahor, H. Miyashita, K. Taketomi, J. Kulothungan, S. Ogawa and M. Muruganathan. The 4th Malaysia-Japan Joint Symposium on Nanoelectronics 2019, Kuala Lumpur, 4-5 March, 2019

7. **Graphene nano-electro-mechanical (NEM) device technology for extreme sensing, sub-thermal switching and heat phonon engineering (Invited Talk).** H. Mizuta, ME Schmidt, M. Haque, S. Kubo, G. Agbonlahor, H. Miyashita, J. Kulothungan, S. Ogawa and M. Muruganathan. 3rd International Conference on Emerging Advanced Nanomaterials (ICEAN 2018), Newcastle, Australia, 30 Oct.-2 Nov., 2018

8. **Graphene NEMS technology for extreme sensing and nano thermal engineering (Plenary Speech).** H. Mizuta, ME Schmidt, M. Haque, S. Kubo, G. Agbonlahor, H. Miyashita, J. Kulothungan, S. Ogawa and M. Muruganathan. 19th EuroSciCon Conference on Nanotechnology & Smart Materials, Amsterdam, 4-6 October, 2018

Domestic Conferences

1. **Atmosphere-Specific Response in Graphene Field-Effect Transistors** Osazuwa Gabriel Agbonlahor, Manoharan Muruganathan, Hiroshi Mizuta 2020年3月12-15日、第67回応用物理学会春季学術講演会、上智大学　四谷キャンパス

2. **High sensitive detection of Acetone gas using Graphene nanoribbon sensor** R. Sankar Ganesh, Gabriel Agbonlahor, H. Maki, M. Manoharan, H. Mizuta 2020年3月12-15日、第67回応用物理学会春季学術講演会、上智大学　四谷キャンパス

3. **Detection of ammonia via charge transfer-induced shift of graphene charge neutrality point.** Osazuwa Gabriel Agbonlahor, Jothiramalingam Kulothungan, Manoharan Muruganathan , and Hiroshi Mizuta 第79回応用物理学会秋季学術講演, 2018年9月18日-21日、名古屋国際会議場

4. **Negative Magnetoresistance of Helium-ion-irradiated Graphene(presented in Japanese)**. T. Iwasaki, G. Agbonlahor, M. Muruganathan, M. Akabori, Y Morita, S. Moriyama, S. Ogawa, Y. Wakayama, H. Mizuta, S. Nakaharai 第79回応用物理学会秋季学術講演会, 2018年9月18日-21日、名古屋国際会議場

Acknowledgement

My utmost gratitude goes to Mizuta Sensei for accepting me into a Ph.D. program in his laboratory and his guidance throughout the program. I am also indebted to Manoharan Sensei, for his guidance, useful discussions, corrections, and very constructive criticisms. Many thanks to Dr. Wang Zhongwang for teaching me graphene fabrication in the cleanroom. I also have to thank Dr. Hammam for improving my understanding of device fabrication and helping with troubleshooting of various device fabrication problems. Mention must be made of Dr. Jothi and Schmidt for their useful discussions on device fabrication.

I am very grateful to Professor Yukiko Takamura for useful discussions and corrections of my PhD research documents. Special thanks to Professor Daniel Moraru for serving as the external reviewer for this dissertation, as well as Professor Akabori Masashi, Professor Tokumitsu Eisuke, and Professor Yuzuru Takamura who served as the internal reviewers. I highly appreciate the efforts of Professor Yuzuru Takamura and Dr. Dhirose towards the success of my minor research in Takamura Laboratory. I must appreciate Dr. Afsal, Dr. Chieu Liu, Professor Oshima, and Nobuaki Ito for their help with instrumentation and device characterization.

Special thanks to past and present members of Mizuta Laboratory for their useful discussions and friendly disposition. I am very grateful to Gunter Ellrott and Dr. Amit Banerjee for their very constructive criticisms, useful discussions, and help with measurement set-ups. Thanks to Kubo and Gunter Ellrott for improving my understanding of LabVIEW programming. I must also thank all the new friends I made in JAIST (too many to mention) who made my stay very enjoyable.

Finally, I must appreciate my friends and family back home in Nigeria, who though are not here with me, kept encouraging me throughout the Ph.D. program.

Yours Sincerely,

Osazuwa Gabriel Agbonlahor.